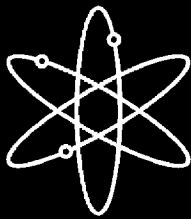




# Characterization of Radioactive Slags



**U.S. Nuclear Regulatory Commission  
Office of Nuclear Regulatory Research  
Washington, DC 20555-0001**



---

---

# Characterization of Radioactive Slags

---

---

Manuscript Completed: February 2004

Date Published: October 2004

Prepared by

L.A. Veblen<sup>1,2</sup>

D. Farthing<sup>2</sup>

E. O'Donnell<sup>1</sup>, J.D. Randall<sup>1</sup>

<sup>1</sup>Office of Nuclear Regulatory Research

U.S. Nuclear Regulatory Commission

Washington, DC 20555-0001

<sup>2</sup>Department of Earth and Planetary Sciences

Johns Hopkins University

Baltimore, MD 21218

**Division of Systems Analysis and Regulatory Effectiveness**

**Office of Nuclear Regulatory Research**

**U.S. Nuclear Regulatory Commission**

**Washington, DC 20555-0001**



## AVAILABILITY OF REFERENCE MATERIALS IN NRC PUBLICATIONS

### NRC Reference Material

As of November 1999, you may electronically access NUREG-series publications and other NRC records at NRC's Public Electronic Reading Room at <http://www.nrc.gov/reading-rm.html>.

Publicly released records include, to name a few, NUREG-series publications; *Federal Register* notices; applicant, licensee, and vendor documents and correspondence; NRC correspondence and internal memoranda; bulletins and information notices; inspection and investigative reports; licensee event reports; and Commission papers and their attachments.

NRC publications in the NUREG series, NRC regulations, and *Title 10, Energy*, in the Code of *Federal Regulations* may also be purchased from one of these two sources.

1. The Superintendent of Documents  
U.S. Government Printing Office  
Mail Stop SSOP  
Washington, DC 20402-0001  
Internet: [bookstore.gpo.gov](http://bookstore.gpo.gov)  
Telephone: 202-512-1800  
Fax: 202-512-2250
2. The National Technical Information Service  
Springfield, VA 22161-0002  
[www.ntis.gov](http://www.ntis.gov)  
1-800-553-6847 or, locally, 703-605-6000

A single copy of each NRC draft report for comment is available free, to the extent of supply, upon written request as follows:

Address: Office of the Chief Information Officer,  
Reproduction and Distribution  
Services Section  
U.S. Nuclear Regulatory Commission  
Washington, DC 20555-0001  
E-mail: [DISTRIBUTION@nrc.gov](mailto:DISTRIBUTION@nrc.gov)  
Facsimile: 301-415-2289

Some publications in the NUREG series that are posted at NRC's Web site address <http://www.nrc.gov/reading-rm/doc-collections/nuregs> are updated periodically and may differ from the last printed version. Although references to material found on a Web site bear the date the material was accessed, the material available on the date cited may subsequently be removed from the site.

### Non-NRC Reference Material

Documents available from public and special technical libraries include all open literature items, such as books, journal articles, and transactions, *Federal Register* notices, Federal and State legislation, and congressional reports. Such documents as theses, dissertations, foreign reports and translations, and non-NRC conference proceedings may be purchased from their sponsoring organization.

Copies of industry codes and standards used in a substantive manner in the NRC regulatory process are maintained at—

The NRC Technical Library  
Two White Flint North  
11545 Rockville Pike  
Rockville, MD 20852-2738

These standards are available in the library for reference use by the public. Codes and standards are usually copyrighted and may be purchased from the originating organization or, if they are American National Standards, from—

American National Standards Institute  
11 West 42<sup>nd</sup> Street  
New York, NY 10036-8002  
[www.ansi.org](http://www.ansi.org)  
212-642-4900

Legally binding regulatory requirements are stated only in laws; NRC regulations; licenses, including technical specifications; or orders, not in NUREG-series publications. The views expressed in contractor-prepared publications in this series are not necessarily those of the NRC.

The NUREG series comprises (1) technical and administrative reports and books prepared by the staff (NUREG-XXXX) or agency contractors (NUREG/CR-XXXX), (2) proceedings of conferences (NUREG/CP-XXXX), (3) reports resulting from international agreements (NUREG/IA-XXXX), (4) brochures (NUREG/BR-XXXX), and (5) compilations of legal decisions and orders of the Commission and Atomic and Safety Licensing Boards and of Directors' decisions under Section 2.206 of NRC's regulations (NUREG-0750).



## Abstract

Slag samples from three humid region sites located in the Eastern United States were studied in detail. Since this investigation is generic in nature, the precise locations of the sites are not identified and are referred to as Sites A, B, and C. Site A's slag was formed from a reprocessed Nb-Ta slag that was ground, leached and deposited in settling ponds which were allowed to evaporate. The resulting material was a "rock like," porous, altered material that resembled a sandstone. Site B was the most intensively studied site and it provided valuable information on the physical and chemical form of the original Nb and Ta slag, as well as the Sn slag that was used as the "ore" material. Site C's slag, although not studied in as much detail as the Site B slag, is physically similar to the Site B slag and both sites had (i) glassy slag and (ii) dense dark slags that ranged from fine grained to very coarsely crystalline. Detailed microanalytical data from Sites B and C provide information regarding the degradation of the radionuclide-bearing phases. Uranium and thorium are present in glass, perovskite, calzirtite, zirconolite, and pyrochlore. Cerium and thorium are present in hibonite. These phases are similar to phases in the proposed high-level radioactive waste form SYNROC. Numerous studies provide experimentally determined solubility and leach rates for these phases. These data provide insight into and bounding values for estimates of slag leach rates. Data reduction and a detailed petrological study provide the necessary information for guidance to the NRC's Office of Nuclear Material Safety and Safeguards for license termination at future decommissioning sites.



# Table of Contents

Abstract .....	iii
List of Figures .....	vii
List of Tables .....	ix
Executive Summary .....	x
Foreword .....	xi
<b>1.0 Introduction .....</b>	<b>1</b>
1.1 Background .....	1
1.2 Objective .....	1
1.3 Scope of the Research .....	1
1.4 Radioactive Source Term .....	2
1.5 Description of Site A .....	2
1.6 Description of Site B .....	2
1.7 Description of Site C .....	3
<b>2.0 Slag Characterization .....</b>	<b>7</b>
2.1 Introduction .....	7
2.2 Hand-size Sample Observation and Light Microscopy: Methods and Results .....	7
2.2.1 Site A .....	7
2.2.2 Site B .....	8
2.2.3 Site C: .....	9
2.3 Bulk Chemical Analyses of Slag - X-ray Fluorescence .....	9
2.3.1 Results of Bulk Chemical Analyses .....	9
2.4 Mineral Identification by X-Ray Diffraction: Methods and Results .....	10
2.4.1 Methods .....	10
2.4.2 X-Ray Diffraction of Site A Slag .....	10
2.4.3 X-Ray Diffraction of Site B Slag .....	10
2.4.4 X-Ray Diffraction of Site C Slag .....	10
2.5 Quantitative Analysis by Scanning Electron Microprobe and Electron Microprobe Analysis .....	10
2.5.1 Scanning Electron Microprobe and Electron Microprobe Analysis - Sample Selection and Preparation .....	10
2.5.2 Scanning Electron Microprobe and Electron Microprobe Analysis - Analytical Methods .....	11
2.5.3 Scanning Electron Microprobe and Electron Microprobe Analysis - Quantitative Analyses .....	11
2.5.3.1 Standards .....	11
2.5.3.2 Spectrometer Considerations .....	11
2.5.3.3 Quantitative Wavelength Dispersive Spectrometer (WDS) Analysis .....	11
2.5.4 Scanning Electron Microprobe and Electron Microprobe Analysis Results - Site A .....	11
2.5.5 Scanning Electron Microprobe and Electron Microprobe Analysis - Results Site B .....	12
2.5.6 Scanning Electron Microprobe and Electron Microprobe Analysis Results - Site C .....	12
2.6 Transmission Electron Microscopy .....	13
2.7 Surface Area Analyses: Methods and Results .....	13
2.8 Petrology of the Slags .....	13
<b>3.0 Slag Weathering .....</b>	<b>49</b>
3.1 Introduction .....	49
3.2 Estimating Radionuclide Release from Slags .....	49
3.2.1 Estimating Leach Rates as Mass Fluxes at the Slag Surface .....	49
3.2.2 Release to the Surrounding Fluid and Deposition onto the Slag Surface .....	50
3.2.3 Calculation of Bulk Leach Rates .....	51
3.2.4 Estimation of Mass Available for Transport .....	51
3.3 Naturally Weathered Samples .....	51
3.3.1 Natural Weathering Features at Site A .....	52
3.3.2 Natural Weathering Features at Site B .....	52
3.3.3 Natural Weathering Features at Site C .....	53
3.3.4 Estimation of Weathering Rate .....	54

3.3.5	Distinguishing Between Primary and Secondary Phases through the Use of Artificial Melts	54
3.4	Artificially Weathered (Leached) Samples	54
3.5	Archaeological Slags	55
3.5.1	Introduction	55
3.5.2	Dating of Archaeological Slags	55
3.5.3	Archaeological Slags Investigated	56
3.5.3.1	Tin Slag from England and Malaysia	56
3.5.3.2	Copper Slag from Cyprus	56
3.5.3.3	Lead and Silver Slag from the Czech Republic	56
3.6	Summary of Weathering Mechanisms of Slag	56
4.0	Conclusions and Recommendations	87
4.1	Site Specific Conclusions	87
4.1.1	Phases Present in Slag	87
4.1.1.1	Site A	87
4.1.1.2	Site B	87
4.1.1.3	Site C	87
4.1.2	Weathering in Slag	87
4.2	Generic Conclusions	88
4.3	Recommendations and Future Work	88
5.0	References	90
Appendix: Surface Mass-Transfer Coefficients		92
A.1	Fluid Flow Regimes	92
A.2	Idealizing Slag Shapes	92
A.3	Stagnant Fluid	92
A.4	Very Slow Flow	92
A.5	Laminar Flow	92
A.6	Turbulent Flow	92

## List of Figures

Figure 1-1.	Sampling buried slag at Site B. . . . .	4
Figure 1-2.	Site A samples. . . . .	4
Figure 1-3.	Hand sample of Site B slag. . . . .	5
Figure 1-4.	Hand sample of Site B slag. . . . .	5
Figure 1-5.	Top of slag pile at Site C. . . . .	6
Figure 1-6.	Close up of slag found at the ground surface at Site C. . . . .	6
Figure 2-1.	Photomicrographs of thin section of Site A slag sample A-2. . . . .	30
Figure 2-2.	Photomicrographs of thin section of Site A slag sample A-2. . . . .	31
Figure 2-3.	Photomicrographs of thin section from Site B slag sample B-8. . . . .	32
Figure 2-4.	Photomicrographs of thin section from Site B slag sample 96TC-19. . . . .	33
Figure 2-5.	Photomicrographs of thin section from Site B slag sample B-8 showing glass, gehlenite ( $\text{Ca}_2\text{Al}(\text{Al},\text{Si})\text{O}_7$ ), and perovskite ( $\text{CaTiO}_3$ ). . . . .	34
Figure 2-6.	Photomicrographs of thin section from Site B slag sample B-8 showing perovskite ( $\text{CaTiO}_3$ ) dendrites. . . . .	35
Figure 2-7.	Back scattered electron (BSE) image of a Sn slag (B-5.5) from Site B showing evidence of devitrification and alteration of glass. . . . .	36
Figure 2-8.	Back Scattered Electron (BSE) image of Site C slag sample C-1a. . . . .	37
Figure 2-9.	Photomicrographs of Site C slag sample C-S in plane polarized light and BSE. . . . .	38
Figure 2-10.	Ternary diagram of x-ray fluorescence data showing chemical composition for all of the slag collected. . . . .	39
Figure 2-11.	Compositional variation diagrams illustrating the variation of select elements when compared with $\text{TiO}_2$ . . . . .	40
Figure 2-12.	X-ray diffraction patterns of Site A slag. . . . .	41
Figure 2-13.	X-ray diffraction patterns of Site B slag. . . . .	42
Figure 2-14.	Back Scattered Electron (BSE) image and Energy Dispersive Spectra (EDS) patterns of Site A sample 96F-A-4. . . . .	43
Figure 2-15.	Back Scattered Electron (BSE) and x-ray map images of Site B slag sample B-5.5. . . . .	44
Figure 2-16.	Site B tin slag Sample B-8. . . . .	45
Figure 2-17.	Ion-milled Site B sample B-8. . . . .	46
Figure 2-18.	HRTEM image of Site B tin slag (sample B-8). . . . .	47
Figure 2-19.	Phase diagram of the $\text{ZrO}_2$ - zirconolite - $\text{TiO}_2$ + Ca Ti $\text{O}_3$ system (after Xu and Wang, 2000). . . . .	48
Figure 3-1.	Weathered Slags from Sites A and B. . . . .	59
Figure 3-2.	Photomicrographs of weathered slag under plane polarized light. . . . .	60
Figure 3-3.	SEM images showing weathering features in Site B sample B-5.5. . . . .	61
Figure 3-4.	TEM images of Site B tin slag B-8 showing weathering on a sub-microscopic scale. . . . .	62
Figure 3-5.	Back scattered electron (BSE) image of weathered Site B slag sample 96TC-19. . . . .	63
Figure 3-6.	Microprobe analyses of Site B sample 96TC-19 showing variation in rare earth elements (REE) as a function of proximity to distance from a fracture. . . . .	64
Figure 3-7.	Schematic diagram illustrating location of elemental variation measurements from Site B sample B-5.5 as a function of proximity to a weathered edge. . . . .	65
Figure 3-8.	Chemical changes associated with weathering. . . . .	66
Figure 3-9.	Compositional variation diagrams for Site B weathered glass. . . . .	68
Figure 3-10.	Electron microprobe analyses of Site B samples showing the elemental variation in calzirtite as a function of distance from a weathered edge. . . . .	70
Figure 3-11.	Photomicrograph of a weathered edge of a dense blocky slag (sample C-2a) from Site C. . . . .	71
Figure 3-12.	BSE image of remelted Site B slag. . . . .	72
Figure 3-13.	SEM secondary electron images of Site B Sn slag (B-5.5) showing surface of the slag leached by PNNL with deionized water. . . . .	73
Figure 3-14.	SEM secondary electron images of Site B Nb-Ta slag sample 96TC-19 after leaching by PNNL at pH 0.5 and pH 2. . . . .	74
Figure 3-15.	Elemental variation of glass in unleached and leached Site B sample 96TC-19. . . . .	75
Figure 3-16.	Elemental variation of hibonite in unleached and leached Site B sample 96TC-19. . . . .	76
Figure 3-17.	SEM secondary electron images of Site B slag sample 96TC-19 following leaching by PNNL at pH 2 and 4. . . . .	77
Figure 3-18.	SEM secondary electron images of Site B slag sample 96TC-19 after leaching by PNNL at pH 6, and 12. . . . .	78
Figure 3-19.	SEM secondary electron images of Site B Nb-Ta slag sample 96TC-19 contrasting a leached sample with an unleached one. . . . .	79
Figure 3-20.	BSE image of thorianite grains from Site A slag. . . . .	80
Figure 3-21.	Crift Farm tin slags, Cornwall, England. . . . .	81
Figure 3-22.	Pribram slag pile, Czech Republic. . . . .	81
Figure 3-23.	Photomicrographs of 1,000 year old Cyprus slag. . . . .	82

Figure 3-24. X-ray diffraction spectrum of Cu slag from Cyprus (using CuK $\alpha$ radiation). . . . .	83
Figure 3-25. BSE images of weathered edge of Site C sample C-1a. . . . .	84
Figure 3-26. Photomicrographs of Site C slag sample C-1a in plane polarized light. . . . .	85
Figure 3-27. Hypothetical plot of a slag's surface-concentration gradient. . . . .	86

## List of Tables

Table 2-1	Hand Specimen Description	15
Table 2-2	Measurements of Samples with Detectable Radioactivity	18
Table 2-3	Phases Present in Samples from Sites A, B, and C	19
Table 2-4	Chemical Composition of Major Elements in Slag Samples (weight %) as determined by XRF.	21
Table 2-5	Chemical Composition of Trace Elements in Slag Samples (ppm) as determined by XRF.	22
Table 2-6	List of minerals indicated by X-Ray Diffraction analysis of Site B Sample B-5.5a.	23
Table 2-7	Modal Abundance of Phases in Representative Site A Slag Sample as determined by Electron Microprobe Analysis (EMPA).	24
Table 2-8	Average Chemical Composition (weight %) of Most Common Phases Site A Samples as Determined by Electron Microprobe Analysis (EMPA).	25
Table 2-9	Modal Abundance of Phases in Representative Samples from Sites B and C Slag as determined by Electron Microprobe Analysis (EMPA).	26
Table 2-10	Average Chemical Composition (weight %) of Most Common Phases Site B Samples as Determined by Electron Microprobe Analysis.	27
Table 2-11	Average Chemical Composition (weight %) of Most Common Phases Site C Samples as Determined by Electron Microprobe Analysis.	28
Table 2-12	Weight Percent of Major Phases in Slag Samples and their Uranium, Thorium and REE (rare earth elements) abundance.	29
Table 3-1	Table for Estimating Leach Rate at Site B Based on Mineral Abundance in the Slag Samples.	58
Table 3-2	Archaeological Slags investigated in this study.	58

## Executive Summary

The US Nuclear Regulatory Commission (NRC) issues licenses to possess nuclear material for various purposes, one of which is the extraction of non-radioactive metals from ores that contain radioactive elements such as uranium and thorium. Some of the materials licensees are no longer extracting metal from radioactive ore and have asked the NRC to terminate their licenses. To terminate the licenses the NRC has to consider whether the slags left behind from the extraction processes have sufficiently low levels of radiation, or if the radioactive material is sequestered sufficiently to meet its license termination requirements.

The authors of this report used a suite of microanalytical tools at the Johns Hopkins University's Department of Earth and Planetary Sciences to characterize the radioactive slags, physically and chemically, so that realistic determinations of uranium and thorium leach rates from the slags can be made. Typically, leach rates are determined experimentally on either crushed or intact materials, using standardized tests such as ANSI/ANS 16.1, EPA 1311, or EPA 1312 leach tests. It has been reported<sup>1</sup> that experimentally determined leach rates range over four orders of magnitude. An objective of the study described herein was to reduce some of the uncertainty inherent in experimentally determined leach rates by providing the necessary detailed physical and chemical characterization of the slags to determine "realistic" leach rates. Information provided by this study will enable NRC decision makers and their licensees to calculate either a uranium and thorium solubility release model or a multi-phase leach rate model, and to compare estimated releases with those determined "in-situ" from quantitative electron microprobe analysis.

Three humid region sites located in the Eastern United States were studied in detail. Since this investigation is generic in nature, the precise locations of the sites are not identified and are referred to as Sites A, B, and C. Site A's slag was formed from a reprocessed Nb-Ta slag that was ground, leached and deposited in settling ponds which were allowed to evaporate. The resulting material was a "rock like," porous, altered material that resembled a sandstone. Site B was the most intensively studied site and it provided valuable information on the physical and chemical form of the original Nb and Ta slag, as well as the Sn slag that was used as the "ore" material. Site C's slag, although not studied in as much detail as the Site B slag, is physically similar to the Site B slag and both sites had (i) glassy slag and (ii) dense dark slags that ranged from fine grained to very coarsely crystalline. Detailed microanalytical data from Sites B and C provide information regarding the degradation of the radionuclide-bearing phases. Uranium and thorium are present in glass, perovskite, calzirtite, zirconolite, and pyrochlore. Cerium and thorium are present in hibonite. These phases are similar to phases in the proposed high-level radioactive waste form SYNROC. Numerous studies provide experimentally determined solubility and leach rates for these phases. These data provide insight into and bounding values for estimates of slag leach rates. Data reduction and a detailed petrological study provide the necessary information for guidance to the NRC's Office of Nuclear Material Safety and Safeguards for license termination at future decommissioning sites.

The quantification (by electron microprobe analysis) of uranium and thorium depletion or enrichment in the weathered surface of the slags provides estimates of short-term leach rates. A study of archaeological slags was undertaken to quantify the weathering of slag over the 1000-year period of interest to decision makers. Information from the short-term leach rates and estimated "in-situ" leach rates from the archaeological slags at various times provides a measure of how the leach rates change as a function of time. The leach-rate histories can also be used in decommissioning performance assessment computer programs codes such as RESRAD.

The authors investigated weathering (dissolution and alteration) mechanisms by measuring the elemental variation in naturally weathered decommissioning and archaeological slags and determined that the slags weather incongruently, i.e. certain phases dissolve preferentially. It was found that weathering occurs along grain boundaries and within particular grains and provides more penetrating access for fluids to the interior of the slags. It is possible that over time the slags will degrade chemically, while remaining semi-intact physically, similar to a saprolite. The authors' data suggest that the thorium, and perhaps uranium, will remain in the resistant (refractory) phases. Future decommissioning studies could collect x-ray fluorescence chemical data from the slag and compare it to data from this study. If the new data fall within the range plotted for Sites B and C, then it could be assumed that the new slag would have similar weathering properties and leach rates to the Site B and C slags. This would eliminate the need for more detailed characterization.

---

<sup>1</sup>Pickett, et al., 1998, Letter report: "Evaluation of Leach Tests for Estimating Release from Slag Sites subject to Decommissioning - Final Report."

## Foreword

The US Nuclear Regulatory Commission (NRC) issues licenses to possess nuclear material for various purposes, one of which is the extraction of non-radioactive metals from ores that contain radioactive elements, predominantly uranium and thorium. The leftover material from the extraction process (slag) is enriched in radioactive elements because of the extraction of the non-radioactive elements. Once licensees are no longer extracting metal from radioactive ore, they will seek to terminate their licenses. If the slags are not removed, the radioactive material in them may contaminate groundwater and surface water and may provide a health hazard. Before terminating a license, the NRC will consider whether any slags left behind from the extraction processes have sufficiently low levels of radiation, and if the radioactive material is sequestered sufficiently to meet NRC license termination requirements. Staff from the NRC's Office of Nuclear Regulatory Research conducted the research described in this report to provide technical support for these decisions.

Uranium and thorium are not uniformly distributed within the slags, but are present in various mineral phases. A suite of tools was used in this research project to characterize the radioactive slags, physically and chemically, so that realistic determinations of uranium and thorium leach and surface-deposition rates from the slags can be made. Typically, leach rates are determined experimentally on either crushed or intact materials, using standardized tests. An objective of the study described herein was to reduce some of the uncertainty inherent in experimentally determined leach rates, by providing detailed physical and chemical characterization of the slags to determine more "realistic" leach rates. This study provides methods for obtaining characterization data needed to determine whether any slags remaining at a site will meet license-termination criteria.

This report summarizes the results of research to characterize the crystalline and non-crystalline phases in slag samples from several NRC-regulated sites that are being decommissioned and contain isotopes of uranium or thorium. The slag was collected from three humid region sites in the Eastern United States. The purpose of this study was to identify the uranium- and thorium-bearing phases within the slags, and to evaluate the long-term stability of those phases. The results of this investigation give insights into the basic weathering mechanisms affecting the slag and the possible fate of the uranium and thorium radioisotopes.



Farouk Eltawila, Director  
Division of Systems Analysis and Regulatory Effectiveness  
Office of Nuclear Regulatory Research



## 1.0 Introduction

### 1.1 Background

The US Nuclear Regulatory Commission (NRC) issues licences to possess nuclear material for various purposes, one of which is the extraction of non-radioactive metals from ores that contain radioactive elements such as uranium and thorium. Some of these firms are no longer extracting metal from radioactive ore and have asked the NRC to terminate their licenses. NUREG-1444 (Fauver et al. 1993 and 1995) identifies as many as 17 sites containing radioactive slags.

The uranium and thorium in the slags described in this report were by-products of smelting operations that extracted niobium, tantalum, and tin. Various waste products were disposed on the sites, and in some cases moved off site. Solid and liquid waste were present at some of the sites. Liquid waste included waste water and liquids associated with leaching processes. Solid wastes included slags, both in their original form and also in leached, crushed and settled forms. Three sites were investigated in detail by the authors and are referred to in this report as Sites A, B, and C.

Because Sites A, B, and C, are in populated areas, and their slags tend to contain higher levels of radioactivity than the surrounding soil, it is important to determine the potential for release of radioactivity from the sites. To make such determinations, one must consider the weathering and leaching properties of the slags. These properties determine the rates at which elements may be released to the environment. The weathering properties of a slag depend on its physical, chemical, and mineralogical composition. These factors, in conjunction with local climatic conditions, control the rate at which uranium, and thorium are released from the slag.

The NRC assessment of a licensee's application to decommission a site and subsequent termination of the applicant's license relies on performance calculations that require consideration of the rates of leaching of uranium and thorium from slags containing them. Site characterization reports submitted by licensees for Sites A, B, and C provided information on the radiological assessment of the slags and other waste materials at the sites. However, the site characterization reports contain no information about the actual physical, chemical and mineralogic composition of the slags. These are the properties which will determine how easily the slags might leach into the environment.

### 1.2 Objective

The purpose of this study is to identify the phases within slags that contain uranium and/or thorium and to determine the long-term stability of those phases.

### 1.3 Scope of the Research

This is a report on the materials characterization of radioactive slags with emphasis on three of the sites identified in NUREG-1444. Preliminary analyses done at the Johns Hopkins University indicate that these slags are mixtures of glass and crystalline phases which are unusual in terrestrial rocks. This is due to the fact that the slags are the products from processing exotic ores and the reprocessing of Sn slags at extreme values of temperature and partial pressure of CO<sub>2</sub>. The slags are composed of minerals and glasses which resemble more closely lunar chondrites and meteorites than terrestrial basalts or Fe or Cu slags.

Determining the long-term performance of these unusual suites of minerals and glass is the focus of this report. To determine the long-term performance of the slags under weathering conditions typical of the sites, it is necessary to determine the crystalline and non-crystalline phases in the slags. This information can be linked with (a) results from laboratory leach tests based on ASTM standards, and (b) information from long-term weathering behavior of archaeological slags of similar chemical composition to understand fully the implications of weathering on the slag and its associated phases.

This research includes mineralogical and chemical data collected on samples from these sites. Much of the analytical work that characterized the crystalline and non-crystalline phases was done by L. Veblen (NRC/RES) and D. Farthing (Johns Hopkins University), at the Johns Hopkins University, Department of Earth and Planetary Sciences as a cooperative effort involving The NRC's Offices of Nuclear Regulatory Research (RES) and Nuclear Material Safety and Safeguards (NMSS), the Pacific Northwest National Laboratory (PNNL), and the NRC's Center for Nuclear Waste Regulatory Analyses (CNWRA).

A complete site characterization program for the three sites was beyond the scope of this project and the focus was on collecting material which exhibited radioactivity in the field. A scintillometer was used for this purpose. Determining the long-term performance of an entire slag pile is complicated by the slag's compositional heterogeneity. Slag piles are usually a mixture of soil, slag, and other waste. The slag pieces range in size from small cm-sized pieces to large cobbles 0.25 to 1.0 m in diameter. Based on sampling from this study, the larger pieces of slag were found to be the most radioactive materials on site. The slag at Site A was placed in mounds with minimal soil cover. Thus it lent itself to ready sampling. Sampling at Sites B and C was more difficult because of partial revegetation of the sites and because the slag was covered with approximately 0.3 to 1.0 m of soil and construction debris. At Site B it was necessary to dig a small pit to a depth of approximately 1.5m to collect slag samples (Figure 1-1).

Leaching studies of the slags were done by the CNWRA<sup>2</sup>. CNWRA analyzed slag leaching by comparing results from different standard leach tests [ANSI/ANS 16.1, 1986, EPA Method 1311 (TCLP), 1995, and EPA Method 1312 (SPLP), 1995]. The CNWRA results show that the tests rank in the following descending order of chemical aggressiveness: TCLP > SPLP > ANSI/ANS. It should be noted that the leach rates of uranium and thorium vary by four orders of magnitude among the three tests for the same slag.

Felmy et al. (2003), at PNNL performed leaching and solubility studies on the same slag samples as the CNWRA. The PNNL slags were leached in solutions with pH values ranging from 0.5 to 12 which provided important insights on the weathering of some of the slag samples.

To determine the long-term performance of the slags, archaeological slags, similar to the decommissioning slags, were collected from Cornwall, England, the Czech Republic, and Cyprus (see Section 3.4, "Archaeological Slags"). Information about how these older slags have weathered will aid in assessing the stability of the radioactive slags. Analytical work on the archaeological slags was done by Dori Farthing as a doctoral dissertation at Johns Hopkins University (Farthing, 2002).

#### 1.4 Radioactive Source Term

Given that there are limited records on materials and slag composition at these sites, it is difficult to determine the source term. To quantify the radionuclide source term it is necessary to gather information regarding (1) the type and amount of ore (source material), flux and any additional materials used during the smelting, and (2) the smelting process used at a site. From this information a general characterization of the slag can be estimated. It is beyond the scope of this project to examine in detail the materials used or their amounts. In Sections 1.5, 1.6, and 1.7 which follow we shall address in general terms the materials on site and the smelting processes used at the three SDMP sites.

With regard to a source term, Sites A, B, and C processed niobium and tantalum, but each used a different process for the beneficiation and extraction from the primary ores and/or tin slags. Accessory phases rich in uranium, thorium, and rare earth elements (REE), are part of the original ore, and are concentrated in the slag which was generated by the smelting process. These elements are incompatible with the metallic portion of the smelt and are residual products that are concentrated in slag.

#### 1.5 Description of Site A

---

<sup>2</sup> Pickett, et al., 1998, Letter report: "Evaluation of Leach Tests for Estimating Release from Slag Sites Subject to Decommissioning - Final Report".

Site A is no longer producing Nb-Ta slags and subsequent to our sampling of the site in 1997 the slag was transferred to a licensed radioactive waste disposal site.

Site A produced ferro-columbium concentrate with ore from the Araxa mine in Brazil between 1963 and 1969. The process was an exothermic or aluminothermic reaction in which Fe-Nb ore was crushed and combined with Al powder, FeSi, and Fe<sub>2</sub>O<sub>3</sub>. The mixture was ignited to produce a Fe-Nb tap slag and Fe silicate waste slag.

The tap slag, which contained most of the Fe and Nb, was separated from the silicate slag by crushing. The silicate slag was then ball-milled, and water floatation was used to separate any remaining Fe and Nb from the slag. The waste slurry was sent to settling/evaporation ponds, and the leachate was recycled to the floatation slurry. Most of the Th remained in the waste slag and ended up in the settling/evaporation ponds, where the solid material settled and was lithified through natural cementation processes as the settling ponds evaporated. The resulting slag resembles a cross-bedded sandstone. A reddish-brown weathered surface was observed on samples which had been exposed to the atmosphere and this is found in the sample illustrated in Figure 1-2. Figure 1-3 is a photograph of this slag showing the features that one commonly associates with sedimentary rocks.

Prior to the removal of the radioactive material from Site A, the radioactive material was mounded into piles approximately 5 - 8m (15 - 25 ft) high. The piles, located at the sites of the settling/evaporation ponds, were covered by grasses, wild flowers, and a 20 cm soil veneer. The piles contained the sandstone-like waste material and "failed taps" or batches of melt that failed to produce the dense metallic Fe-Nb layer, but instead formed a "lava-like" mass in which the Fe-Nb was distributed throughout the mass. The plant would have about one failed smelt during each year.

#### 1.6 Description of Site B

Site B is located within 100m of a river. A slag pile lies to the west of a decommissioned fabrication warehouse, several hundred yards from residential buildings. The slag pile forms a steep slope and the pile is covered with some soil, trash, and numerous plants and trees. The size of the slag blocks is 0.3 to 1.0 m in diameter. Hand specimens of slag collected from the pit shown in Figure 1-1 are illustrated in Figures 1-3 and 1-4. One sample exhibits a glassy texture and it probably represents the outer surface of a cooling block. The other is fine grained and probably represents the center of a cooling block.

NRC staff made three site visits to Site B to collect samples. The first visit of staff from RES and Johns Hopkins University (JHU) was in September 1996. The second was in November, 1996, with staff from PNNL, RES, and JHU. The third was in October,

1997, with NRC staff from RES and NMSS and the CNWRA.

During the first visit, it was noted that the site was covered with tall grass, weeds, wild sunflowers, young sycamore trees (~5 years old), older (~20 years old) sycamore, oak and maple trees, bushes, and a wide range of debris: concrete slabs, asphalt, wood, paper, etc. Slag samples were collected from the surface of the pile, at the slope edge, and in the pit dug at the location of a licensee's borehole. The borehole was selected because in a 1996 site characterization report, this particular borehole was reported to have some of the most radioactive material at the site from a depth of 1.5 to 3.7 m. To collect some of this material, a 1.5 m hole was dug, during the 1996 site visit to sample buried, near surface material. In this hole, slag, soil, concrete, asphalt, brick and wood from the decommissioned floor of the foundry were found to a depth of approximately 1.2 to 1.5 m. The slag found at the site and in this hole varied in texture and in size, ranging from large blocks 0.5 m in diameter to sand-sized grains. The Site B slag will be described in greater detail along with the samples from Sites A and C in Section 2.2, "Hand Sample Observation and Light Microscopy: Methods and Results." The blocks varied from glassy to dense, dark gray to black blocks. The site's soil also varied in appearance and texture. Some soil appeared to be oxidized (reddish) while other parts of the soil remained very dark gray to almost black. Soil samples were collected and analyzed for chemical composition. The slag pile was not uniformly compacted, and many large voids exist between many adjacent blocks of slag.

During the second sampling visit in November 1996 additional samples were collected from a borehole and at the location of several of the licensee's other boreholes.

The third sampling visit to the Site B was made in October 1997. Subsequent to the November 1996 sampling visit, the top of the site was bulldozed and cleared of debris and vegetation. The same boreholes previously sampled were enlarged at this time. The first was excavated to a depth of 1.5 m (Figure 1-2), and second to depth of 0.6 to 0.9 m. At the depth of 0.6 to 0.9 m, the original B1 borehole was found. B1 is 18 m deep and no water was found in the borehole. Slag and soils were collected from both holes.

A discussion of the method for extracting Nb and Ta from tin slags by an exothermic fusion process can be found in Gustison and Cenerazzo (1971). This reference provided valuable information on the material that constituted the source term for the slag

pile. The conditions of the Source Materials License for Site B issued by the Atomic Energy Commission in the 1960s authorized the on-site possession of ore (i.e. Sn slag) not to exceed 2 weight % uranium and thorium. This is consistent with our bulk chemical analyses of the Site B samples by x-ray fluorescence in which the highest concentration of uranium was 1980 ppm (~0.2%) (see Table 2-7).

### 1.7 Description of Site C

Site C is located on a river at the edge of a town. The site was the location of a metallurgical processing plant for ferro-niobium and ferro-nickel alloys that operated in the 1960s. An aluminothermic melting process was used to extract Nb-Ta from niobium ores and nickel scrap that contained up to 1 wt% thorium. Natural and depleted uranium were some contaminants of the metal scrap. Process slag contained thorium, uranium, and Ra-226. Little information regarding the smelting process is available. It is assumed that the aluminothermic melting process is similar to that of Site A, which is well documented.

The slag is stored in four separate sections adjacent to a river. The slag is partially buried under approximately 0.5 m to 1 m of soil and construction debris (see Figure 1-5). The materials from Site C described in this report were collected by NMSS staff in 1997 and by RES staff in April 2001. The 1997 samples were sent to CNWRA, where they were divided and a portion of the samples was sent to the Johns Hopkins University for characterization of the phases. The CNWRA used their samples for leaching studies (Pickett et al., 1998). The Johns Hopkins portion of the samples will be described in further detail along with the samples from Sites A and B in Section 2.2, "Hand Sample Observation and Light Microscopy: Methods and Results."

Although much of Site C's slag was covered, several blocks of a dense dark gray slag similar in appearance to some of the Site B slag were found at the ground surface. The outer surfaces of the blocks are highly weathered and this can be seen in Figure 1-6.

A radiological characterization of the waste and slag storage area, done for the licensee by a contractor in 1998, indicates that, generally, the slag has a much higher level of radioactivity than the surrounding materials. The radioactivity of the slag ranged from 0.3 pCi/g to 6,779 pCi/g, while the radioactivity of the soil, water, and river sediment was on the order of 1-20 pCi/g. Samples collected by RES staff in April 2001 averaged about 1000 pCi/g.



Figure 1-1. Sites B and C were covered with approximately 0.3 to 1.0 m of soil and construction debris. At Site B a small pit was excavated on top of the site to collect slag samples. The large block being pointed to had a prominent brownish weathering rind visible on the right side of the block.



Figure 1-2. Site A samples. Note the sedimentary features of these samples. This material was produced by crushing, leaching, and deposition of the material in a settling pond. The dark layers are enriched in thorium. The outer 1.2 cm top surface of the slag is weathered to a red-brown phase (Ba oxyhydroxides). (Photograph courtesy of CNWRA).



Figure 1-3. Hand sample of Site B slag. This sample is dominated by glass and is apparently a cooling surface of the slag. (Photograph courtesy of CNWRA).



Figure 1-4. Hand sample of Site B slag. This sample is more crystalline than the one shown in Figure 1-3 indicating that it was from the interior of a melt block. (Photograph courtesy of CNWRA).



Figure 1-5. Top of slag pile at Site C . The slag is found below the cleared area and it is covered with approximately 0.5 m to 1 m (1.5 ft to 3 ft) of soil and construction debris.



Figure 1-6. Close up of slag found at the ground surface at Site C. The interior is medium gray in color. The outer rusty brown colored surface is indicative of the rapid weathering of these blocks when exposed to the atmosphere.

## 2.0 Slag Characterization

### 2.1 Introduction

Samples were analyzed by a number of methods to determine the bulk chemical composition and the phases present. No single method can be used to identify all the phases present and their elemental chemistry efficiently and definitively. For example, light microscopy can sometimes be used for identification of the larger crystalline and glassy phases. However, the Scanning Electron Microscope (SEM), Electron Microprobe Analyses (EMPA), and Transmission Electron Microscopy (TEM) are needed for identification of the phases present in minute amounts. X-ray fluorescence is useful for providing information on the bulk chemistry but it can not determine the chemistry of individual minute phases. Therefore, a combination of analytical techniques is necessary to identify the mineral and crystalline phases in the slag accurately.

Selected hand samples were observed under a binocular reflected light microscope to determine areas of interest for further investigation. Splits were made of the samples. One portion was used for light microscopy, SEM, EMPA, TEM. These methods provide information on the possible phases present and their chemistry. For these analyses, two petrographic thin-sections were made. One was a polished section which was used for light microscopy, SEM, and EMPA. The other thin-section was used for TEM and was made with Aremco Crystalbond 509 (a thermoplastic cement). The other portion of the samples was powdered for X-ray diffraction (XRD) and X-ray fluorescence (XRF) analyses. XRD provided information on possible crystalline phases present and XRF was used for bulk chemical analyses of the samples.

### 2.2 Hand-size Sample Observation and Light Microscopy: Methods and Results

The physical appearance of hand-sized slag specimens varied widely as shown in Table 2-1. The greatest difference was between Site A and the other two sites. As noted previously in Section 1.5, "Description of Site A," the Site A slag's residual waste, also commonly called "slag," was formed by lithification of a Th-bearing waste slurry originally deposited in settling ponds that were allowed to evaporate. As the ponds evaporated the waste slurry was lithified by natural cementation processes. Because of this mode of origin, Site A "slag" resembles a stratified sandstone in which angular to sub-rounded grains are cemented together to form a reddish brown to light tan porous, grain supported sandstone as illustrated in Figure 1-2. In contrast, the slags from Sites B and C more closely resemble materials that formed from a melt. The Site B and C slags ranged from glassy black, blue, or green blocks similar to obsidian to dense, dark gray to black finely crystalline phases, similar to basalt as shown in Figures 1-3 and 1-4. The slags at all three sites appear to weather rapidly when exposed to the

atmosphere and it is common to find light tan to reddish brown weathering rinds on those exposed as seen in Figure 1-6. The extent of the alteration will be discussed in Chapter 3, "Slag Weathering."

The first step in the hand specimen analysis was measurement of sample radioactivity to determine which samples merited closer investigation. This was done in the laboratory at Johns Hopkins University with a Biochron meter and a 2 inch pancake Geiger/Muller probe. Results of the measurements of samples with detectable radioactivity are shown in Table 2-2. The highest measured doses were about 4.0 to 5.0  $\mu\text{Sv}/\text{hour}$  (400 to 500  $\mu\text{rem}/\text{hour}$ ).

Petrographic thin sections were made of all the slag samples. Transmitted and reflected light was used to identify the glass and crystalline phases present and their modal abundance was calculated by using a JEOL Super Probe (EMPA). Silicates, silicate glass, oxides, and metallic phases are present in all the slags sampled, but to a differing degree depending on the process and position relative to the outer surface (cooling surface). A list of crystalline phases and their chemical formulae is provided in Table 2-3. More detailed descriptions of each site follow.

#### 2.2.1 Site A:

As noted above, the Site A slag differs in physical form from the slag found at Sites B and C. The Site A slag formed by cementation of crushed slag which was placed in settling ponds for extraction of metals through leaching. The ponds were subsequently drained and the resulting material which had solidified was dumped on site.

Common phases in the solidified material include quartz grains, hibonite, gehlenite, perovskite, glassy clasts, thorianite, and metallic phases (see Table 2-3 for the chemical formulas of the phases). These phases are found in stratified layers where the darker layers are more concentrated with metallic and oxide phases and thus contain higher concentrations of heavy elements (Figure 2-1). Gehlenite, glass clasts, quartz, hibonite, and other silicates are more common in the lighter bands. A 1.2-cm crust of red-brown material coats the surface of the slag blocks. Microprobe analyses indicate that the crust is enriched in Ba-oxyhydroxides which are believed to be a product of weathering.

The phases observed in the settled slags are similar to those observed in slags from Site B, namely, gehlenite, perovskite, clinopyroxene, and zirconolite. However, thorianite is more prevalent in Site A samples than in samples from the other sites. Site A shares some of the same phases as Site C and it has Ba aluminate, perovskite and zirconolite (Figure 2-2). The cement that holds the grains together in the Site A material is difficult to characterize because it is very fine-grained and heterogeneous. Microprobe analyses indicate that the cement contains Al, Ca, Ba, and some Cl.

The presence of large perovskite and thorianite grains at Site A indicates that the site's smelting operations used a different source material from that used at Site B. A likely source might be ore from Brazil that often contains significant amounts of thorite. It is also possible that the thorianite is a secondary mineral formed by the breakdown of pyrochlore during leaching. The presence of thorianite as a secondary phase may be a means of constraining the concentration of Th in the system, with thorianite as the solubility-controlling phase.

### 2.2.2 Site B:

As noted earlier, soil and construction debris was mixed in with slag blocks. The site's soil varied in appearance and texture. Differences in color probably reflect the degree of exposure to the atmosphere (oxidizing conditions). Soil color ranged from reddish to reddish brown (most oxidized) to dark gray to black. Slags at the site can be divided into three groups based on physical appearance and mineral composition will be described in the paragraphs that follow.

The petrographic microscope was used for examination of the rock fabric, weathering features, and for identification of the phases present. The dominant phases are gehlenite, glass, clinopyroxene, perovskite, and calzirtite. To determine which phases contained uranium and thorium, electron microprobe analysis (EMPA) was used, and this will be described in further detail in Section 2.5 "Quantitative Analysis by Scanning Electron Microprobe and Electron Microprobe Analysis. The uranium and thorium are found in glass, perovskite, calzirtite, and in thorianite and pyrochlore which were present in only a trace amount (0.1%).

Three different kinds of slag were collected from Site B: (1) glassy slag that is grayish-green, (2) dense, blocky, finely crystalline slag, and (3) loosely cemented, dark gray blocks of crushed slag material. The dense, blocky, finely crystalline slag was the most radioactive of the material found at Site B and is the only one to be described here. The dark, dense, crystalline slag is found as large angular blocks. These blocks might be fragmented remnants of a melt similar in size to the melts produced at Site A: approximately 2-3 m in diameter, and up to 0.5 m thick. The dense blocky slags may also have been "failed melts" in which the Nb-Ta did not coalesce and sink to the bottom of the melt. The blocky slags are similar in appearance to the Sn slags that were dumped at the site.

Within the dense, blocky slag, different textures are observed. Surfaces that cooled quickly are glassy or have very fine grained crystals present within the glass (Figure 1-3). The crystal grain size increases toward the interior of the slag due to the increased time to cool to subsolidus temperatures. Grain size affects the leach rate of the slag since grain boundaries provide pathways for access by water. The blocky Site B slag has a thin (<20 mm) alteration

rind.

Examination of the Site B samples under polarized light with a petrographic microscope showed the following: silicate glass (e.g. Figure 2-3), was found in many samples and the glass fills interstices between dendritic crystals of perovskite, zirconolite, rutile, and euhedral crystals (crystals with a well defined shape) of pyrochlore, gehlenite and clinopyroxene in Site B's dense, black, finely crystalline slag (samples B-5.5 and RSP5.5).

In Site B sample 96TC-19 (Figure 2-4), the glass fills the gaps between euhedral crystals of hibonite and pyrochlore. The silicate minerals appear as large, euhedral grains. Gehlenite, which is clear in plane polarized light and highly birefringent under crossed polars, engulfs small blue euhedral crystals of an unknown phase (possibly hibonite), zirconolite and perovskite dendrites (e.g. Figures 2-5 and 2-6). Gehlenite is also more abundant in the rapidly cooled exteriors of the slag. Gehlenite often surrounds small hibonite crystals, and glass. Hibonite (Figure 2-4), a rare terrestrial mineral, with composition of  $\text{CaAl}_{12}\text{O}_{19}$  is more abundant in the interior of the slag, where higher temperatures persisted for a longer period of time. Hibonite, a well-known phase in meteorites (e.g. Keil and Fuchs, 1971; Smith, 1979) is thought to be one of the first phases to crystallize from a solar nebula at the formation of a solar system. Hibonite comes in a variety of colors and has been used to indicate oxygen fugacity at the time of crystallization (Ihinger and Stolper, 1986). The hibonite in the Site B slag is blue indicating highly reducing conditions at the time of formation (oxygen fugacity  $\sim 10^{(10-12)}$  atm).

A monoclinic phase, which is pleochroic and ranges from light brown to green, appears to be an Al-, Ti-, and Zr-rich clinopyroxene (Figure 2-3), similar to fassaite ( $\text{Ca}_{1.10}\text{Mg}_{0.39}\text{Ti}_{0.48}\text{Al}_{0.13}(\text{Al}_{0.74}\text{Si}_{1.26})\text{O}_6$ ), a phase found in the Allende meteorite (Dowty and Clark, 1973). Wollastonite ( $\text{CaSiO}_3$ ) has also been identified in sample 96TC-19.

Perovskite, pyrochlore, Fe prills, and zirconolite were identified by reflected light microscopy. Perovskite ( $\text{CaTiO}_3$ ) forms large opaque rectilinear dendrites in transmitted light. Perovskite appears as blue dendrites with 4-fold symmetry in transmitted light (e.g. Figure 2-6). Pyrochlore, a Ca-Nb-Ta oxide, is found as small cubic crystals surrounding the Fe prills (metallic spherules). Zirconolite is observed as small (5  $\mu\text{m}$ ) star shaped dendrites that are light brown in transmitted light. Larger (10  $\mu\text{m}$ ) zirconolite dendrites are opaque, but highly reflective.

Secondary phases which have probably formed as the result of devitrification and/or weathering are present in the Site B slag. Anorthite feldspar ( $\text{CaAl}_2\text{Si}_2\text{O}_8$ ) is a common devitrification phase, as seen in Figure 2-7. In addition, fine grained, feathery crystalline phases are observed, but are too small (<5  $\mu\text{m}$ ) to identify positively with the light microscope. Fine-grained (<1  $\mu\text{m}$ ) cerium silicates are present as a devitrification or alteration product of the glass. Rutile needles

appear as a devitrification product as well.

### 2.2.3 Site C:

Site C slags are heterogeneous in appearance and in chemical composition. They fall into 3 distinct groups based on mineral assemblage and physical appearance. The uranium and thorium found at Site C are concentrated in glass, calzirtite, and perovskite.

#### (1) Glassy Slags

Slags in this group (e.g. sample C- 5) are highly vitreous and often vesicular. Although all of the Site C slags contain some glass, it is most prevalent in samples from this group. Common crystalline phases in this group include  $\text{SiO}_2$  (in the form of dendrites and large rounded patches), fayalite ( $\text{Fe}_2\text{SiO}_4$ ), and phases containing Si, Ca, Al, Fe, K, Mn and Mg. The  $\text{SiO}_2$  phases are likely to have crystallized originally as tridymite or cristobalite. Tridymite and cristobalite are high-temperature polymorphs of quartz. When the slag cooled, the tridymite or cristobalite was no longer stable and recrystallized as quartz which is the phase stable at low temperature. This transformation from a high temperature phase to a low temperature phase involves a volume decrease and the effects of this are seen by the prevalent cracks in the dendrites and the large  $\text{SiO}_2$  patches (Figure 2-8)

#### (2) Dense Blocky Slags

These slags are distinctly different from those in the first group since they are more dense and blocky, and also seem to have fewer vesicles. Slags in this category are physically similar to basalts and to the black, finely crystalline slag from Site B (e. g. samples RSP 5 and B-5.5). Hand sample (C-4) is dark reddish-brown in color. Minerals found in this group include hibonite, barium aluminate, periclase, monticellite, Cr spinel, perovskite, zirconolite, metallic iron prills, wollastonite, wustite and an alteration product, ardelite  $\text{Ca}_2(\text{SO}_4)_2(\text{HPO}_4) \cdot 4\text{H}_2\text{O}$  (Figure 2-9).

#### (3) Green-Blue Slags

Slag in this group (e.g. C--6) is distinctly greenish-blue in color and often has a 1 mm thick white crust around the outside of the sample. Freshly cut surfaces of this group's slag reveal a greenish-blue interior and small circular brassy looking metallic prills are often visible to the naked eye. Mineralogically, this group contains spinel, periclase, monticellite, forsterite, perovskite, zirconolite, a Ti-silicate, a Ni-oxide and metallic chromium

Although the samples from Site C are distinct from those studied from the Sites A and B, there are some mineralogical similarities. For example, slag in the first two groups both have large perovskite crystals (Figure 2-9) as does slag from Site C.

At this site, two dominant radioactive slag types were present. One is similar to Site A and B because it had high aluminum phases (e.g. Ba aluminate, hibonite, or Ca Al phases). In this slag both uranium and thorium are in perovskite, pyrochlore, and Ti oxides such as thorianite. The second Site C slag is rich in 2 spinels and olivine. The dominant uranium and thorium bearing phases are glass, calzirtite, and perovskite

### 2.3 Bulk Chemical Analyses of Slag - X-ray Fluorescence

Slags can be separated into types based upon their bulk chemical composition. This provides a predictive tool for regulators interested in determining leaching characteristics of a slag from a particular site, without necessarily going through an extended mineralogical characterization. In the Ternary Diagram based on chemical composition shown in Figure 2-10 the slags and site soil can be seen to fall into groups.

Bulk chemical analyses of the slags were obtained using X-ray fluorescence (XRF) spectroscopy. These analyses were done with a Philips PW2400 spectrometer at Franklin and Marshall College, Lancaster, Pennsylvania. The results of the bulk chemical analyses of the major elements from XRF are reported in Table 2-4 and trace elements are in Table 2-5. Major elements are recorded in weight percent oxide (wt%) and trace element concentrations in parts per million (ppm).

Difficulties arise when analyzing slag samples, because they are enriched in trace elements relative to the standards used for "normal" rock analyses. The relatively high concentrations of thorium and uranium in the samples result in line overlaps with other elements on the spectra (notably in electron shells  $\text{Zr}\alpha$ ,  $\text{Y}\alpha$ ,  $\text{Sr}\alpha$ ,  $\text{Nb}\alpha$ ,  $\text{Ba}\alpha$  etc.) which causes a problem in quantifying the other trace elements. Trace elements which are present but have serious line overlaps are represented by a question mark (?) in Table 2-5.

#### 2.3.1 Results of Bulk Chemical Analyses

The slags sampled from the three sites vary in chemical composition, but can be classified in terms of major element oxides  $\text{CaO}$ ,  $\text{FeO}_T$ ,  $\text{Al}_2\text{O}_3$ , and  $\text{SiO}_2$ . Figure 2-10 depicts the range of slag compositions within the  $(\text{CaO} + \text{Na}_2\text{O})$ ,  $(\text{TiO}_2 + \text{FeO}_T + \text{Al}_2\text{O}_3)$ ,  $\text{SiO}_2$  ternary system. The samples cluster in three areas: (1) soils which are high in  $\text{SiO}_2$ ; (2) reprocessed slag from Site A which is high in  $\text{FeO}_T$ ,  $\text{Al}_2\text{O}_3$ ; and (3) slags from Site B and Site C which have equal concentrations of  $\text{CaO}$ ,  $(\text{FeO}_T + \text{Al}_2\text{O}_3)$  and  $\text{SiO}_2$ . The slag from Site B can be further categorized into a Sn slag and a Nb/Ta slag that formed after the Sn slag was re-smelted.

It is also instructive to look at the compositional variation diagrams representing the slag's bulk chemical composition (Figure 2-11). These diagrams indicate that slags from Site B and C fall along a continuum of composition. Sn slag (the original feed

stock for the smelting operations) is found at Site B, thus contributing to the range of composition seen in the ternary diagram (Figure 2-10). The composition of slag from Site B plots within a tighter compositional range than Site C. This indicates that either the processing or the original stock material was more homogeneous than materials used at Site C, or that no original feed stock was disposed at these sites. It is clear from Figure 2-10 that slag from Site A was subject to different processing. Chemical composition plotted in a ternary diagram such as Figure 2-10 could be used for future slag analyses if the slags plot within a similar range to Site B's and Site C's slags.

## **2.4 Mineral Identification by X-Ray Diffraction: Methods and Results**

### **2.4.1 Methods**

Powder x-ray diffraction was used in conjunction with electron microprobe analyses to determine the identity of minerals within the slags. EMPA was also used to investigate the compositional variability of the slag phases. XRD analyses were done with a Philips diffractometer equipped with Materials Data, Inc., automation. Usually, a preliminary scan of a crushed sample was run from 5° to 60° or 70° 2θ at a step size of 0.05 degrees/step. A second, more detailed scan with smaller step sizes and longer counting times was then run. Phase identification was done by peak matching the collected data to known crystallographic data in the International Center for Diffraction Data (ICDD) database using the software program JADE (Materials Data, Inc.). Initially samples of the "whole-rock" slag were analyzed, however, the number of phases within the slag made it difficult to interpret the powder x-ray diffraction pattern of "whole rock" samples. (See Table 2-6 which shows the number of crystalline phases found in a single slag sample.) Analyses of slag separates were significantly easier to interpret. The separation was done by hand and by density differences of the individual phases. Some of the common crystalline phases found include gehlenite, hibonite, metal carbides, oxides of uranium and thorium, perovskite, and zirconolite.

### **2.4.2 X-Ray Diffraction of Site A Slag**

XRD spectra for Site A, Figure 2-12, samples indicate the presence of quartz, zirconolite, perovskite, metal carbides and oxides of uranium and thorium. Numerous additional phases are present but have not been verified. These spectra have not been background subtracted and the flatness of the spectra indicates the presence of little, if any glass in these particular samples.

### **2.4.3 X-Ray Diffraction of Site B Slag**

XRD scans of bulk slag samples from Site B are significantly simpler than those of Site A due to a smaller number of minerals present in the Site B slags. This can be seen in Figure 2-13 which shows

x-ray spectra for two Site B samples. The slag at the top at the top (96 TC-19) is thought to be waste product following Nb/Ta extraction from a Sn slag, and the slag at the bottom is thought to be Sn slag prior to Na/Ta extraction. In the former, hibonite appears to be the dominant phase and in the latter gehlenite appears to be the dominant phase. Spectra of Site B's group 1 slags (glassy slags) indicate the presence of quartz (SiO<sub>2</sub>) and a significant amorphous component (glass). Spectra of Site B's group 2 slags (dense blocky slags) indicate the presence of spinel, periclase, monticellite, and forsterite. SEM and EMPA (see below) indicate the presence of perovskite and zirconolite. However their concentration is low, thus, their peaks could not be positively identified by XRD. Spectra for slags from Site B's group 3 indicate the presence of spinel.

### **2.4.4 X-Ray Diffraction of Site C Slag**

As is the case with the slags from the other sites, there is a large number of phases present in the Site C slag. Mineral separates (either by hand picking specific grains or by density separation) were used to identify specific phases. XRD spectra of samples from Site C indicate the presence of gehlenite, zirconolite, rutile, calzirtite and pyrochlore.

## **2.5 Quantitative Analysis by Scanning Electron Microprobe and Electron Microprobe Analysis**

While light microscopy and XRD help identify the major phases within a slag, they cannot determine the chemical composition of the various phases, and therefore it is difficult to identify which phases contribute most to the radioactivity. The importance of linking the radioactivity to the phase is illustrated by the autoradiograph shown in Figure 3.1 in "Evaluation of Leach Tests for Estimating Release from Slag Sites Subject to Decommissioning Final Report" (Pickett et al., 1998.) The autoradiograph shows uranium and thorium disseminated throughout the slag. However Pickett et al., 1998, note that grain size limits the effectiveness of autoradiography on a micron scale. This was confirmed by our microprobe analyses which show that U and Th are found in specific phases rather than being uniformly disseminated throughout the slag. It should be noted that these phases will weather at different rates, and therefore the release of U and Th will vary over time.

### **2.5.1 Scanning Electron Microprobe and Electron Microprobe Analysis - Sample Selection and Preparation**

Following examination with the petrographic microscope, samples were selected for further study with the Electron Microprobe, based on their mineralogy, chemical composition, and possible radioactivity.

Slag samples were prepared in several ways. For observation of surface topography, samples were mounted on brass or carbon platforms using carbon paint. For slab samples, hand samples were cut and polished with diamond and alumina polishing

compounds to a mirror finish. Slabs were mounted in the electron microprobe using a universal holder. Grain mounts were made with embedded particles in 2.5 cm rings using Epotech 301 epoxy and were subsequently polished. Samples were also made into doubly-polished thin sections mounted with the heat-sensitive adhesive Crystalbond. All samples were coated with 50-100 Å of carbon in a carbon evaporator before their insertion into the electron microprobe.

## 2.5.2 Scanning Electron Microprobe and Electron Microprobe Analysis - Analytical Methods

Electron microprobe analyses were done with a JEOL 8600 Superprobe equipped with four wavelength-dispersive spectrometers (WDS) and a Tracor Northern TN-5500 energy dispersive spectrometer (EDS). The microprobe was operated at 25 keV with variable beam currents. Surface topography was investigated using secondary electron imaging (SEI). Backscattered electrons (BSE) were used for compositional imaging on polished thin sections or slabs.

X-ray maps were generated with both energy dispersive and wavelength dispersive spectrometers while rastering the beam over a stationary sample. Eight 128 x 128 pixel X-ray maps were collected simultaneously for different elements including Si, Ca, Ti, Zr, Ce, Ta, Th, and U. The beam was held at 30 nA and 25 keV with a dwell time of 2 seconds. Each set of maps took approximately 9 hours to collect.

## 2.5.3 Scanning Electron Microprobe and Electron Microprobe Analysis - Quantitative Analyses

### 2.5.3.1 Standards

Obtaining the proper standard for each element is of primary importance in the quantitative analysis of materials through the use of EMPA. As the bonding environment can affect the production of X-rays by the electron beam, standards must be chosen to have structures similar to that of the unknown material. Since the slag material contains many different types of materials (i.e., metal, oxides, silicates), a different standard for each material is recommended. However, this is not always possible. For the slag investigation, metal standards were used for all metal phases. Oxide and silicate phases were analyzed using oxide and silicate standards except for the rare-earth elements, which were standardized using rare-earth phosphates.

### 2.5.3.2 Spectrometer Considerations

Since many of the phases found in slags contain numerous elements in relatively high concentrations, overlap between X-ray peaks is a serious problem. Therefore, the peak used for quantification must be the most intense peak with the least interference from

any other possible element. In some cases, an overlap correction factor must be used when two elements cannot be completely separated. In addition, the position of background collection is very important for the detection of trace amounts of elements. The backgrounds chosen were determined to be free of interference with characteristic peaks for forty elements found in major to minor concentrations in the slag samples. This stringent requirement forced some background positions to be unusually far apart, so that linear background extrapolations are inappropriate. In these cases, a non-linear background correction factor was determined, based on the curvature of backgrounds in standards with similar mean atomic number.

### 2.5.3.3 Quantitative Wavelength Dispersive Spectrometer (WDS) Analysis

Quantitative wavelength dispersive spectrometer was used in conjunction with SEM and EDS to determine the chemical composition of the phases present in the slags. WDS analysis of slag materials were carried out using a 25 keV beam with 20 to 50 nA current and a beam diameter of 1µm. Peak and background counts were collected for 60 seconds for each element. Selected elements that were found in low concentration but were deemed important were analyzed repeatedly over the course of one analysis. Uranium and lead were analyzed with six 60 second replicates and thorium with five 60-second replicates. The total time for one analysis was 45 minutes. Data were reduced by the program CITZAF (Armstrong, 1989).

## 2.5.4 Scanning Electron Microprobe and Electron Microprobe Analysis Results - Site A

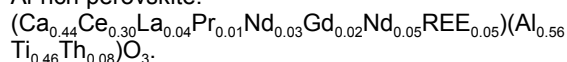
The major portion of the waste material at Site A site was a recycled slag. As described earlier, the original slag was crushed and leached, and allowed to settle in an evaporation pond. This material is now in the form of a sedimentary rock made up of angular clasts of glass, hibonite, Fe-bearing pyroxene (esseneite,  $\text{CaFe}^{+3}\text{AlSiO}_6$ ), perovskite, quartz ( $\text{SiO}_2$ ), thorianite ( $\text{ThO}_2$ ) and thorite ( $(\text{Th,U})\text{SiO}_4$ ). (Ideal chemical formulas of key phases are found in Table 2-3). It should be noted that uranite ( $\text{UO}_2$ ) forms a series with thorianite ( $\text{ThO}_2$ ).

The major Th-bearing phase is perovskite which has a general "idealized" formula of  $\text{AMO}_3$ , where A = Ca, lanthanides, Ce, REE; and M = Al, Ti, V, Mn, Th. These perovskites have compositions of:

Ti-rich perovskite:



Al-rich perovskite:



Thorianite is present as  $(\text{Th}_{0.83}\text{Ce}_{0.11}\text{Ti}_{0.02}\text{Zr}_{0.02})\text{O}_2$ .

Table 2-7 shows the results of a modal analysis by EMPA of the phases in A-2 a sample representative of the crushed recemented slag. The analysis employed a count of 1760 points on a thin section. The uranium and thorium are found in a Ca-Ti perovskite which makes up 2.3% of the sample, in Nb, Th, Ce phases (perovskite, zirconolite, pyrochlore, thorianite) which make up 9.3% of the slag. The other dominant, but non-radioactive phases include quartz or cristobalite (5.1%), a hibonite-like Al-Ca phase (24.2%), ground mass containing primarily Si, Ca, and Al (32.4%), and void spaces (20.2%).

Quantitative WDS analyses of the phases in the Site A samples are presented in Table 2-8. Samples 96F-A-4 (unleached) (Figure 2-14) and sample 96F-A-1-727 (leached in deionized water) depict crushed Site A slag provided by A. Felmy, PNNL. Splits of these samples were used in the PNNL experiments. The samples, both unleached and leached, were subsequently mounted in epoxy, polished and analyzed by SEM and EDS at Johns Hopkins University to investigate changes to the leached slags.

Figure 2-14 shows a BSE image and EDS spectra of unleached sample from Site A's crushed and recemented slag (96F-A-4). Perovskite is found as small white dendritic crystals within a large grain of glass. Hibonite appears as a large (400  $\mu\text{m}$ ) lath in the lower center of the BSE image and it encloses bright crystals of pyrochlore.

### 2.5.5 Scanning Electron Microprobe and Electron Microprobe Analysis - Results Site B

Modal abundance of major phases in a representative sample of Site B slag was determined by counting 2000 points per slide, from four slides using a JEOL Super probe. They are as reported in Table 2-9. The dominant phases in these slides are gehlenite 38.8%, glass 36.3%, clinopyroxene 10.1%, perovskite 9.5%, and calzirtite 4.4%. Uranium and thorium were found in the glass, perovskite, calzirtite, a weathering rind of Ba aluminite, and in thorianite and pyrochlore which were present in only a trace amount (0.1%). Void space is significantly lower than the Site A sample and in this case it makes up 2.1% of the sample. In contrast the void space made up 20.2% of the Site A sample which represented the crushed recemented slag. Table 2-10 shows the  $\text{UO}_2$  and  $\text{ThO}_2$  content of selected phases from Site B samples.

The principal silicate phases in Site B's Sn and Nb-Ta slags consist of silicate glass, gehlenite, and clinopyroxene. Of the silicate phases, only glass contains any significant amount of radioactive elements (U, Th). The glass also contains abundant rare earth elements (REE). In several samples, the glass appears to be altered to wollastonite, feldspar and/or perhaps a high Al-pyroxene and a Ce, Th-silicate (Figure 2-7). These secondary silicate phases are less than 1  $\mu\text{m}$  and are too small to be

accurately analyzed by the microprobe at Johns Hopkins University.

The principal oxide phases in the Site B slags are rutile, hibonite, spinel, perovskite, calzirtite or zirconolite, and pyrochlore minerals. U and Th are contained in the perovskite, calzirtite and pyrochlore. Hibonite contains Ce. The chemical compositions of the major crystalline phases are reported in Table 2-10. X-ray maps (Figure 2-15) provide striking visual evidence for the presence or absence of uranium and thorium in the various slag phases. The maps clearly indicate that thorium is concentrated in perovskite, calzirtite, and glass, while uranium is concentrated in calzirtite and glass.

Several of the phases analyzed do not fit stoichiometrically into any mineral formula, making conclusive identification difficult with the microprobe alone. The Ti-Zr- high Al- clinopyroxene does not fit the formula of 4.00 cations per 6.00 oxygens for a stoichiometric pyroxene. These pyroxenes have total cations that range from 3.51 to 3.90. However, optical properties, diffraction patterns, and d-spacings all indicate the presence of a pyroxene in the slag. For this reason, selected samples were analyzed with the TEM for more accurate phase identification and TEM analysis proved the unknown phase to be pyroxene.

### 2.5.6 Scanning Electron Microprobe and Electron Microprobe Analysis Results - Site C

Site C slags (C-1a, C-1b, C-5a, C-5b, C-6a, C-S) were analyzed by SEM, coupled with EDS. Site C's Group 1 slag (glassy slag) is composed primarily of a Ca-Si-Al glass and  $\text{SiO}_2$  in the form of dendrites and large (~300  $\mu\text{m}$ ) rounded blebs. Cracks formed by the change in volume as the  $\text{SiO}_2$  was transformed from cristobalite to quartz are quite noticeable in microprobe images (Figure 2-8). The silicate glass, rich in Ca, Al and Fe (with accessory amounts of K, Mn and Mg), is devitrified in certain areas and has recrystallized as wollastonite and Fe oxide and Ni silicates.

A modal analysis of phases present in a representative sample from Site C is shown in Table 2-9. Uranium and thorium are found in glass which makes up only 0.3% of the sample, and perovskite-pyrochlore which is 9.2% of the sample. Other major phases include an unidentified alteration product (25.3%), wollastonite and monticellite (27.9%), spinel (22.6%), (periclase 9.4%). Void space represents 5.0% of the sample.

Site C's Group 2 slag (dense blocky slag) contains primarily spinel, olivine and oxides. The red cubic crystals in Figure 2-9 are Al-Mg-Cr spinels. Perovskite, thorianite and other oxide phases are also present. A small amount of thorium is contained in the perovskite. The dense blocky samples also contain pyrite nodules and Fe-Ni prills. Perovskite appears to be the only mineral containing Th. The slag is oxidized and the glass, which is normally clear, has been altered from blue or green to brown and contains small microlites of Fe oxyhydroxides.

EMPA was used for detailed chemical analysis of the dominant phases in samples C-4 and C-6 and the results are shown in Table 2-11. Analyses were done of the core and the altered edges of several of the phases chosen to see patterns associated with alteration of the material.

## 2.6 Transmission Electron Microscopy

Slag from the three sites was investigated using a Philips 420 Transmission Electron Microscope and Philips 300 kV field-emission-gun TEM. The TEM was used to obtain high magnification and high resolution images, electron diffraction patterns, and small scale elemental analyses for the samples. Two methods of sample preparation were employed. The first method involved crushing a small portion of the slag in alcohol to make a suspension and then dipping a sample grid with a carbon support film into the suspension. The second method involved gluing a copper TEM grid to a small area of a thin section and then ion-milling a portion of the sample to electron transparency. Figures 2-16 and 2-17 provide an illustration of how a thin section is prepared as a TEM sample. Figure 2-16 shows three images of a portion of thin section. In (a), an area of interest is identified in plane-polarized light, (b) the same area in cross-polarized light, and (c) provides chemical information in the BSE image. Figure 2-17 is a plane polarized light micrograph of the same area in Figure 2-16, to which a TEM grid was glued to the thin section and a hole was made in the center of the grid with an ion-mill. A-A' is a cross-section of the TEM sample. Sample sizes for both methods are either 2.3 or 3.0 mm in diameter depending on the grid used. Because of the small grid size, TEM observations are not meant to be applied to the bulk sample, but are extremely helpful in identifying and describing individual phases. Electron diffraction patterns of unknown phases can be measured and converted to lattice spacings which are then compared to crystallographic databases, thus identifying unknown components of the slags. These identifications are supported by an analytical system (EDS) that provides elemental spectra for the small grains in the sample. Devitrification of glass and alteration along grain boundaries can be explored with TEM, as in Figure 2-18.

The electron microprobe provides excellent chemical analyses of points >1.0 micrometer in size. However, it provides no information on the crystal structure, and hence is difficult to determine mineral chemistry. A combination of EMPA, XRD and TEM provides the necessary information to determine crystal chemistry and structure.

The TEM has been used in this study to positively identify hibonite, Ba aluminate, Ti-Al-Zr clinopyroxene, perovskite, calzirtite and zirconolite. Hibonite contains Ce and trace amounts of Th. Perovskite, calzirtite, and zirconolite contain varying amounts of U and Th. TEM analyses of the glass provided data on the elemental composition of small areas now devitrified. Devitrification of the glass

produced small crystallites of Ce silicates, wollastonite, and voids.

Future TEM studies could investigate the phase interfaces as well as the presence of structural defects within individual crystals. Crystalline defects often serve as conduits for leaching fluids. Crystal defects are also a starting point for the breakdown of a phase. Information about the mineralogy as well as the types of defects and their relative concentrations should provide insight into the leaching rates and solubility of U and Th in the slag.

## 2.7 Surface Area Analyses: Methods and Results

Surface area analyses were performed by L. Veblen at the Johns Hopkins University to assist A. Felmy, PNNL, in interpreting the slag solubility and leaching studies performed by PNNL. The surface area of powdered slags was measured using a BET Surface Area Analyzer. Three of the Site B samples (96TC19F, 96TC20F, and 96TC21F) provided by PNNL were analyzed. These were powdered (crushed) samples that they used in the PNNL leaching experiments. The surface area varied among samples and it ranged from 0.166 m<sup>2</sup>/g for 96TC19F to 0.6 m<sup>2</sup>/g for 96TC20F to approximately 1.0 m<sup>2</sup>/g for 96TC21F. Intact samples could be measured, with a new sample holder that allows larger (cm sized) samples.

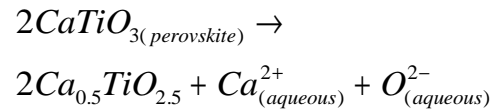
## 2.8 Petrology of the Slags

Based on the XRF bulk chemical analyses and the mineralogy of the Sn, and Nb-Ta slags, it is possible to classify the slag into discrete chemictypes as seen in the Ternary Diagram (Figure 2-10). Additional analyses by the microprobe, XRF, and TEM data should enable one to define petrologically a "typical" Nb-Ta slag, and thereby classify additional Nb-Ta slags based solely on bulk chemical analyses. A similar method of classification is commonly used in igneous petrology. This classification, based on bulk chemical composition, may be used in the future by licensees to place bounds on the weathering characteristics of the materials on site without the detailed solid phase characterization done in this report. For example: if one had a phase diagram for the production of slag, given a bulk composition, the crystalline phases could be predicted. This information could be used along with individual mineral weathering or degradation information to estimate leach rates.

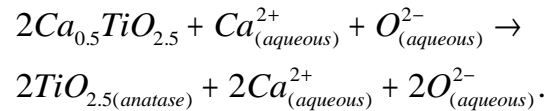
Table 2-12 summarizes the principal phases and their corresponding amounts present in the slags at the three sites. This table also provides information on the weight percent of U and Th in each phase which can in turn be used in estimating leach rates. Sites A, B, and C share many phases. All three sites contain hibonite, perovskite, and Site A contains considerable thorianite. There is not much glass at Site A but this is understandable because the Site A material was crushed and processed with acid. Under such conditions the glass is not expected to survive.

The Site B slags that contribute the greatest radioactivity to the source term have been characterized chemically and mineralogically. There appear to be two slag types that contribute most to radioactivity at the site. These are the Sn slag (e.g. B-5.5) which had been brought from Malaysia and the Nb-Ta slag which was a waste product following the extraction of Nb-Ta from the original Sn slag. Both slags have similar chemical composition, and hence similar crystalline phases. The primary silicates of both are gehlenite (a Ca rich melilite), clinopyroxene (there appear to be two distinct high Al pyroxenes), wollastonite, and silicate glass. The secondary minerals include feldspar, Ce silicate, and quartz, and they formed by devitrification of the glass or from alteration of the glass and primary crystalline phases. Quartz is also included as a xenocryst from the physical process of smelting. The original feed materials sat on a quartz-sand bed. Zirconolite and hibonite were most likely the first phases to crystallize from the melt (Figure 2-19). Hibonite, spinel, perovskite, calzirtite and/or zirconolite, and pyrochlore are the oxides present and appear to be the primary phases. Rutile is present, but may be a secondary alteration phase of perovskite. Perovskite is not stable under low temperature, atmospheric conditions, and will eventually alter to rutile or anatase. The alteration proceeds via incongruent

dissolution of the Ca ions, followed by a transitional CaTiO phase according to the following reactions (Banfield and Veblen, 1992):



and



Site C has two main types of slag based on mineralogy. One characteristically contains Ba aluminate, hibonite, and perovskite. Radioisotopes of Th are typically found in the perovskite. The second slag type contains spinel, olvine, and perovskite. Site C is similar to Site A in that there is Ba aluminate present at both sites along with hibonite or a hibonite-like phase, perovskite and thorianite. Site C has some glass. As noted above, there is little glass at Site A because the acid leaching during refining of the material would remove glass.

Table 2-1 Hand Specimen Description	
Sample Number	Description
<b>Site A Samples</b>	
 A-1	Crushed, naturally cemented slag, specific gravity approximately that of sandstone. Resembles a sandstone with cross bedding and some graded bedding. Grain size ranges from <1mm to 1mm. Has some voids <1mm which are probably depositional structures rather than voids caused by weathering. Fresh surfaces are white (N/8/0) and light gray (N/7/0). Has a thin goethite like weathering rind typically 1 - 2mm thick but up to 10mm in places. Color of rind ranges from gray (*Munsell color 10YR/6/1) to brownish yellow (*Munsell color 10YR/6/6) to strong brown (*Munsell color 7.5YR/4/6). Radioactivity 3200 counts/minute.**
 A-2	Crushed, naturally cemented slag. Almost identical to A-1 except that portions of the weathering rind are greenish gray (*Munsell color 10G/6/1) in addition to the colors noted under A-1. Radioactivity 4000 counts/minute.**
<b>Site B Samples</b>	
B 1-4	Slag, high specific gravity, surface vitreous, vesicles <1mm and make up 5% of sample. Elongate crystal laths greenish gray in color stand out on a weathered surface. Color is greenish gray (*Munsell color 10Y/5/1).
 B- 5-5	Slag, high specific gravity, very glassy. Numerous crystals stand out on weathered surface. Fresh surfaces are very dark gray (*Munsell color N/3/0). Outer weathered surface is pale yellow (*Munsell color 2.5Y/7/3). Gamma Radioactivity 4000 counts/minute.**
 B- 5.5b	Slag, high specific gravity, crystalline with the crystals. Small vesicles <1mm are visible on weathered edge and make up ~5% of volume. Color of fresh surface is gray (*Munsell color N/5/0) weathers to light gray (*Munsell color 10YR/7/2). Radioactivity 4000 counts/minute.**
 B- 5-8	Slag, high specific gravity. Numerous vesicles <1mm to 10mm in diameter toward one surface. Make up ~ 40% of the volume at that surface. Numerous euhedral crystals 1 - 2mm on the edge with vesicles. Color is gray (*Munsell color N/5/0/N) on fresh surface and on weathered surfaces it is light brownish gray (*Munsell color 10YR/6/2). Radioactivity 3600 counts/minute.**
 B- 5-9	Slag, high specific gravity, fine grained, dense. Fresh surface dark gray (*Munsell color N/4/0). Weathers to a light gray (*Munsell color 2.5Y/7/2). Radioactivity 3000 counts/minute.**
 B- 5-10	Slag, high specific gravity, finely crystalline. Very dark gray (*Munsell color N/3/0/N) weathers to light gray (*Munsell color 2.5Y/7/2). Large vesicles ranging in size from < 1mm to >100mm on one surface. Radioactivity 2000 counts/minute.**
 B- 5-11	Slag, high specific gravity, finely crystalline with abundant glass particularly close to cooling surface. Fresh surfaces are dark bluish gray (*Munsell color 5B/3/1). Weathering surface is red (*Munsell color 10R/4/6). Radioactivity 2200 counts/minute.**
 B- 5-11	Slag, high specific gravity, finely crystalline with an abundance of metallic prills <1mm to ~5mm. Has tiny vesicles <1mm throughout and represent ~10% of volume. Color on fresh surfaces is dark gray (*Munsell color N/4/0). Weathering surface is red (*Munsell color 10R/4/6). Radioactivity 2200 counts/minute.**
B- 1	Possibly crushed slag. Very fine grains <1mm in size with quartz and slag fragments 1 - 2mm in diameter. Color is dark greenish gray (*Munsell color 10Y/4/1)
B- 2	Possibly crushed slag. Poorly lithified. Contains about 5% of light colored angular fragments which are possibly crushed fire brick or concrete up to 10mm in diameter. Color is gray (*Munsell color N/5/0) .
B- 3	Fine grained dense metal. Silvery metallic on fresh surfaces some of which oxidized after cutting to a light red (*Munsell color 10R/6/8). Fresh surfaces are gray (N/5/0) and weathered surfaces are dark reddish brown (*Munsell color 2.5Y/3/3).

<b>Table 2-1 Hand Specimen Description</b>	
<b>Sample Number</b>	<b>Description</b>
B- 4	Ore like material. Very fine grained with grains <1mm. Has a 10mm thick lens of very fine <1mm euhedral pyrite crystals. Lens is centimeters long. Color is very dark gray (*Munsell color N/3/0) and the sample weathers to a yellowish red (*Munsell color 5YR/4/6) goethite like material.
B- 5.3	May be a weathered slag. High specific gravity which is made up of fairly uniform very fine grained grains <1mm in diameter. Vesicles <1mm in diameter make up <1% of sample. Fresh surfaces are very dark gray (*Munsell color 5YR/3/1) and the outer surfaces is weathered to a goethite like material which is light brown (*Munsell color 7.5YR/6/4).
B- 5-5	Slag, high specific gravity. Glassy and fine grained made up of subhedral to euhedral black grains. Has minor amount (<1%) round metallic prills and some of them have weathered to a goethite like material. Color is dark gray (*Munsell color N/4/0).
B- 6	Possible ore, high specific gravity. On a polished surface there were numerous filament like silvery metallic veins 2 - 5mm thick and cm long. Matrix between the veins is dark reddish gray (*Munsell color 10R/4/1). Fresh surfaces are gray (*Munsell color N/5/0) and the outer weathered surface is a weak red (*Munsell color 10YR/5/3). Very small vesicles <1mm make up ~5% of the material.
B- 7	Slag, specific gravity about that of sedimentary rock. About 3% of sample consists of sub angular to rounded quartz grains <1mm in diameter. Has thin glassy rind about 10mm thick. Many vesicles <1mm are present and make up 15% of the sample. The outer surface has vesicles 1 - 2mm in diameter. Cut surface is dark metallic gray (*Munsell color N/4/0) and the outer surface is gray (*Munsell color N/5/0).
96T-C-9C	Crushed sample with angular fragments approximately 2mm in length. Looks like a devitrified slag. Some glass fragments present. Unweathered surfaces are black. Overall color is grayish brown (*Munsell color 10YR/5/2) and probably represents weathered surfaces.
96 T-C-19C	Crushed sample of slag with angular fragments 2 - 20mm in length. Made up of subeuhedral to euhedral dark glassy grains. Vesicles <1mm in diameter are about 2% of sample. Needle like laths stand out in relief on weathered surfaces. Color is dark gray (*Munsell color N/4/0) and the material weathers to gray (*Munsell color 5YR/5/1).
96 T-C-20C	Crushed sample of slag consisting of angular fragments 2 - 10mm in length. It's very glassy. Vesicles <1mm in diameter make up ~3% of sample. Unweathered surfaces range from very dark gray (*Munsell color N/3/0 to black (*Munsell color N/2.5/0). Weathered surfaces are weak red (*Munsell color 10R/4/2).
<b>Site C Samples</b>	
 C-1	Slag, very high specific gravity. Large lath like crystals up to 10 mm long visible in cut surface and the ends of the laths are very prominent on weathered surface where they stand in relief. Has other smaller crystals <1mm at cooling surface. Fresh surfaces are dark bluish gray (*Munsell color 10B/4/1) to bluish black (*Munsell color 10B/2.5/1). There is a weathering rind 1 to 5mm thick with a range of colors including lightish green gray (*Munsell color 10Y/8/1), grayish brown (*Munsell color 2.5Y/5/2), to white (*Munsell color N/8/0). Radioactivity 5000 - 8000 counts/minute.**
 C-2	Slag, very high specific gravity. Very fine grained. Lots of metallic prills <1mm which are about 20% of sample. Fresh surface is dark bluish gray (*Munsell color 5PB/4/1). There is a thin weathering rind <1mm thick with a range of colors including dark gray (*Munsell color 5Y/4/1), light gray (5Y/7/2), light gray (*Munsell color 2.5Y/7/2) and light gray (*Munsell color 2.5Y/7/1). Radioactivity 8000 counts/minute.**
 C-3	Slag, high specific gravity. Description the same as C-2 except the metallic prills are missing and large laths stand in relief on weathering surfaces. Radioactivity 600 counts/minute.**

Table 2-1 Hand Specimen Description	
Sample Number	Description
 C-4	Slag, specific gravity similar to sandstone. Resembles C-6. Made up of equant grains <1mm in diameter. Has some vesicles up to 3mm in diameter and they represent ~5% of the sample. Metallic prills along the edge are <1mm in diameter and make up around 1% of the area. Exterior surface very fractured and it resembles mud cracks (dehydration cracking). Fresh surface is light bluish gray (*Munsell color 5PB/7/1). Weathered pretty much throughout the sample and the outer surface is light greenish gray (*Munsell color 10Y/7/1) and almost white (*Munsell color N/8/1). Radioactivity 650 counts/minute.**
 C-5	Slag, resembles green obsidian. Specific gravity the same as obsidian. Has some prills. On the edge they are up to 2mm in diameter. Inside they are <1mm. Fresh surfaces is grayish green (*Munsell color 5G/4/2). It is devitified along the edge and the color is light greenish gray (*Munsell color 5GY/7/1). Other portions of the weathered edge is pale brown (*Munsell color 10YR/6/3) and yellowish brown (*Munsell color 10YR/5/4). Radioactivity 100 counts/minute.**
C- 5a	Sample chips, angular 2mm to 10mm in diameter. Fine grained with vesicles <1mm making up about 5% of volume. Color is gray (*Munsell color N/5/0). Weathers to light gray (*Munsell color 2.5Y/7/2).
 C-6	Slag, specific gravity moderate, highly weathered. Similar in appearance to C-4. Exterior surface very fractured and it resembles mud cracks (dehydration cracking). Has some prills <1mm in diameter throughout the sample. Very fine grained with grains <1mm. Has very fine equant crystals green in color. Fresh surface is light greenish gray (*Munsell color 5GY/8/1) and the exterior weathered surface is close to white (*Munsell color N/8/0). Radioactivity 2000 counts/minute.**
* Color description is based on Munsell Soil Color Charts, 1994 revised edition, Macbeth Division of Kollmorgen Instruments Corporation, New Windsor, New York. The order of description is hue/value/chroma.	
** Radioactivity measured with a 5 cm (2") pancake type Geiger Muller probe.	

<b>Table 2-2 Measurements of Samples with Detectable Radioactivity</b>		
<b>Site and Sample number</b>	<b>☢ Bichron <math>\mu</math>Sv/hour</b>	<b>☢ Contact counts per minute</b>
Laboratory background	0.05	
<b>Site A</b>		
A-1		3200
A-2 (alteration product)	3.0	4000
A-2		7000
A-2		4000
<b>Site B</b>		
B-1		100
B-5		3000
B-5.5	4.0	4000
B-5.5	4.5	4000
B-5.8	4.0	3600
B-5.9		3000
B-5.10		2000
B-5.11		2500
B-5.11		2200
Green slag		100
<b>Site C</b>		
C1	5.0	5000-8000
C2	3.5	8000
C3	2.5	600
C4	0.25	650
C5	0.05	100
C6		2000

Table 2-3 Phases Present in Samples from Sites A, B, and C				
Phase	Ideal formula	Site A	Site B	Site C
 Calzirtite*	$(Ca,U,Th)ZrTi_2O_7$	x	x	x
 Zirconolite*	$(Ca,Th,Ce)Zr(Ti,Nb)_2O_7$	x	x	x
 Perovskite*	$CaTiO_3$	x	x	x
 Perovskite (Loparite)	$(Ca,Ce,Th)(Ti,Nb)O_3$	x		x
 Zirconolite	$(Ca_{2.45}Th_{0.03}REE_{0.04})Zr_{0.34}Al_{0.30}Ti_{1.24}Nb_{0.15}Ta_{0.12}O_7$		x	x
 Zirconolite	$(Ca_{1.18}Ce_{0.61}Th_{0.11}REE_{0.26})Zr_{0.02}Al_{1.17}Ti_{1.14}Nb_{0.08}O_7$		x	x
 Pyrochlore (Betafite)	$(Ca,U,Ce)_2(Nb,Ti)_2O_6$	x		x
 Pyrochlore	$(Ca,Th,Ce)_2(Nb,Ti)_2O_6$	x	x	x
 Glass	Si,Al,Ca,Ti,U,Th	trace	x	x
 Hibonite	$(Ca,Ce)_9(Ti,Al)_{12}O_{19}$	x	x	x
 Barium Aluminate*	$Ba,Ce(Ti,Al)_{12}O_{19}$	x		x
Spinel*	$AB_2O_4$ A = Co, Fe, Mg, Mn, Ni B = Al, Cr, Fe, Mg, Mn, V	x	x	x
 Thorianite	$ThO_2$ (note: forms a series with uranite ( $UO_2$ ))	x	?	?
 Thorite	$(Th,U)SiO_4$	x	?	?
Periclase	MgO			x
Wustite	FeO			x
Monticellite (olivine)	$CaMgSiO_4$			x
Gehlenite	$Ca_2Al(AlSi)O_7$	x	x	x
Melilite	$(Ca,Na)_2(Mg,Fe,Al,Si)_3O_7$		x	
Clinopyroxene	$Ca(Zr,Ti,Al)(Al,Si,Ti)_2O_6$		x	
Feldspar	$CaAl_2Si_2O_8$	x	x	x
Wollastonite	$CaSiO_3$		x	
 Ce-Silicate	Ce,Si		x	
 Ce-Aluminosilicate	Ce,Si,Al		x	
Barium Aluminosilicate	$BaAl_2Si_2O_8$	x		
Gypsum	$Ca(SO)_4$	x		

<b>Table 2-3 Phases Present in Samples from Sites A, B, and C</b>				
<b>Phase</b>	<b>Ideal formula</b>	<b>Site A</b>	<b>Site B</b>	<b>Site C</b>
Tridymite	SiO <sub>2</sub>	x	x	x
Groundmass	Ca,Ba,Al; Ca,Ba,S,Cl,Al	x		
☢ indicates some radioactivity may be present				
* indicates SYNROC phases				

**Table 2-4 Chemical Composition of Major Elements in Slag Samples (weight %) as determined by XRF.**

(Blank = not analyzed; ? = undefined amount; n.d. = not detected)

	Site A		Site B										Site C	
	A-1	A-2	B-5	B-5.5	B-8(1)	B-5-5A	B-5-5B	B-5-5C avg	B-5-8	B-5-11	B-4 (soil)	B-9 (soil)	B- glass	C-5a
SiO <sub>2</sub>	18.01	10.73	25.47	25.85	38.42	26.40	28.59	28.76	29.79	26.50	62.26	50.19	58.67	18.63
TiO <sub>2</sub>	2.06	2.75	8.61	11.40	1.04	13.62	6.81	6.79	6.43	9.86	0.54	1.46	0.26	2.34
Al <sub>2</sub> O <sub>2</sub>	41.87	46.65	14.11	13.35	23.54	15.10	16.78	16.90	16.30	14.38	10.51	5.64	3.34	13.42
Fe <sub>2</sub> O <sub>3</sub>	n.d.	n.d.	0.66	0.22	20.65	0.57	0.06	0.05	0.01	2.20	10.90	4.48	0.73	0.20
FeO	1.22	0.54	0.62	1.78	7.68	N.d.	n.d.	n.d.	n.d.	n.d.	1.03	3.13	2.60	1.53
MnO	0.07	0.05	0.61	0.54	0.15	0.49	0.51	0.51	0.69	0.74	0.01	0.24	14.56	0.59
MgO	0.22	0.24	1.54	1.51	0.80	1.52	1.76	1.76	2.27	1.77	0.52	2.05	0.19	17.50
CaO	11.53	11.32	28.92	26.80	3.50	29.17	32.65	32.72	31.77	27.81	0.10	9.71	10.94	19.93
Na <sub>2</sub> O	0.72	0.80	0.17	0.13	0.68	0.11	0.09	0.10	0.11	0.14	0.30	0.33	0.05	0.26
K <sub>2</sub> O	0.06	0.07	0.22	0.23	1.24	0.16	0.19	0.20	0.29	0.22	1.65	0.96	0.08	0.10
P <sub>2</sub> O <sub>5</sub>	0.01	0.01	0.04	0.21	0.45	0.05	0.01	0.01	0.01	0.26	0.05	0.16	0.03	0.02
CuO														0.08
ZnO														0.01
SO <sub>2</sub>														1.01
Total	75.77	73.16	80.97	82.02	98.15	87.19	87.45	87.78	87.67	83.88	87.87	78.35	91.45	75.62
LOI	20.53	23.24	0.20	-3.80	0.43	5.35	-0.32	-0.33	-0.37	-3.11	9.69	20.74		
Fe <sub>2</sub> O <sub>3</sub> total	1.36	0.60	1.35	2.20	29.19	0.57	0.06	0.05	0.01	2.20	12.04	7.96		

**Table 2-5 Chemical Composition of Trace Elements in Slag Samples (ppm) as determined by XRF.**

(Blank = not analyzed; ? = undefined amount; n.d. = not detected)

Site A		Site B											Site C	
	A-1	A-2	B-5	B-5.5	B-8(1)	B-5-5A	B-5-5B	B-5-5C avg	B-5-8	B-5-11	B-4 (soil)	B-9 (soil)	B- glass	C-5
Rb	45.0	67.0	15.0	?	63.0	24.0	23.0	21	33.0	?	86.0	22.0	7	5
Sr	373	474	258	240	1570	230	271	269.5	265	245	74	134	72	295
Ba	40600	61800	905	1125	1530	1240	1300	1325	1300	1250	472	127	115	0
Y	96	109	3850	?	60	3250	5400	5300	5300	?	23	91	7	15
Zr	?	?	21000	?	217	18000	41000	40250	40000	?	157	940	173	675
V	75	105	102	275	230	183	55	50	54	234	61	192	38	305
Ni	20	21	57	52	86	40	44	41.5	43	42	54	155	5	670
Cr	?	?	154	387	223	233	19	1	24	395	39	584	890	25850
Nb	12400	12200	1150	7000	25.8	1250	12?	13.5?	5?	6400	12.3	1026	5	1440
Ga	n.d.	n.d.	3.2	139	21.6	18.0	?	?	?	145	28.9	33.6	0	0
Cu	45	39	?	?	102	?	?	?	?	?	42	2420	231	105
Zn	37	23	15	16	117	11	?	?	?	?	60	4390	22	200
 U	213	280	180	1980	9.1	225.0	?	?	?	1920	2.9	18.0	1	15
 Th	10250	13250	3960	3650	22.8	3640.0	4400.0	4225	4200	4100	1.8	84.5	0	
Co	?	?	?	?	28	4	1	2	3	2	31	18	0	19
La	2600	2750	?	?	67	3900	5000	4725	4600	4600	41	138	10	3
Ce	6400	6500	?	?	168	?	?	?	?	?	120	351	12	9
Sc													7	
Pb	34	?				?	?	?	?	?			18	

**Table 2-6 List of minerals indicated by X-Ray Diffraction analysis of Site B Sample B-5.5a.**

Mineral	Formula
Gehlenite	$\text{Ca}_2\text{Al}_2\text{SiO}_7$
Schorlomite	$\text{Ca}_3(\text{Fe}, \text{Ti})_2[(\text{Si}, \text{Ti})\text{O}_4]_3$
Kimzeyite	$\text{Ca}_3(\text{Zr}, \text{Fe}, \text{Ti})_2[(\text{Al}, \text{Si}, \text{Fe})\text{O}_4]_3$
Grossular	$\text{Ca}_3\text{Al}_2(\text{SiO}_4)_3$
Goldmanite	$\text{Ca}_3(\text{V}, \text{Fe}, \text{Al})_2(\text{SiO}_4)_3$
Epidote	$\text{Ca}_2\text{Al}_2\text{Fe}(\text{SiO}_4)(\text{Si}_2\text{O}_7)(\text{O}, \text{OH})$
Rutile	$(\text{Ti}, \text{Nb}, \text{Ta}, \text{Fe})\text{O}_2$
Struverite	$(\text{Ti}, \text{Ta}, \text{Fe})\text{O}_2$
Ilmenorutile	$\text{Fe}_x(\text{Nb}, \text{Ta})_{2x}\text{Ti}_{1-x}\text{O}_2$
Ashanite	$(\text{Nb}, \text{Ta}, \text{U}, \text{Fe}, \text{Mn})\text{O}_2$
Wodgnite	$(\text{Ta}, \text{Mn}, \text{Sn}, \text{Nb})\text{O}_2$
Srilankite	$(\text{Ti}, \text{Zr})\text{O}_2$ (synthetic)
Ixiolite	$(\text{Ta}, \text{Fe}, \text{Sn}, \text{Nb}, \text{Mn})\text{O}_2$
Alumotantite	$\text{AlTaO}_4$
Thorite	$(\text{Th}, \text{U})\text{SiO}_4$
Aeschnynite	$(\text{Ce}, \text{Ca}, \text{Fe}, \text{Th})(\text{Ti}, \text{Nb})_2(\text{O}, \text{OH})_6$
Vigezzite	$(\text{Ca}, \text{Ce})(\text{Nb}, \text{Ta}, \text{Ti})_2\text{O}_6$
Tantalaeschnynite	$(\text{Y}, \text{Ce}, \text{Ca})(\text{Ta}, \text{Ti}, \text{Nb})_2\text{O}_6$
Niobo-aseschnynite	$(\text{Ce}, \text{Ca}, \text{Th})(\text{Nb}, \text{Ti})_2(\text{O}, \text{OH})_6$
Rynersonite	$\text{Ca}(\text{Ta}, \text{Nb})_2\text{O}_6$
Staringite	$(\text{Sn}, \text{Fe})(\text{Sn}, \text{Ta}, \text{Nb})_2\text{O}_6$
Manganotapiolite	$(\text{Mn}, \text{Fe})(\text{Ta}, \text{Nb})_2\text{O}_6$
Ferrotapiolite	$(\text{Fe}^{+2}, \text{Mn}^{+2})(\text{Ta}, \text{Nb})_2\text{O}_6$
Fersmite	$(\text{Ca}, \text{Ce}, \text{Na})(\text{Nb}, \text{Ta}, \text{Ti})_2(\text{O}, \text{OH}, \text{F})_6$
Ferrocolumbite	$(\text{Fe}, \text{Mn})(\text{Nb})_2\text{O}_6$
Euxenite	$(\text{Y}, \text{Ca}, \text{Ce}, \text{U}, \text{Th})(\text{Nb}, \text{Ta}, \text{Ti})_2\text{O}_6$
Zirconolite	$\text{CaZrTi}_2\text{O}_7$
Ytropyrochlore	$(\text{Y}, \text{Na}, \text{Ca}, \text{U})_{1-2}(\text{Nb}, \text{Ta}, \text{Ti})_2(\text{O}, \text{OH})_7$
Calzirtite	$\text{CaZr}_3\text{TiO}_9$
Tantalcarbide	$(\text{Ta}, \text{Nb})\text{C}$
Kamacite	$(\text{Fe}, \text{Ni})$
unnamed mineral	WC
Moissanite	SiC

The JADE database was used for this peak based search. This list indicates the complexity in identifying mineral phases based solely on x-ray diffraction data. The JADE data are for pure phases. However, the phases in the slags are not pure end members. They contain elements such as thorium, uranium, and REE (rare earth elements) that are not present in the materials within the JADE database.

**Table 2-7 Modal Abundance of Phases in Representative Site A Slag Sample as determined by Electron Microprobe Analysis (EMPA).**

<b>Phase</b>	<b>Modal Abundance (1760 points)</b>
Si only (Quartz or Cristobalite)	5.1%
Al-Ca phases (Hibonite-like)	24.2%
Ca-Al phases (small amounts of Cl)	3.7%
Si-Al, Ca) (glass and silicates)	2.5%
 <b>Ca-Ti phases (Perovskite)*</b>	2.3%
 <b>Nb, Th, Ce-phases (Perovskite, Zirconolite, Pyrochlore, Thorianite) *</b>	9.3%
Fe phases (Ba, Al, Si, Ca, Ti, Mg, Ce, Cl)	0.4%
Groundmass (contains primarily Si, Ca, and Al)	32.4%
Voids and fractures	20.2%
 * uranium and thorium bearing phases in bold type	

**Table 2-8 Average Chemical Composition (weight %) of Most Common Phases Site A Samples as Determined by Electron Microprobe Analysis (EMPA).**

	<b>Perovskite</b> (average of 13 samples)	<b>Thorianite</b> (average of 5 samples)	<b>Calzirtite</b> (average of 2 samples)	<b>Barium Aluminate</b> (average of 4 samples)
Na <sub>2</sub> O	0.83	0.01		0.42
MgO	0.03	0.03	0.13	0.06
Al <sub>2</sub> O <sub>3</sub>	0.83	0.04	1.01	5.02
SiO <sub>2</sub>	0.00	0.00	0.34	0.11
P <sub>2</sub> O <sub>5</sub>	-----	-----	-----	-----
K <sub>2</sub> O	0.09	0.14	0.10	0.11
CaO	16.12	0.10	19.31	11.84
TiO <sub>2</sub>	23.21	0.71	29.07	17.67
Cr <sub>2</sub> O <sub>3</sub>	0.00	0.00	0.00	0.00
MnO	0.01	0.001	0.18	0.06
FeO	0.01	0.05	0.001	0.02
Y <sub>2</sub> O <sub>3</sub>	0.08	0.05	0.98	0.37
ZrO <sub>2</sub>	0.68	0.45	33.1	11.41
BaO	0.34	0	0.21	0.18
La <sub>2</sub> O <sub>3</sub>	3.13	0.38	1.44	1.65
Ce <sub>2</sub> O <sub>3</sub>	22.51	5.63	4.01	10.76
Pr <sub>2</sub> O <sub>3</sub>	1.18	0.40	0.55	0.71
Nd <sub>2</sub> O <sub>3</sub>	2.82	0.95	1.84	1.87
Sm <sub>2</sub> O <sub>3</sub>	0.20	0.08	0.26	0.18
Gd <sub>2</sub> O <sub>3</sub>	1.65	0.45	0.57	0.89
Dy <sub>2</sub> O <sub>3</sub>	0.04	0.01	0.23	0.09
Er <sub>2</sub> O <sub>3</sub>	0.01	0.01	0.14	0.05
Yb <sub>2</sub> O <sub>3</sub>	0.00	0.001	0.12	0.04
HfO <sub>2</sub>	0.00	0	0.75	0.25
Ta <sub>2</sub> O <sub>3</sub>	0.00	0	0.01	0.003
PbO	0.02	0.02	0.09	0.04
 ThO <sub>2</sub>	11.42	94.31	1.49	35.74
 UO <sub>2</sub>	0.12	1.99	0.72	0.94
<b>Total</b>	98.55	105.81	96.65	100.48
 UO <sub>2</sub> + ThO <sub>2</sub>	11.54	96.30	2.21	36.68

**Table 2-9 Modal Abundance of Phases in Representative Samples from Sites B and C Slag as determined by Electron Microprobe Analysis (EMPA).**

Phase	Modal Abundance) Site B		Modal Abundance Site C		
	B-5 (?) 1794 points	B-5 (?) 2000 points	C- 4 357 points	C- 4B 778 points	C- 4 947 points
Gehlenite	37.0%	38.8%			
<b>☢ Glass *</b>	36.4%	36.3%			0.3%
Wollastonite and Monticellite			28.3%	30.1%	27.9%
Spinel			21.3%	23.0%	22.6%
Clinopyroxene	9.6%	10.1%			
<b>☢ Perovskite *</b>	9.3%	9.5%	9.0%	9.8%	9.2%
<b>☢ Calzirtite + zirconolite*</b>	4.8%	4.4%			
Periclase			26.3%	22.5%	9.4%
Rutile	0.2%	1.9%			
Fe prills				0.1%	0.3%
<b>☢ Pyrochlore *</b>	0.1%	0.1%			
Alteration product	0.5%	0.4%	5.0%	14.3%	25.3%
Voids and fractures	2.2%	2.1%			5.0%
<b>☢ * uranium and thorium bearing phases in bold type</b>					

**Table 2-10 Average Chemical Composition (weight %) of Most Common Phases Site B Samples as Determined by Electron Microprobe Analysis (EMPA).**

	Perovskite	Pyrochlore)	Calzirtite Zirconolite	Melilite Gehlenite	Spinel	Hibonite	Pyroxene	Glass
Na <sub>2</sub> O	0.04	2.04	0.05	0.09	0.04	0.01	0.02	0.11
MgO	0.64	1.24	2.58	3.76	4.07	2.41	4.16	0.50
Al <sub>2</sub> O <sub>3</sub>	9.43	16.37	34.51	35.08	27.42	82.64	22.54	37.99
SiO <sub>2</sub>	22.09	1.86	11.31	22.49	3.74	0.091	24.96	16.61
P <sub>2</sub> O <sub>5</sub>	0.04	0.004	0.01	0.01	0.01	0.008	0.006	0.01
K <sub>2</sub> O	0.43	0.48	0.13	0.33	0.12	0.02	0.002	0.28
CaO	31.97	12.56	18.22	24.92	10.35	7.45	23.40	35.99
TiO <sub>2</sub>	18.60	31.90	15.13	14.39	38.39	3.81	15.38	1.96
Cr <sub>2</sub> O <sub>3</sub>	0.01	0.05	0.03	0.04	0.10	0.00	0.021	0.002
MnO	0.48	0.45	0.40	0.67	0.85	0.08	0.48	0.08
FeO	0.01	0.24	0.007	0.006	0.008	0.01	0.002	0.003
Y <sub>2</sub> O <sub>3</sub>	0.25	0.32	0.23	0.14	0.20	0.03	0.11	0.29
ZrO <sub>2</sub>	6.61	27.10	15.49	1.97	14.46	1.36	7.18	0.58
BaO	0.13	0.48	0.27	0.22	0.58	0.04	0.25	0.08
La <sub>2</sub> O <sub>3</sub>	0.86	0.18	0.24	0.14	0.02	0.81	0.07	0.36
Ce <sub>2</sub> O <sub>3</sub>	2.56	0.49	0.56	0.35	0.12	1.55	0.23	0.97
Pr <sub>2</sub> O <sub>3</sub>	0.30	0.07	0.06	0.04	0.008	0.16	0.05	0.13
Nd <sub>2</sub> O <sub>3</sub>	1.05	0.17	0.21	0.18	0.04	0.43	0.12	0.49
Sm <sub>2</sub> O <sub>3</sub>	0.21	0.06	0.06	0.05	0.04	0.06	0.02	0.12
Gd <sub>2</sub> O <sub>3</sub>	0.32	0.05	0.05	0.04	0.03	0.05	0.03	0.11
Dy <sub>2</sub> O <sub>3</sub>	0.07	0.05	0.06	0.05	0.04	0.02	0.03	0.07
Er <sub>2</sub> O <sub>3</sub>	0.04	0.06	0.04	0.01	0.03	0.01	0.22	0.03
Yb <sub>2</sub> O <sub>3</sub>	0.04	0.06	0.05	0.03	0.05	0.004	0.21	0.03
HfO <sub>2</sub>	0.03	0.94	0.52	0.00	0.59	0.005	0.22	0.00
Ta <sub>2</sub> O <sub>3</sub>	----	3.51	0.21	0.04	0.34	0.01	0.00	0.00
PbO	0.03	0.12	0.07	0.003	0.08	0.01	0.04	0.01
 ThO <sub>2</sub>	0.45	1.27	0.30	0.06	0.20	0.130	0.01	0.22
 UO <sub>2</sub>	0.08	0.39	0.16	0.005	0.11	0.007	0.01	0.03
<b>Total</b>	96.77	102.514	100.957	105.114	102.036	101.215	99.771	97.055
 UO <sub>2</sub> + ThO <sub>2</sub>	0.53	1.66	0.46	0.065	0.31	0.137	0.02	0.25

**Table 2-11 Average Chemical Composition (weight %) of Most Common Phases Site C Samples as Determined by Electron Microprobe Analysis (EMPA).**

	<b>C-6 Pyrochlore</b>	<b>C-4- Pyrochlore</b>	<b>C-6- Alteration</b>	<b>C-6 Spinel- core</b>	<b>C-6 Spinel- rim</b>	<b>C-4 Spinel- core</b>	<b>C-4 Spinel-rim</b>	<b>C-6- Periclase</b>	<b>C-4 Ba- Aluminate</b>
MgO	3.525	1.147	0.204	29.128	19.048	27.813	25.330	92.920	2.76
Al <sub>2</sub> O <sub>3</sub>	4.092	4.190	17.170	68.088	45.283	50.590	54.653	0.272	87.51999
K <sub>2</sub> O	0.064	0.081	0.048	0.045	0.046	0.045	0.045	0.055	0.5091
CaO	50.491	35.507	36.250	0.081	12.142	0.097	4.107	0.422	0.0149
TiO <sub>2</sub>	19.515	25.773	0.157	1.732	1.295	1.997	1.675	0.344	1.1162
Cr <sub>2</sub> O <sub>3</sub>	0.069	1.431	0.014	0.662	6.903	20.033	9.199	0.071	0
MnO	0.055	0.039	0.052	0.137	0.157	0.281	0.191	0.711	0.1003
FeO	0.002	0.031	0.066	0.007	0.078	0.160	0.082	0.013	0.0004
ZrO <sub>2</sub>	2.725	7.593	0.001	0.013	0.030	0.076	0.040	0.002	0
NbO <sub>2</sub>	0.038	5.380	0.000	0.001	0.008	0.022	0.010	0.000	0.001
BaO	0.219	0.211	0.000	0.010	0.007	0.011	0.009	0.000	10.3
Ce <sub>2</sub> O <sub>3</sub>	0.036	0.071	0.013	0.010	0.009	0.004	0.008	0.014	0.5384
Sm <sub>2</sub> O <sub>3</sub>	0.004	0.003	0.000	0.004	0.001	0.000	0.002	0.024	0
Er <sub>2</sub> O <sub>3</sub>	0.001	0.002	0.011	0.002	0.008	0.012	0.007	0.003	0
HfO <sub>2</sub>	0.000	1.517	0.000	0.000	0.000	0.000	0.000	0.000	0
Ta <sub>2</sub> O <sub>3</sub>	0.000	10.250	0.000	0.000	0.000	0.000	0.000	0.000	0
ThO <sub>2</sub>	0.009	2.290	0.001	0.004	0.003	0.004	0.003	0.010	0.001
UO <sub>2</sub>	0.007	0.008	0.006	0.003	0.004	0.003	0.003	0.001	0
La <sub>2</sub> O <sub>3</sub>	0.020	0.012	0.000	0.000	0.003	0.008	0.003	0.000	0
Pr <sub>2</sub> O <sub>3</sub>	0.011	0.010	0.023	0.010	0.011	0.000	0.007	0.000	0.0158
Nd <sub>2</sub> O <sub>3</sub>	0.013	0.021	0.000	0.011	0.004	0.000	0.005	0.017	0
Gd <sub>2</sub> O <sub>3</sub>	0.005	0.009	0.001	0.004	0.002	0.000	0.002	0.000	0.0011
PbO	0.014	0.018	0.026	0.012	0.018	0.016	0.015	0.023	0.0149
SiO <sub>2</sub>	15.677	0.000	3.110	0.000	1.037	0.000	0.346	0.152	0
P <sub>2</sub> O <sub>5</sub>	0.011	0.000	0.008	0.004	0.005	0.003	0.004	0.000	0
Y <sub>2</sub> O <sub>3</sub>	0.013	0.000	0.021	0.013	0.014	0.006	0.011	0.007	0.0036
Dy <sub>2</sub> O <sub>3</sub>	0.004	0.000	0.019	0.014	0.021	0.030	0.022	0.007	0
Yb <sub>2</sub> O <sub>3</sub>	0.001	0.000	0.000	0.002	0.002	0.003	0.002	0.000	0
Total	96.620	95.595	57.199	99.996	86.136	101.212	95.781	95.067	102.89669
UO <sub>2</sub> +ThO <sub>2</sub>	0.0016	2.298	0.007	0.007	0.007	0.007	0.006	0.011	0.001

**Table 2-12 Weight Percent of Major Phases in Slag Samples and their Uranium, Thorium and REE (rare earth elements) abundance.**

Phase	Modal Abundance	Weight % Uranium and Thorium	Weight % REE
Glass	Site A: 3% Site B: 36 Site C: 2%	All: $\leq 0.6\%$	All: $\leq 10\%$
Gehlenite	Site A: 0-10% Site B: 39% Site C: 29%	Site A: 0 Site B: 0.065% Site C: 0	Site A: $\leq 1\%$ Site B: 3% Site C:
Calcium Aluminate (hibonite)	Site A: 30% Site B: 1% Site C:	Site A: 0.2% Site B: 0.137% Site C:	Site A: 4% Site B: 1% Site C:
Clinopyroxene	Site A: 0.0% Site B: 10% Site C:	Site A: 0.0% Site B: $\leq 1\%$ Site C:	Site A: 0.0% Site B: 1% Site C:
Ce-Silicate	Site A: ? Site B: 5-10% Site C:	Site A: ? Site B: $\leq 2\%$ Site C:	Site A: ? Site B: $\leq 18\%$ Site C:
Calzirtite - Zirconolite	Site A: Site B: 9.4% Site C: 4.0%	Site A: 2.2% Site B: 0.46% Site C:	Site A: Site B: Site C:
Perovskite - Pyrochlore	Site A: 11.6%* Site B: 9.5% Site C: 5.7	Site A: 11.5% Site B: 2.19% Site C:	Site A: ? Site B: Site C:
Thorianite - Th oxides	Site A: Site B: Site C:	Site A: 96.2% Site B: Site C:	Site A: Site B: Site C:
Spinel	Site A: 0.0% Site B: Site C: 22.6%	Site A: Site B: 0.31% Site C:	Site A: Site B: Site C:

\* For Site A calzirtite, perovskite, pyrochlore, and thorianite are combined.

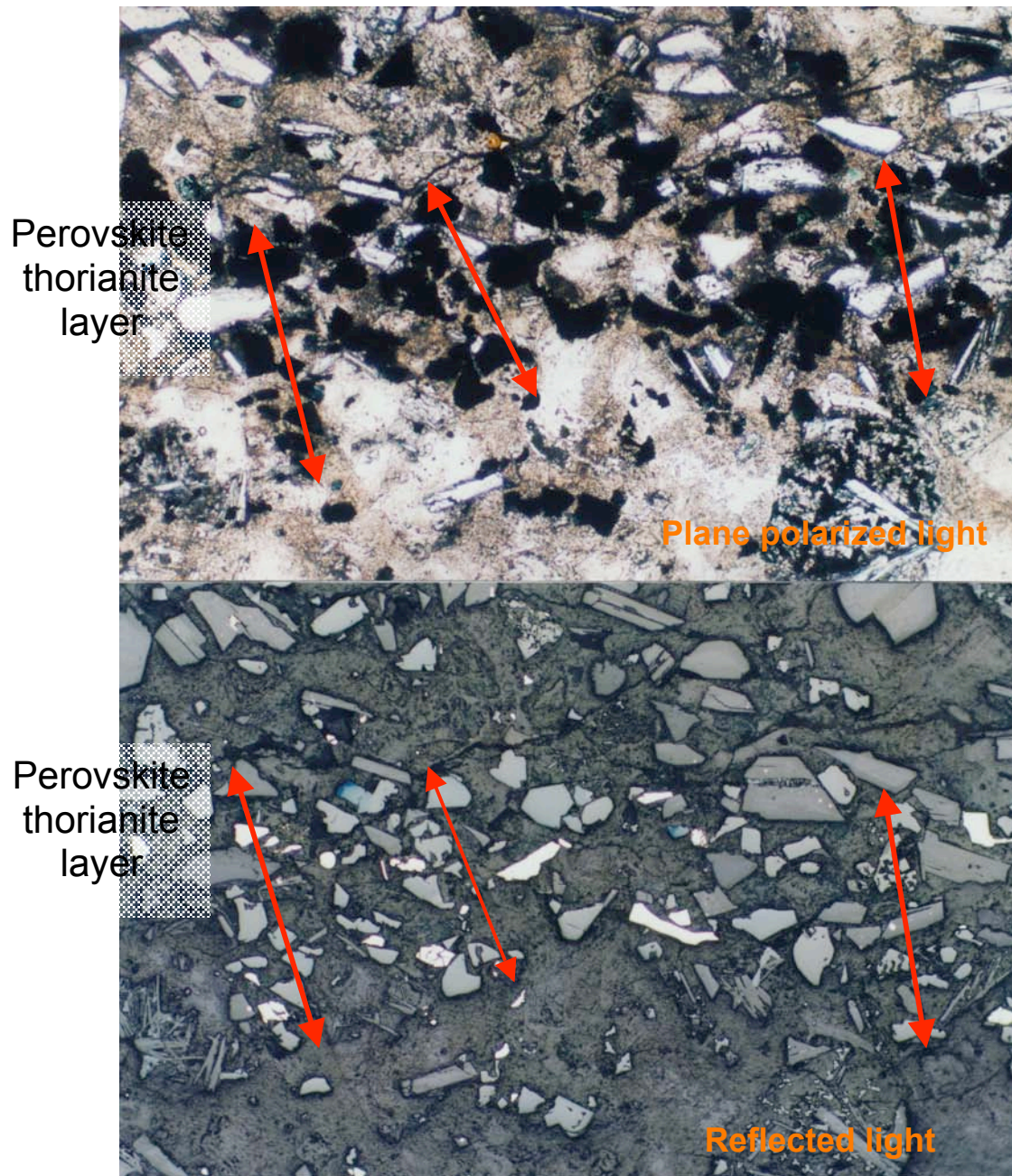


Figure 2-1. Photomicrographs of thin section of Site A slag sample A-2. Uranium and thorium are present in perovskite and thorianite. These photomicrographs show a layer enriched in perovskite and thorianite. See also Figure 1-2 for photograph of hand sample. Upper image shows the sample in plane polarized light. The perovskite and thorianite layer is black and it extends across the thin section from left to right toward the middle of the image. The same layer appears as small white grains in the lower image which was taken in reflected light.

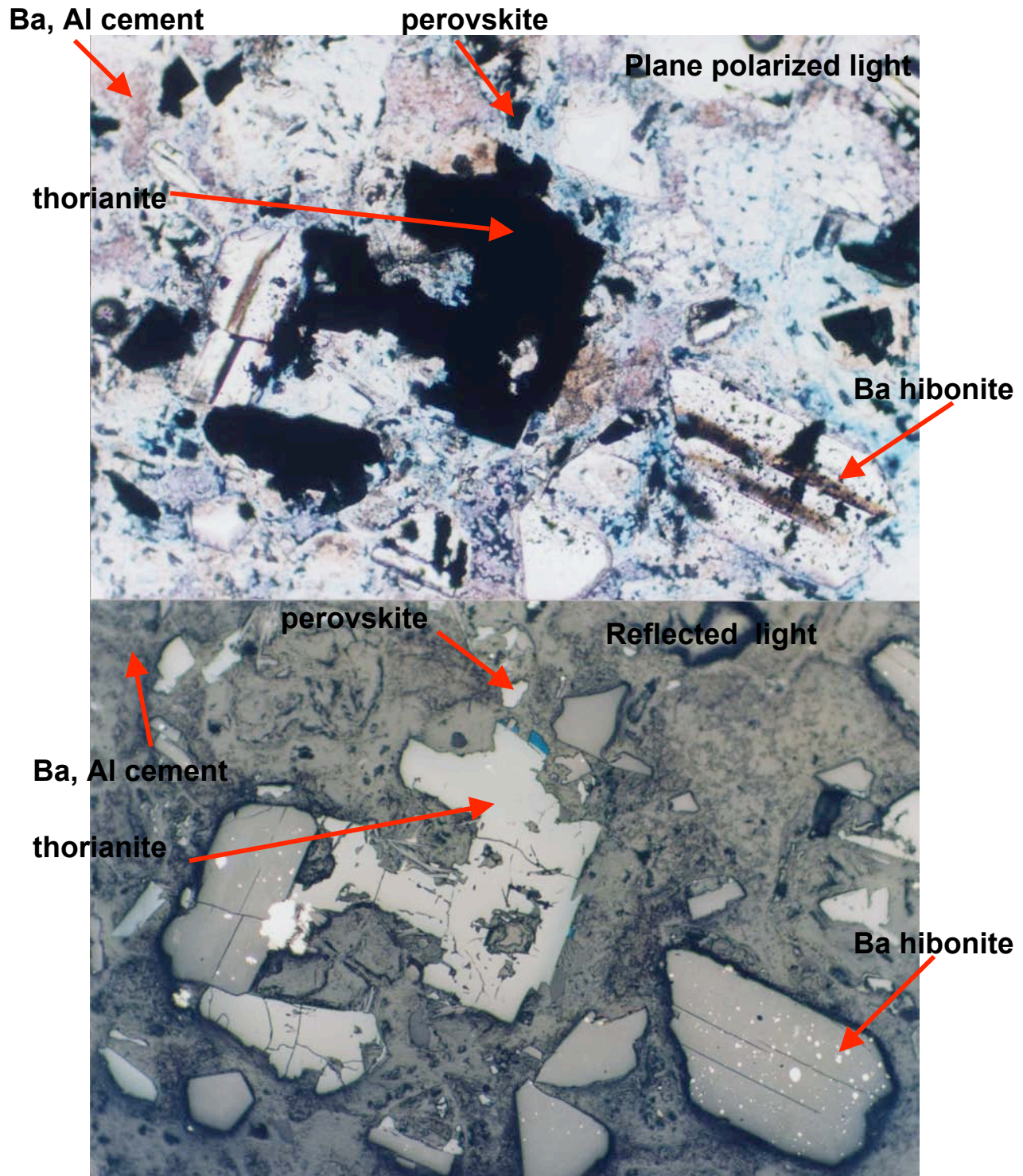


Figure 2-2. Photomicrographs of thin section of Site A slag sample A-2. See also Figure 1-2 for photograph of hand sample. Upper image shows the sample in plane polarized light. The fine grained cement, which is a complex Ba, Al compound, is medium gray. The uranium and thorium is found in perovskite which is the black opaque material under plane polarized light. The lower image is reflected light. The fine grained cement is more evident in this image. The medium gray colored grains with cleavage are Ba hibonite. Light gray grains are thorianite and perovskite.

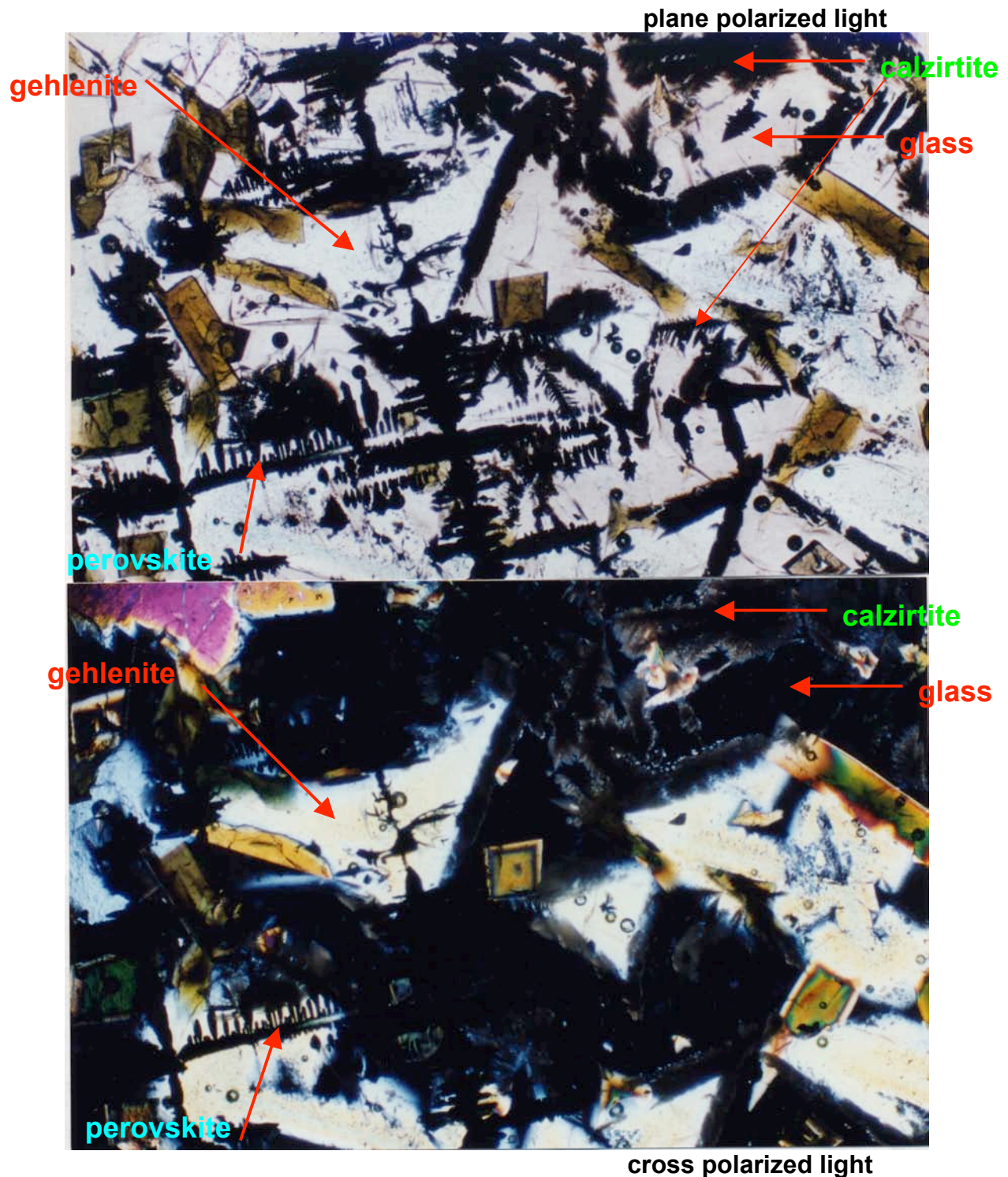


Figure 2-3. Photomicrographs of thin section from Site B slag sample B-8. The upper image is plane polarized light. The lower image is cross polarized light (crossed nicols). In the upper image, the brown euhedral crystals are clinopyroxene ( $\text{Ca, Al, Zr, Ti, Si}_2\text{O}_6$ ). The dark brown feathery dendritic crystals are calzirtite ( $\text{Ca}_2\text{Zr}_5\text{Ti}_2\text{O}_{16}$ ). It is difficult to distinguish between glass and gehlenite ( $\text{Ca}_2\text{Al}(\text{Al, Si})\text{O}_7$ ) under plane polarized light because both are white. However, under cross polarized light (lower image) gehlenite is pinkish yellowish and the glass is bluish black thus making it easy to differentiate between them.

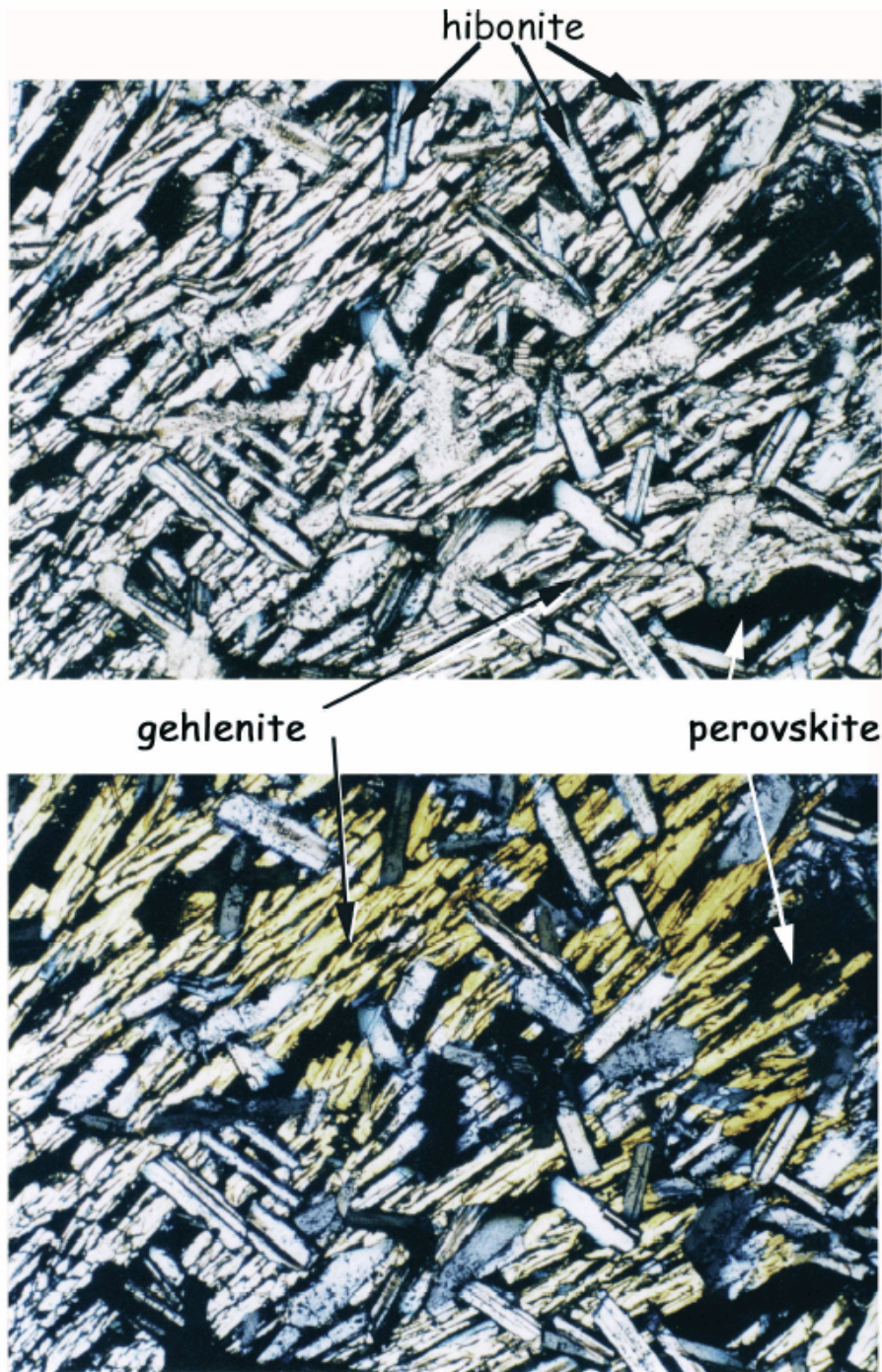
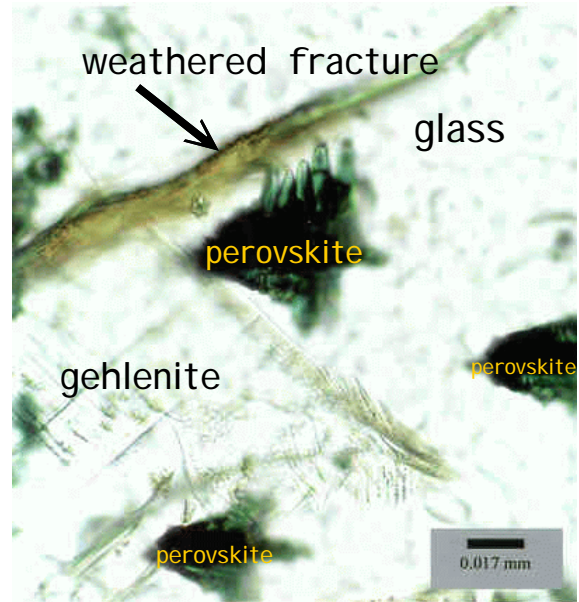
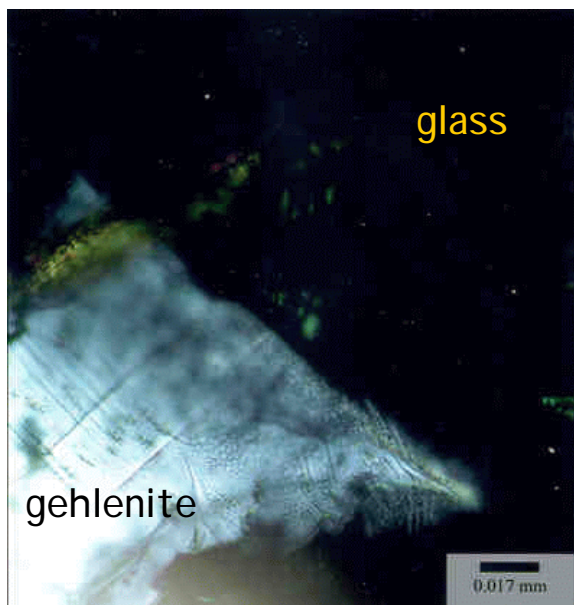


Figure 2-4. Photomicrographs of thin section from Site B slag sample 96TC-19. Upper image is plane polarized light, lower image is cross polarized light (crossed nicols). Uranium and thorium are found in perovskite and glass. When viewed in color under the polarizing microscope, hibonite  $[(Ca,Ce)(Ti,Al)_{12}O_{19}]$  appears as bluish white laths under both plane polarized and cross polarized light. Gehlenite also appears as light colored laths under plane polarizing light but it is golden under cross polarized light. The gehlenite is visible in the lower image as medium gray laths trending from the upper right toward the lower left part of the photomicrographs. The grayish white laths are hibonite and trend almost 90° to the gehlenite. In the lower image, the black phases are oxides, perovskite, calzite, and glass.



**Plane polarized light**



**Cross polarized light**

Figure 2-5. Photomicrographs of thin section from Site B slag sample B-8 showing glass, gehlenite  $\text{Ca}_2\text{Al}(\text{Al},\text{Si})\text{O}_7$ , and perovskite ( $\text{CaTiO}_3$ ). Uranium and thorium are found in the perovskite and glass. Under plane polarized light (upper image) the glass has a mottled texture and is white to colorless. However under cross polarized light (lower image) the glass appears black. Gehlenite is a white crystal with cleavage under plane polarized light (upper image) and is visible in the lower left corner. Under cross polarized light (lower image) the gehlenite is medium gray to white. Perovskite is green blue to black in plane polarized light and it is black in cross polarized light (lower image). Finally, note the weathered greenish brown fracture toward the top of the upper image.

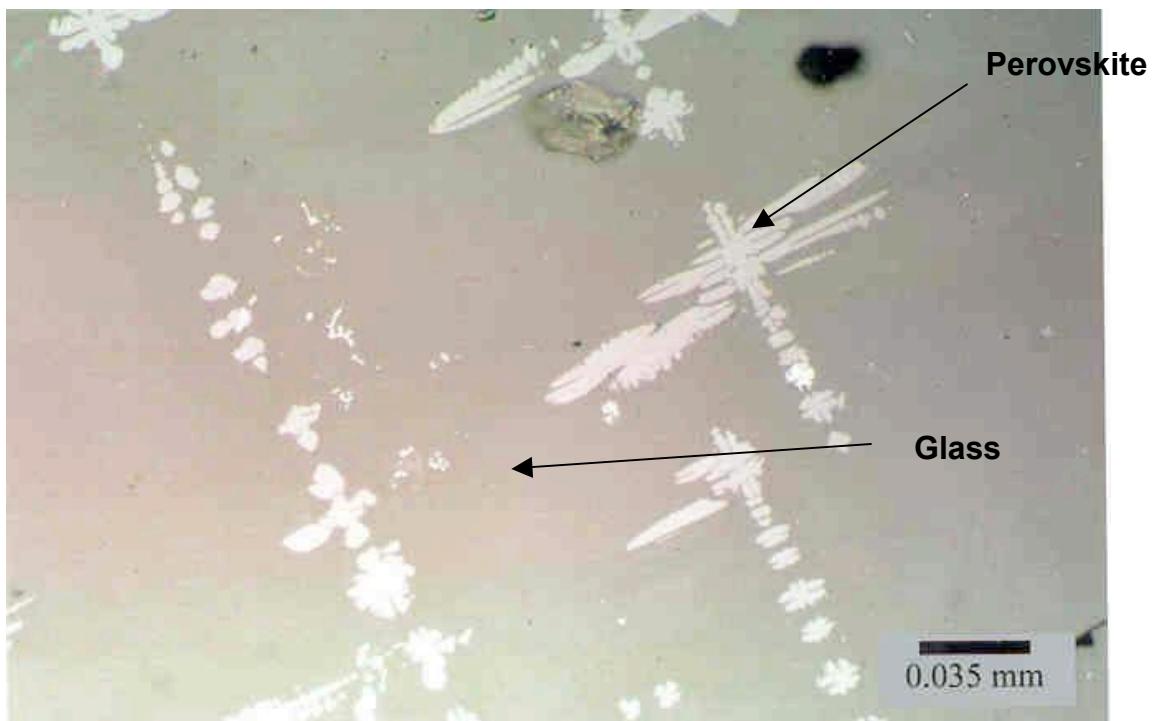


Figure 2-6. Photomicrographs of thin section from Site B slag sample B-8 showing perovskite ( $\text{CaTiO}_3$ ) dendrites. Uranium and thorium is found in the perovskite. Perovskite is medium gray to black in plane polarized light and although perovskite is black in cross polarized light (see Figure 2-5) it is white in reflected light (lower image).

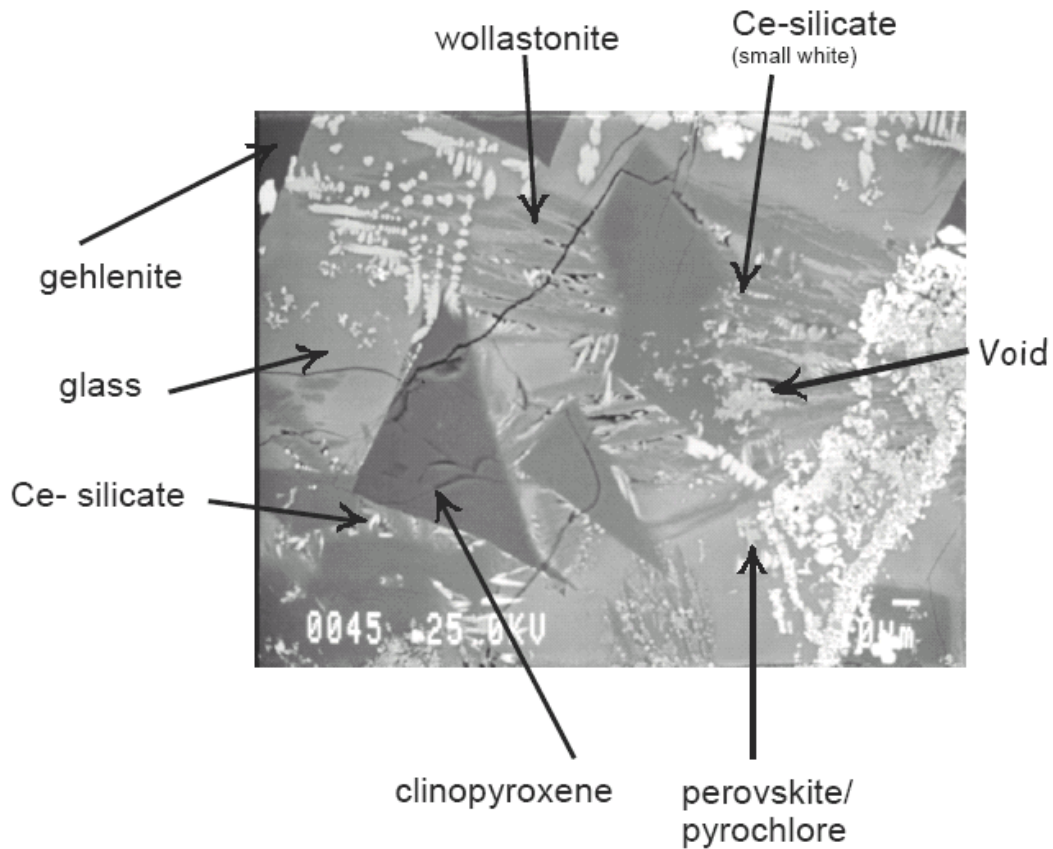


Figure 2-7. Back scattered electron (BSE) image of a Sn slag (B-5.5) from Site B showing evidence of devitrification and alteration of glass. This sample has weathered naturally. The glass devitrified to form wollastonite ( $\text{CaSiO}_3$ ) and the Ce and Th from the glass form Ce-silicate. There is some void space created due to decrease in volume during devitrification which would increase the porosity.

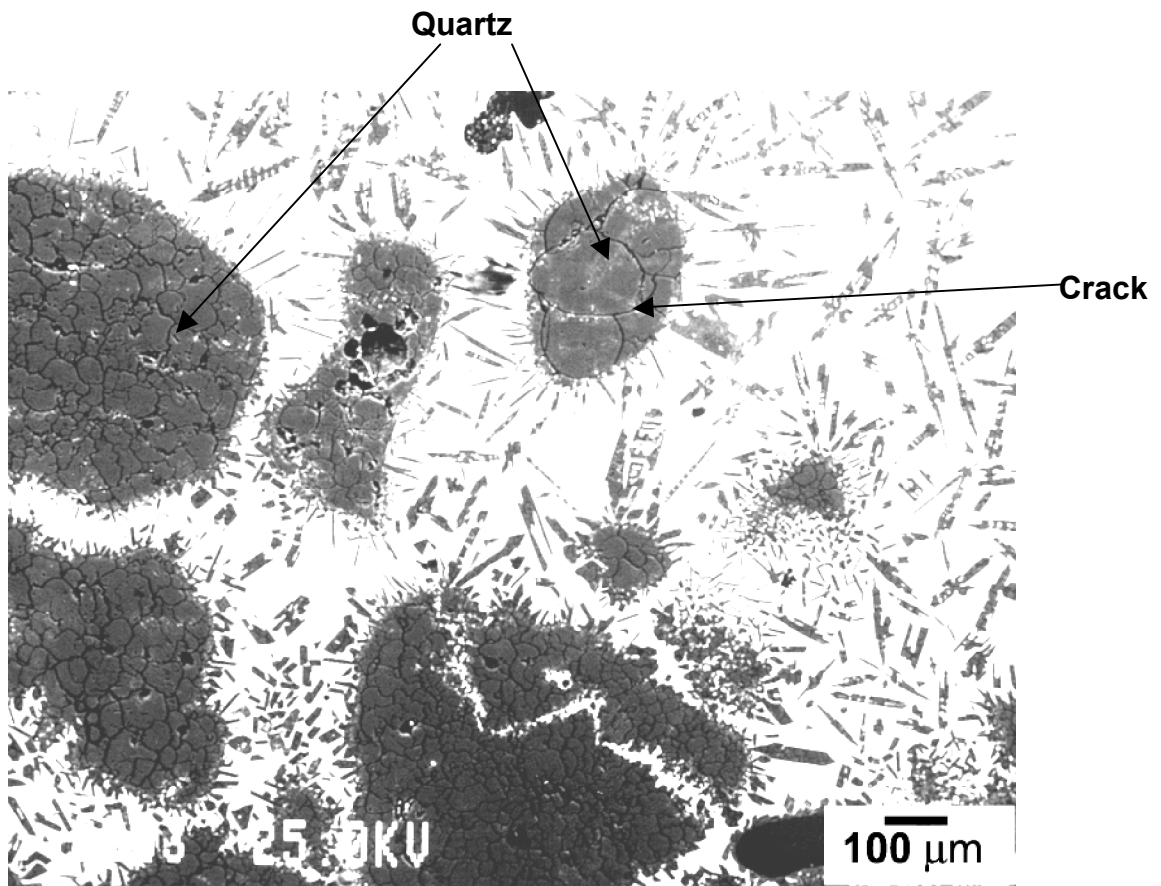


Figure 2-8. Back Scattered Electron (BSE) image of Site C slag sample C-1a. The large dark grains are quartz pseudomorphs after cristobalite. Cracks formed by the change in volume as the  $\text{SiO}_2$  transformed from cristobalite to quartz are quite noticeable particularly in the large grains at the top.

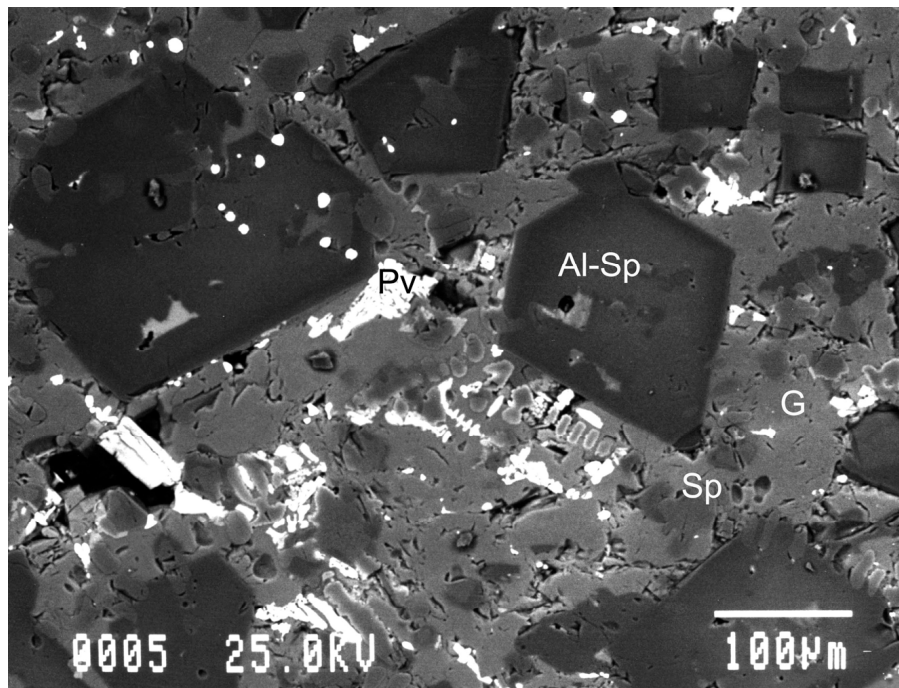
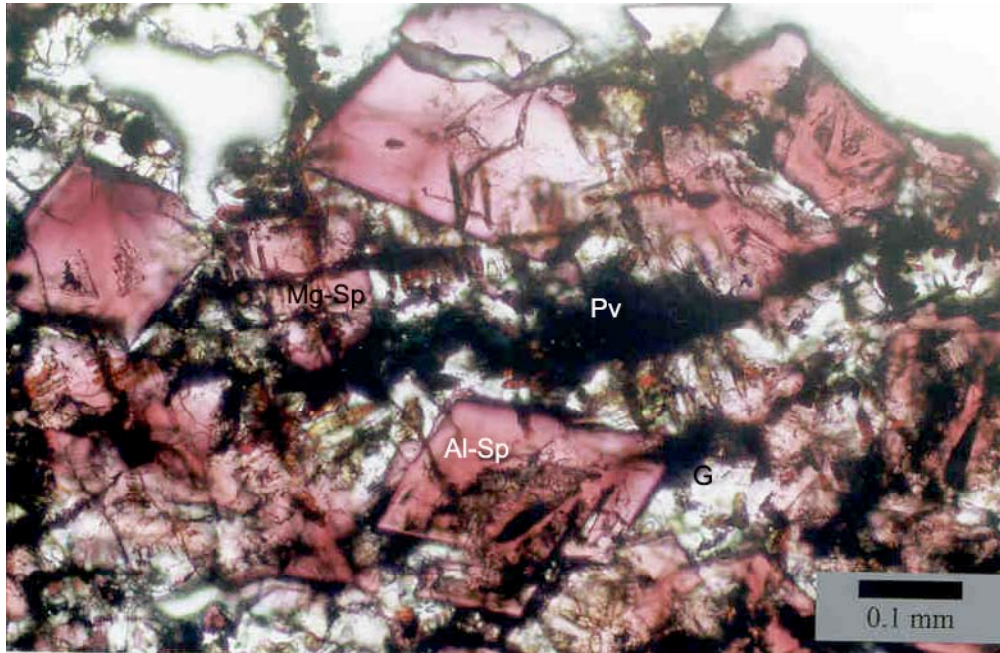
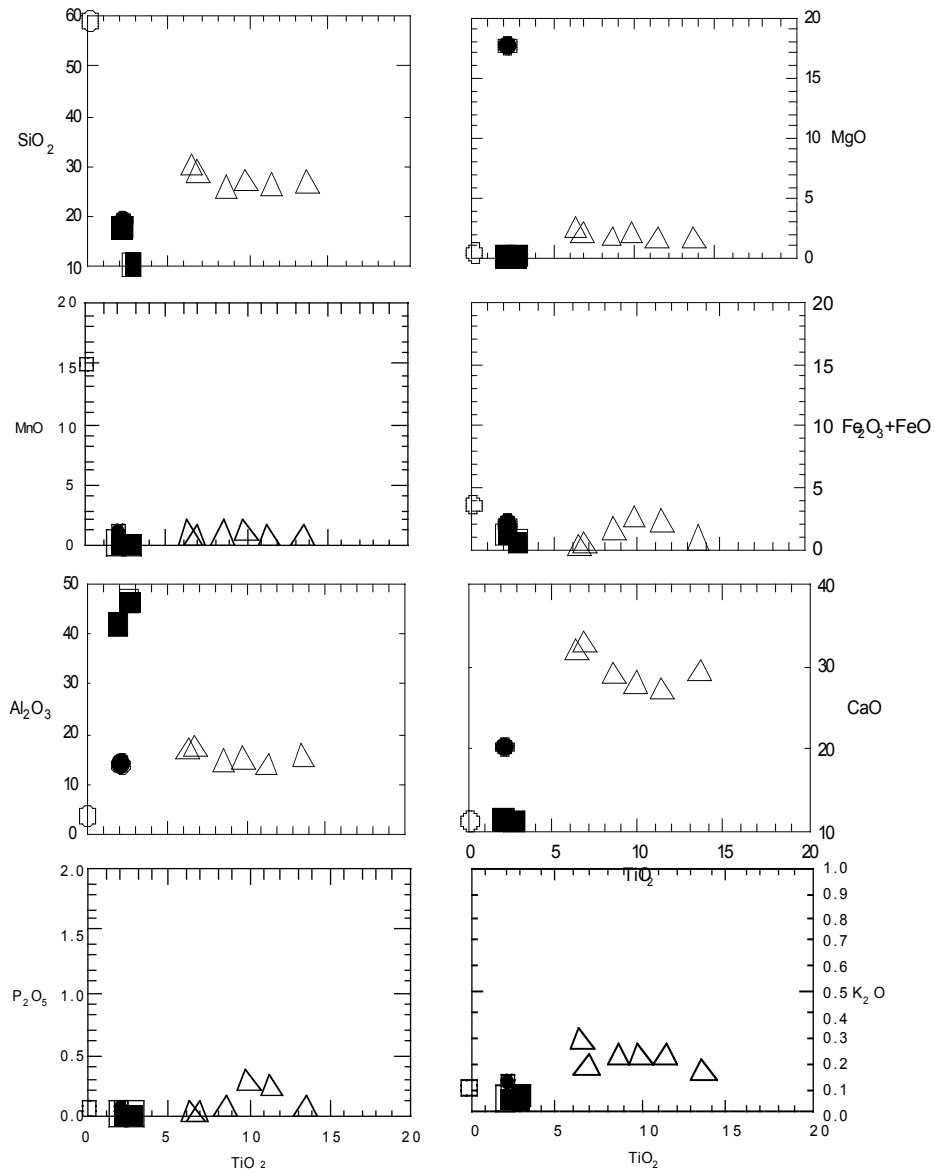


Figure 2-9. Photomicrographs of Site C slag sample C-S in plane polarized light and BSE. Upper image is plane polarized light and the bottom one is a Back Scattered Electron image (BSE) of a different part of the sample. In the plane polarized light image, the large rhombohedral crystals are Al, Cr, Mg spinel (Al-Sp), the dendrites are Mg,Fe spinel (Mg-sp), the black dendrites and interstitial phases are perovskite, and the white phase is glass. In the BSE image, the dark gray euhedral crystals are Al, Cr,Mg spinel (Al-sp), the medium gray dendrites are Mg,Fe spinel, the light gray is glass (G), and the white phase is perovskite (Pv).



Weight Percent

Weight Percent



Weight Percent TiO<sub>2</sub>

Figure 2-11. Compositional variation diagrams illustrating the variation of select elements when compared with TiO<sub>2</sub>. Site A slag - solid square, Site B glass - open circle, Site C slag - triangle, Site C slag - solid circle.

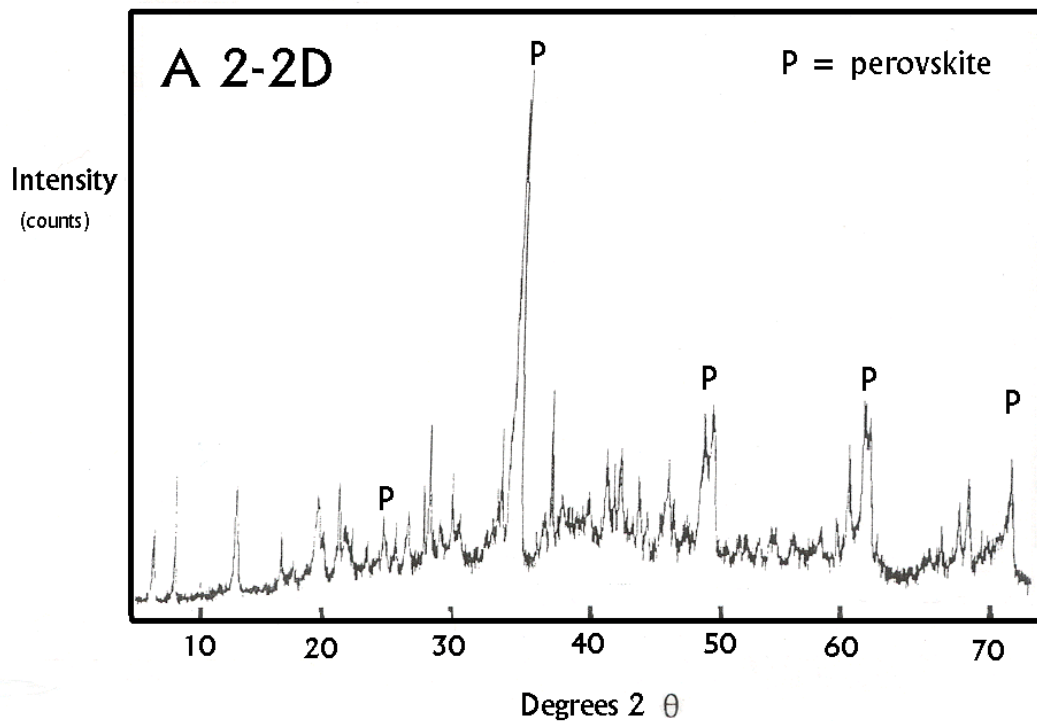
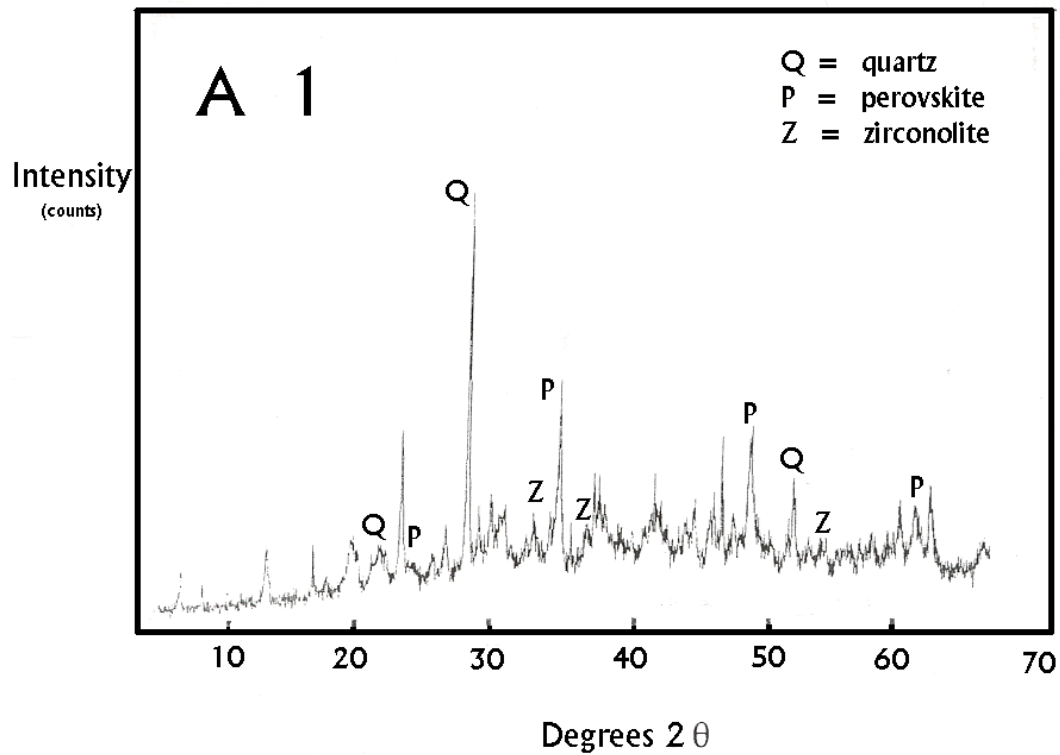


Figure 2-12. X-ray diffraction patterns of Site A slag. Note the complexity of the patterns due to the number of phases present. It is difficult to distinguish between many of the phases by this means. Consequently a suite of analytical techniques was required to identify the phases.

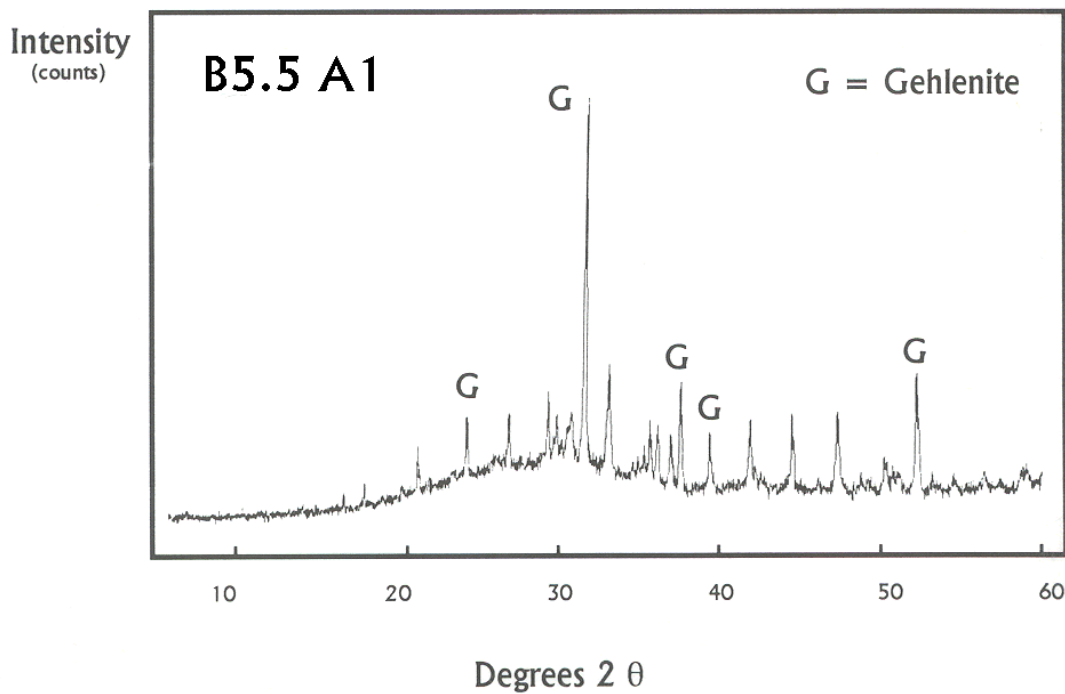
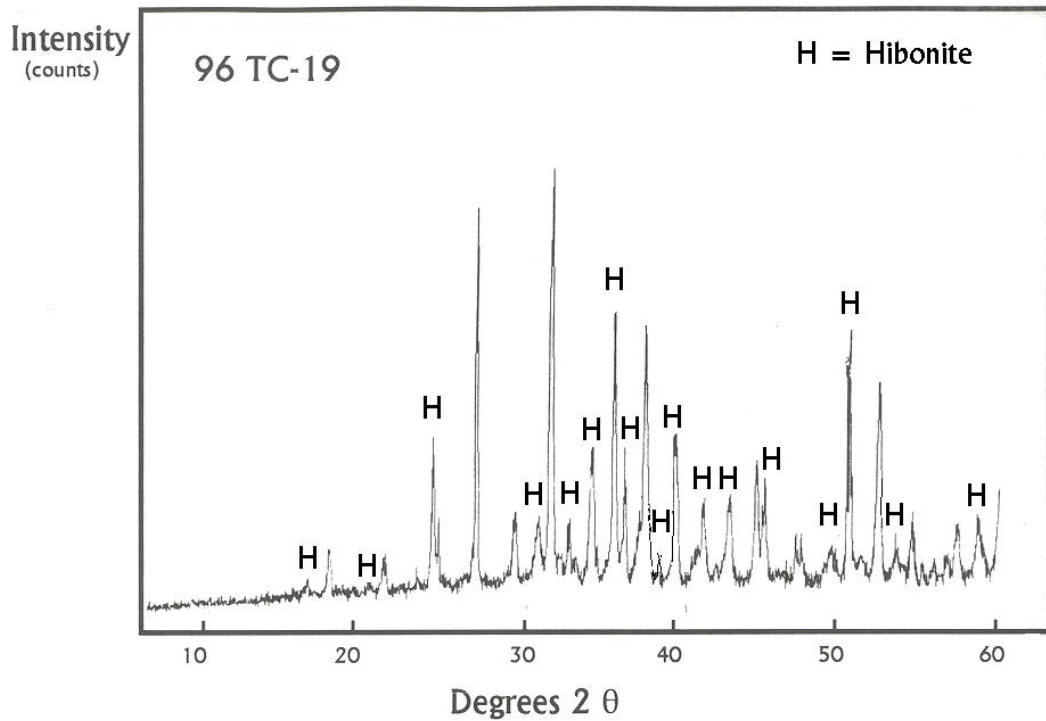


Figure 2-13. X-ray diffraction patterns of Site B slag. Note the compositional differences. The slag at the top is probably the result of Nb - Ta processing and the slag at the bottom is thought to be the parent tin slag prior to Nb - Ta extraction.

96T-A-4 Unleached

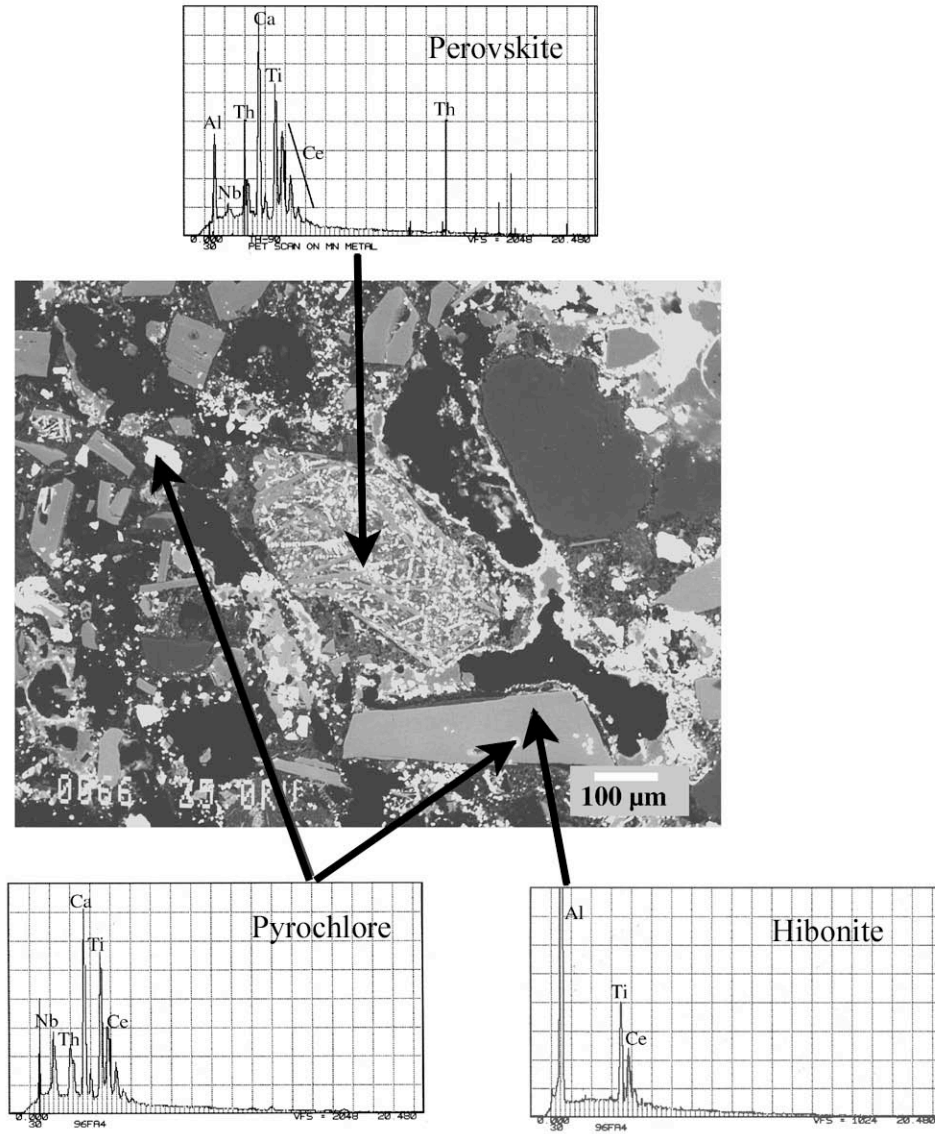


Figure 2-14. Back Scattered Electron (BSE) image and Energy Dispersive Spectra (EDS) patterns of Site A sample 96F-A-4. In the back scattered electron image, the bright phases have a higher mean atomic number. The large, central grain consists of glass and perovskite and it contains Al, Nb, Th, Ca, Ti, Ce, and Th (indicated by upper EDS spectra). The medium gray grain in the lower right of the BSE image is hibonite which contains Al, Ti, and Ce (lower EDS spectra) and it surrounds a bright sphere of pyrochlore which contains Nb, Th, Ca, Ti and Ce (lower left EDS spectra).

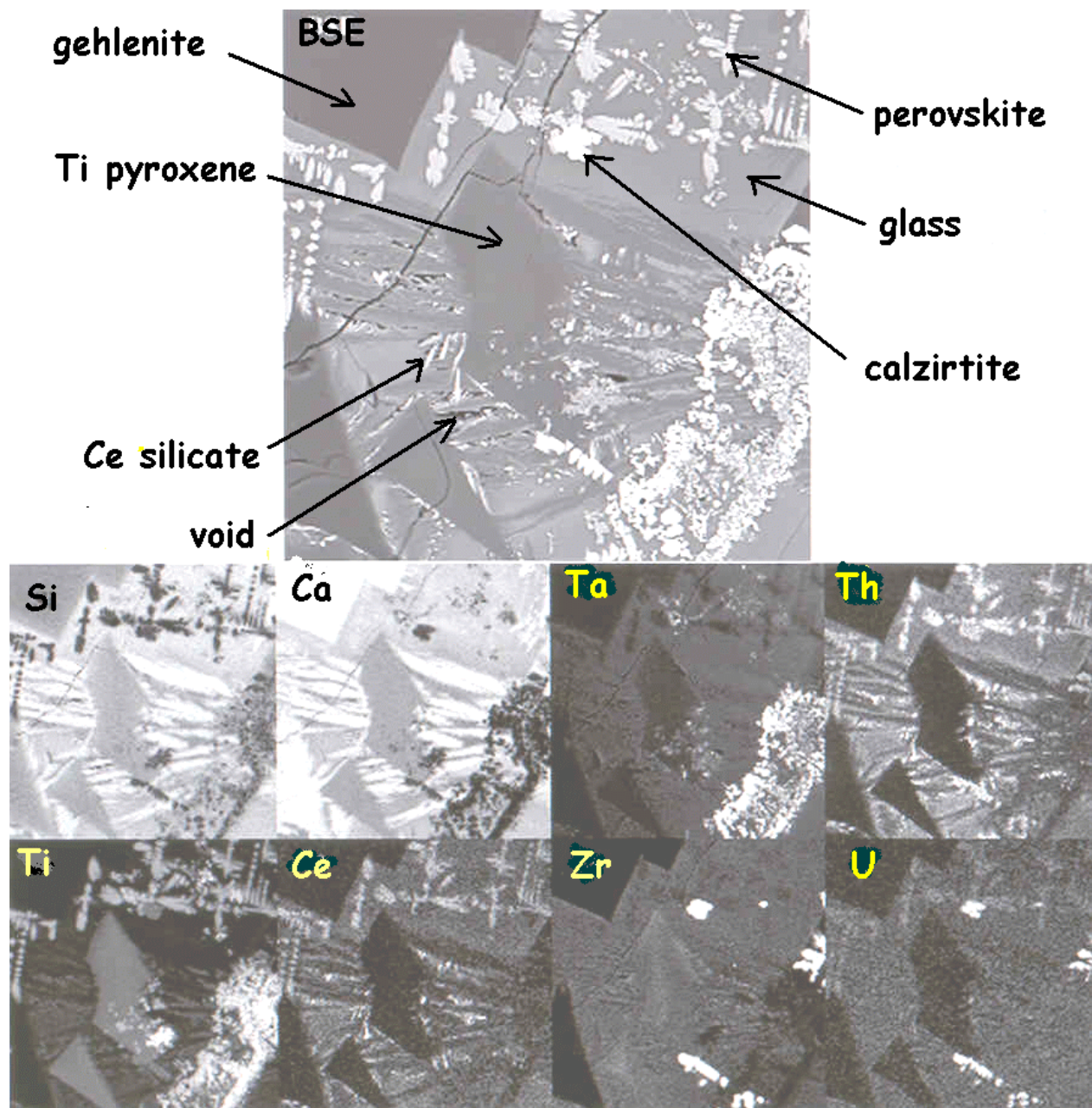


Figure 2-15. Back Scattered Electron (BSE) and x-ray map images of Site B slag sample B5.5. The upper one is a BSE image of slag in which the bright crystals are uranium/thorium bearing perovskite and calzirtite. The dark phases are gehlenite and Ti clinopyroxene, and the medium gray interstitial phase is glass. The eight smaller images are x-ray maps of elements: Si, Ca, Ta, Th, Ti, Ce, Zr, and U. Brightness of the phase indicates greater abundance of the element in the image. It can be seen from these images, that uranium is concentrated in the calzirtite and thorium is concentrated in the perovskite.

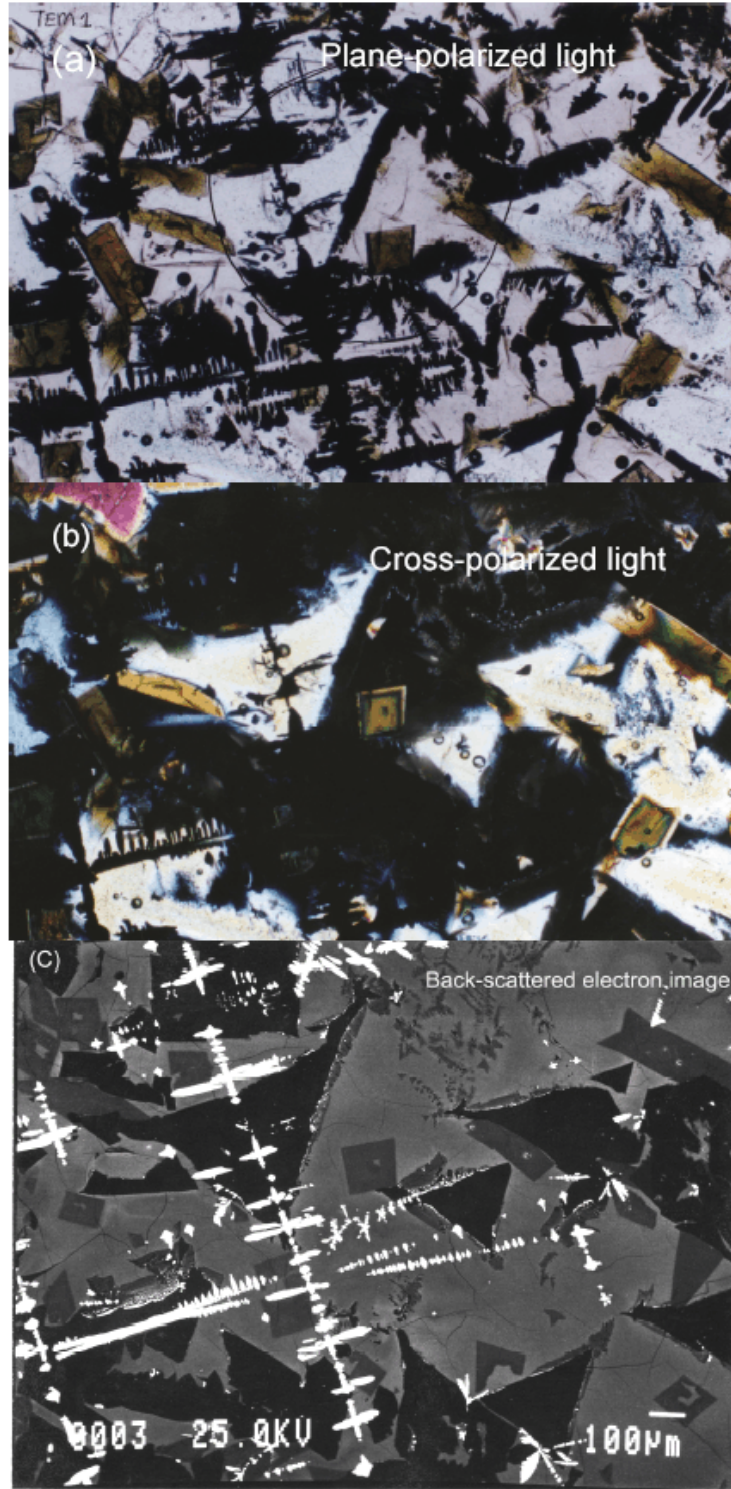


Figure 2-16. Site B tin slag Sample B-8. The top image (a) represents plane-polarized light. The central medium gray euhedral crystal is a Ti - Zr pyroxene. Under plane-polarized light, gehlenite and glass are both light gray and are difficult to distinguish. Perovskite is a black dendrite and calzirtite is present as small feathery dendrites. Image (b) is the same view as (a) under cross-polarized light, the gehlenite crystals appear white and are easily distinguished from the black glass. The pyroxenes are visible as medium gray, zoned crystals. (c) is a BSE image of the same view as above. Pyroxene is medium to dark gray, gehlenite is dark gray, the perovskite dendrites are white, and the small white stars are calzirtite. The circle in image (a) was drawn in ink on the thin section and it is the area selected for TEM study. See Figure 2-17 for a further explanation of the methodology.

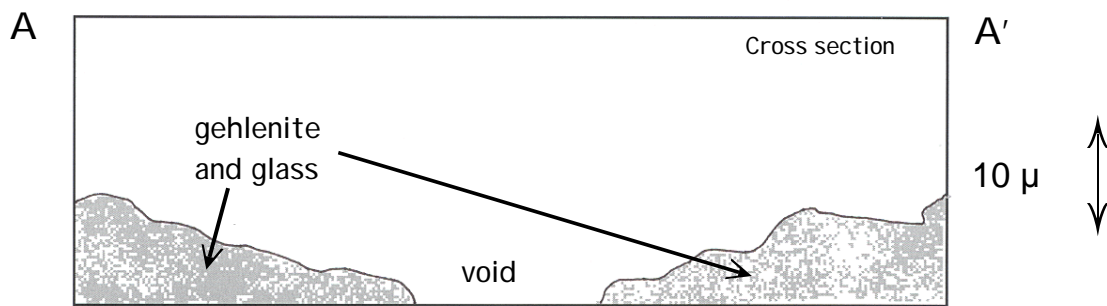
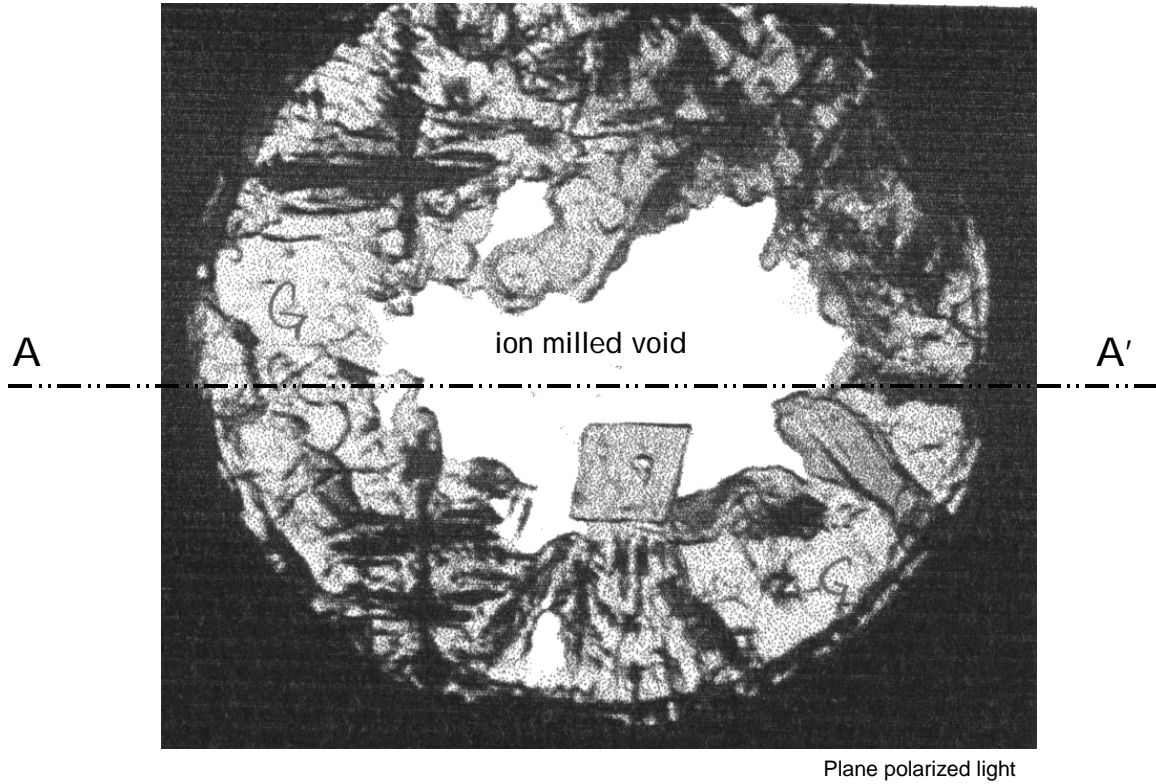


Figure 2-17. Upper image shows a TEM grid of Site B slag sample B 8 with an ion milled hole. The euhedral crystal in the lower center is the Ti- Zr pyroxene seen in Figure 2-16. The black dendrites are perovskite and the gray material around the edge of the view consists of gehlenite and glass. Ion milling was used to make a section thin enough to be used in the high resolution TEM (HRTEM). The HTEM patterns are seen in Figure 2-18. The lower image is a schematic cross-section of the ion milled sample.

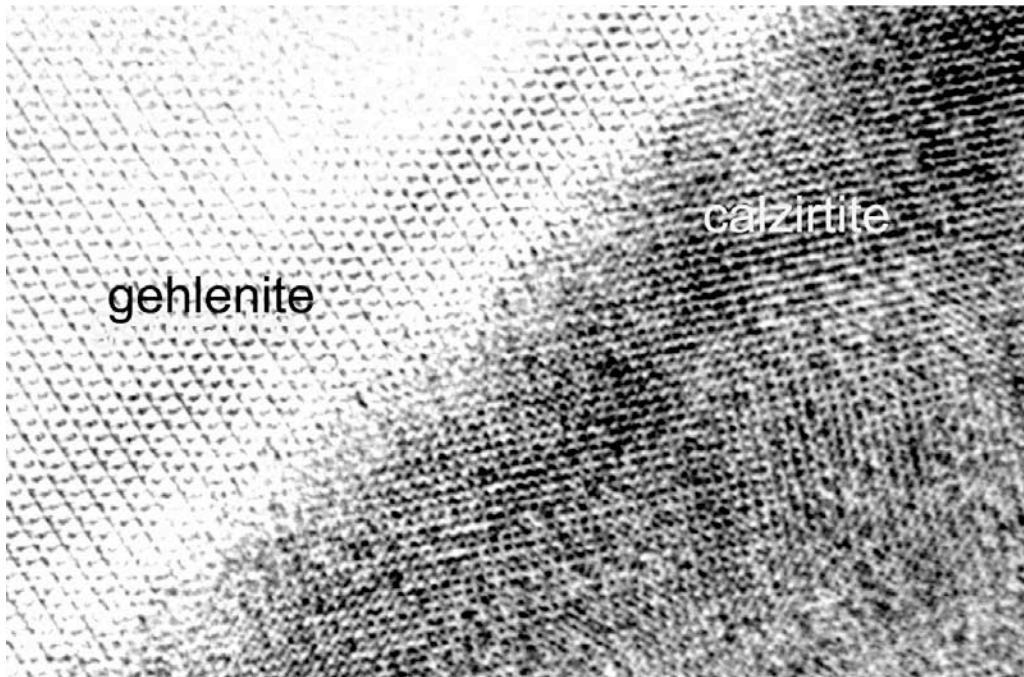
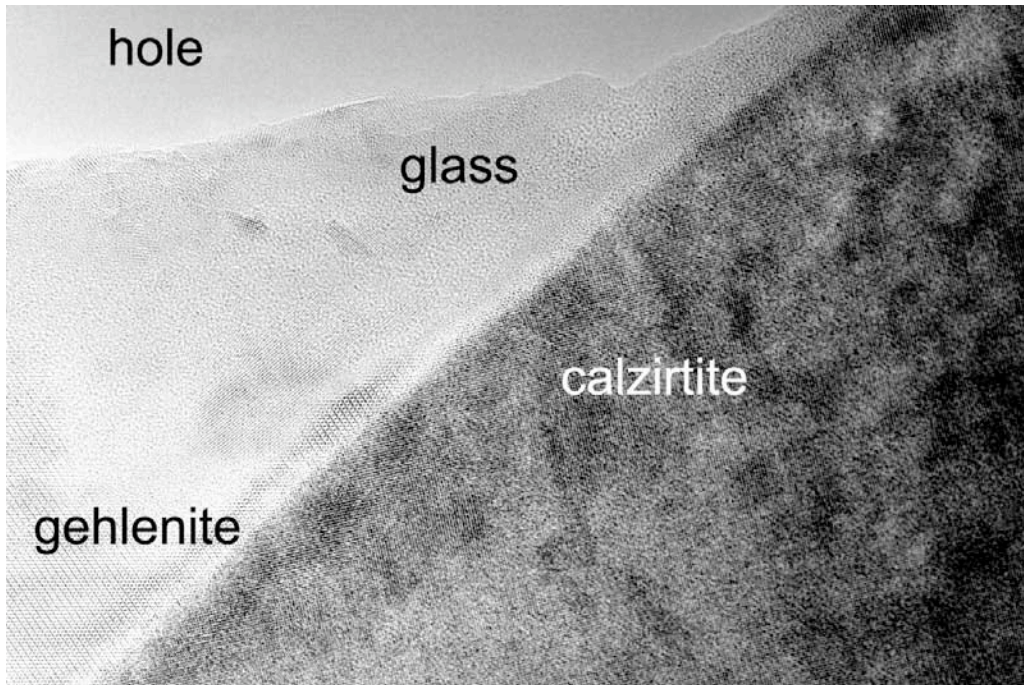


Figure 2-18. HRTEM image of Site B tin slag (sample B-8). The upper image shows the grain boundary between gehlenite and calzirtite. Note that the glass is devitrifying forming an unidentified crystalline material. The lower image is a magnification of the lower left corner of the upper image and it shows the contact of the gehlenite and calzirtite.

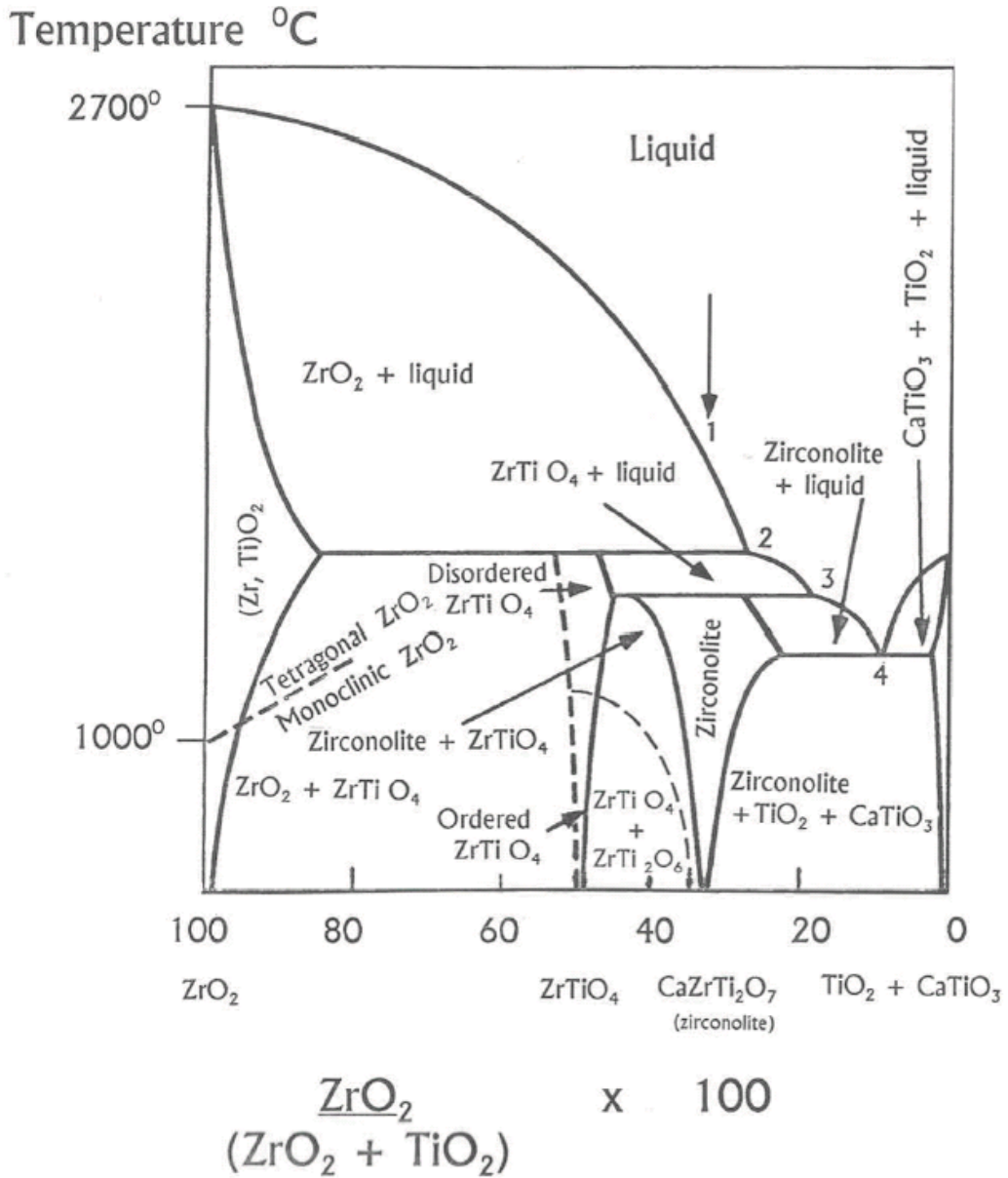


Figure 2-19. Phase diagram of the ZrO<sub>2</sub> - zirconolite - TiO<sub>2</sub> + CaTiO<sub>3</sub> system (after Xu and Wang (2000)).

### 3.0 Slag Weathering

#### 3.1 Introduction

Slag is a multiphase material, containing glass and crystalline phases. Corrosion of glasses and ceramics has been studied for many years by both industry and the nuclear waste community (Bates, et al., 1982, Byers, et al., 1985, Grambow, 1992, Vandiver, 1992), and this information is available to bound the leaching behavior of the glass found in the slags.

Degradation of a slag is controlled by the phases most susceptible to corrosive attack by the environment, which depends on the composition, concentration and the temperature of the attacking substances, and the glass or crystalline phases. For example, experimental weathering of a borosilicate glass indicates that the effect of boiling, concentrated hydrochloric acid on borosilicate glass is almost negligible. However borosilicate glass is severely corroded by interaction with dilute hydrofluoric acid at 25 degrees C (Parry, 1992). In contrast, phosphate glasses are resistant to HF, but are corroded by HCl (Parry, 1992).

Susceptibility to corrosion by water and acid solutions increases with the alkali content of the glass (Parry, 1992). Parry also showed that the higher the coulombic force between the divalent cations and a singly charged oxygen ion the lower the solubility. Jantzen (1992, p 20) discussed a thermodynamic approach to glass corrosion and noted that "...hydration thermodynamics has wide applicability to predict the durability of ... modern, and nuclear waste glass..." This approach may have utility with respect to the corrosion of the glass phase in the SDMP slags.

In addition to dissolution of the glass, devitrification may lead to increase in overall porosity of the slag, and provide access for fluids to the interior of a slag block, thus allowing potential corrosion and alteration of glass and radionuclide-bearing phases. Glass from the naturally weathered samples at the SDMP sites have been analyzed and results are discussed below.

#### 3.2 Estimating Radionuclide Release from Slags

Chemical composition and elemental variation in the SDMP slag glasses can be determined and provide the basis for useful alternatives to standardized leach tests. As was pointed out in Section 1.3 there can be up to four orders of magnitude of difference in the results among the ANSI/ANS 16.1, the EPA Method 1311 (TCLP) and EPA Method 1312 (SPLP) leach tests.

One can use the data discussed in Sections 2 and 3 of this report to calculate leach rates as mass fluxes

of radionuclides<sup>3</sup> from the slags analyzed to the fluids surrounding the slags. Depending on nature of the surrounding fluid, the radionuclide species released may be soluble in the fluid and may deposit on the surface of the slag. The volumetric concentrations of dissolved species and the mass fluxes of deposited species depend on species solubility in the flow regime of the surrounding fluid. The data taken in this report allow for the calculation of mass flux releases for individual radionuclides. Cruder estimates that lump radionuclides and their species together also are possible.

An alternative to using mass fluxes is to estimate the total amount of radionuclide species that could be available from the slag and use this quantity as a concentrated source in a transport calculation.

##### 3.2.1 Estimating Leach Rates as Mass Fluxes at the Slag Surface

Radionuclide species were observed as compounds, e.g.  $UO_2$ , in phases, e.g. perovskite, in slags. Mass-based concentrations of radionuclide species (mass of species/mass of phase) were measured as weight percents. Volume fractions of phases (volume of phase/volume of slag) were measured as modal abundances. For purposes of estimating releases of radionuclides from slags, one needs to know the concentration of radionuclide  $r$  occurring as species  $k$  in phase  $p$  in units of mass of radionuclide  $r$ /volume of slag. This concentration can be expressed in terms of the observable quantities and quantities available in handbooks as

$$C_{k,r,p}^s = \mu_p \rho_p C_{k,r,p}^m \quad (1)$$

where

$C_{k,r,p}^s$  = the volumetric concentration of species  $k$  containing radionuclide  $r$  in phase  $p$  in the slag in units of (mass of species  $k$  containing radionuclide  $r$ /volume of slag),

$\mu_p$  = the modal abundance (volume fraction) of phase  $p$  in the slag in units of (volume of phase  $p$ /volume of slag), measured in the laboratory;

$\rho_p$  = the density of phase  $p$  in the slag in units of (mass of phase  $p$ /volume of phase  $p$ ), available from handbooks of properties of materials; and

$C_{k,r,p}^m$  = the mass-based concentration of the  $k$ th species containing radionuclide  $r$  in phase  $p$  in units of (mass of constituent  $k$ /mass of phase  $p$ ), measured in the laboratory.

---

<sup>3</sup>The data could be used to calculate the release of non-radioactive contaminants as well.

If  $x=0$  represents the slag surface and the  $x$  coordinate is directed into the slag, the surface gradient of the volumetric concentration is

$$\left( \frac{\partial C_{k_r,p}^s}{\partial x} \right)_{x=0} = \mu_p \rho_p \left( \frac{\partial C_{k_r,p}^m}{\partial x} \right)_{x=0} \quad (2)$$

An analysis of the slag data collected for this report<sup>4</sup> has shown that the slags' phases dissolve and their surfaces recede at a dissolution rate  $v_p$  (length/time), which can be estimated from a knowledge of the history of the slag's shape or from the slag's age and the thickness of the rind around the slag. The volumetric concentration of the species  $k$  containing radionuclide  $r$  in phase  $p$  in the slag near a receding surface follows approximately the steady-state law

$$C_{k_r,p}^s(x) = (C_{k_r,p,0}^s - C_{k_r,p,\infty}^s) \exp\left(-\frac{v_p x}{D_{k_r,p}^s}\right) + C_{k_r,p,\infty}^s \quad (3)$$

where 0 and  $\infty$  denote surface and far-from-surface values of concentration, and  $D_{k_r,p}^s$  is the diffusion coefficient for component  $k$  containing radionuclide  $r$  in phase  $p$ , which one can estimate if  $v_p$  is known by fitting Equation (3) to measured concentration profiles. The surface mass flux of component  $k$  containing radionuclide  $r$  in phase  $p$  from the slag is

$$\begin{aligned} m_{k_r,p}'' &= D_{k_r,p}^s \left( \frac{\partial C_{k_r,p}^s}{\partial x} \right)_{x=0} \\ &= v_p (C_{k_r,p,\infty}^s - C_{k_r,p,0}^s). \end{aligned} \quad (4)$$

The mass flux of species  $k$  containing radionuclide  $r$  from the slag at its surface may be deposited on the slag surface, dissolved in the fluid adjacent to the slag and carried away, or both deposited on the slag surface and dissolved and carried away. The surface mass flux for radionuclide  $r$ , released by all species containing the radionuclide, is

$$m_{r,p}'' = M_r \sum_{k_r} \frac{m_{k_r,p}''}{M_{k_r}}, \quad (5)$$

where  $M$  denotes molecular weight. The amount of species  $k$  containing radionuclide  $r$  taken away from the slag by the adjacent fluid depends on the flow regime of the fluid and whether the radionuclide species being released is soluble in the fluid. Given the slags' outdoor locations on or below the ground surface, the most common adjacent fluids are expected to be air and water. Radionuclide species are not expected to be soluble in air, but they may be soluble in water.

If the concentration of species  $k$  containing radionuclide  $r$  in the adjacent fluid and far from the slag is zero, then conservation of mass at the slag-fluid interface can be expressed as

$$H_{k_r} C_{k_r}^F + \Delta_{k_r}'' = \sum_p m_{k_r,p}'' \quad (6)$$

where

$H_{k_r}$  = the surface mass-transfer coefficient for species  $k$  containing radionuclide  $r$  in the fluid adjacent to the slag in units of (length/time) and is described in more detail in this report's Appendix,

$C_{k_r}^F$  = the volumetric concentration of species  $k$  containing radionuclide  $r$  in the fluid adjacent to the slag in units of (mass of species  $k$  containing radionuclide  $r$ /volume of fluid), and

$\Delta_{k_r}''$  = surface deposition flux of species  $k$  containing radionuclide  $r$  in the fluid adjacent to the slag in units of (mass species  $k$  containing radionuclide  $r$ /area/time).

### 3.2.2 Release to the Surrounding Fluid and Deposition onto the Slag Surface

The right-hand side of Equation (6) gives the available mass flux of released species from the slag. The left-hand side gives the distribution of released species between fluid dissolution and deposition on the slag surface. Depending on whether the species released at the slag surface is soluble in the fluid adjacent to the slag, Equation (6) provides a means to calculate either the concentration of the species in the fluid adjacent to the slag or the surface deposition flux onto the slag.

If the fluid concentration,  $C_{k_r}^F$ , of the released species is less than the species's solubility,  $S_{k_r}$ , there is no surface deposition and Equation (6) gives

$$C_{k_r}^F = \sum_p m_{k_r,p}'' / H_{k_r}. \quad (7)$$

<sup>4</sup>"Mathematical and Geochemical Modeling of Radionuclide Leaching Rates from Radioactive Slags," Chen Zhu, University of Pittsburgh, Letter Report to the NRC, September 2002.

For dose calculations in performance assessments, one needs the concentration of radionuclide  $r$  in the fluid,

$$C_r^F = M_r \sum_{k_r} \frac{C_{k_r}^F}{M_{k_r}}. \quad (8)$$

If the calculated value of  $C_{k_r}^F$  in Equation (7) turns out to be greater than  $S_{k_r}$ , then one has to set

$C_{k_r}^F$  equal to  $S_{k_r}$  and use Equation (6) to estimate the surface deposition flux of the species:

$$\Delta_{k_r}'' = \sum_p m_{k_r,p}'' - H_{k_r} S_{k_r}. \quad (9)$$

The deposition flux of radionuclide  $r$  is

$$\Delta_r'' = M_r \sum_{k_r} \frac{\Delta_{k_r}''}{M_{k_r}}. \quad (10)$$

Equations (7) - (10) account for the possibility that for a particular radionuclide, there may be some dissolution and some deposition. This could be the case for release into water. For release into air,

$S_{k_r} = 0$  for all radionuclides, and only deposition occurs at a rate given by

$$\Delta_{k_r}'' = \sum_p m_{k_r,p}'' \quad (11)$$

During field surveys for slag samples,  $\alpha$  radiation was observed on slag surfaces. Given that  $\alpha$  radiation is easy to block and that U and Th are  $\alpha$  emitters, these observations suggest that surface deposition of U or Th may have taken place on the slags.

### 3.2.3 Calculation of Bulk Leach Rates

One can estimate a bulk mass-flux leach rate of all radionuclides in phase  $p$  or a slag by combining all of the radionuclides into a composite radionuclide,  $R$ . The slag-surface mass flux for the composite radionuclide is estimated using the equation

$$m_{p,R}'' = v_p \mu_p \rho_p C_{k_R,p}^m \frac{\sum_r M_r}{\sum_r M_{k_r}} \quad (12)$$

The summations in Equation (12) define the composite radionuclide  $R$ . Section 3.3.4 gives an example of the use of this equation.

### 3.2.4 Estimation of Mass Available for Transport

An alternative to estimating mass fluxes directly from the slag as boundary conditions for transport equations is to specify an amount of mass of radionuclide available for transport. This mass could be treated in the appropriate transport equation as a concentrated initial condition represented by a Dirac delta function or an approximation to it. If all of a constituent  $k_r$  containing radionuclide  $r$  in phase  $p$  in a slag is assumed to be available directly for transport, it could be represented as a mass source in the transport equations as

$$C_{k_r,p}^s(\vec{r}, 0) = \mu_p \rho_p C_{k_r,p}^m V_s \delta(\vec{r}) \quad (13)$$

where  $V_s$  is the volume of the slag and  $\delta$  is the Dirac delta function or a product of Dirac delta functions. The table below describes how  $V_s$  and  $\delta$  depend on the dimensionality of the transport analysis in Cartesian  $(x, y, z)$  coordinates.

Dim-ensions	$V_s$	$\delta(\vec{r})$
1	Slab thickness	$\delta(x)$
2	Slab cross-section	$\delta(x)\delta(y)$
3	Slab volume	$\delta(x)\delta(y)\delta(z)$

If a finite-difference method is used to solve the transport equations,  $\delta(x)$ ,  $\delta(y)$ , and  $\delta(z)$  would be  $1/\Delta x$ ,  $1/\Delta y$ , and  $1/\Delta z$ , where  $\Delta x$ ,  $\Delta y$ , and  $\Delta z$  are the dimensions of the cell where the initial contaminant mass is concentrated.

### 3.3 Naturally Weathered Samples

Many of the slags collected have light tan to medium reddish-brown weathered surfaces (Figure 3-1). This surficial alteration is believed to be caused by natural weathering processes. The alteration is not unexpected since the slags were formed under strongly reducing conditions. When the slag located at or close to the ground surface is exposed to oxidizing conditions, alteration may take place because the slag is no longer in an environment in which it is chemically stable. The alteration must be considered in long-term estimates of the slag's leaching behavior and the potential for release of radionuclides. To determine the physical and chemical changes taking place in the slag with time an investigation into the slag's weathering was done on a few of the samples to determine what physical

and chemical changes were occurring.

The slag's weathering was rapid and it took place some time between the slag's formation which began in the 1950s and continued through the mid 1970s at Site B and the 1990s at Sites A and C (i.e. ~ 40 years or less). Although this is not a long time by regulatory standards for radioactive waste disposal, weathering has taken place and it must be considered in long-term estimates of the slag's leaching behavior and the potential for release of radionuclides.

In hand specimens the weathering manifests itself as a surface rind of a few mm to > 1 cm thick. However, the weathering extends further into the samples than is apparent to the unaided eye. Optical and electron microscopy was particularly useful for clarifying the extent of alteration and for determining the mineralogic changes associated with alteration (i.e. what disappears and what secondary minerals form due to alteration). Microscopy revealed that the alteration extended well into the fabric of the slag particularly along fractures and grain boundaries (e.g. see Figure 3-2).

Sample porosity may play a role in the extent of weathering and a preliminary analysis was done. Given that the slags have all been sitting for about the same amount of time (20 to 40 years) there are slight differences in the thickness of the weathering rind. They are often >1.0 cm thick on the Site A slags, and ~0.2 cm thick on the Site B and Site C slags (Figure 3-1). The difference in the thickness of rind appears to be a function of sample porosity.

### 3.3.1 Natural Weathering Features at Site A

Samples from Site A often feature a ~1.0 cm yellowish-brown rind (Figure 3-1). The mineralogy of this rind is complicated and has not been fully determined. It is apparent though that the rinds are enriched in barium sulfates (barite), iron oxides and hydroxides. SEM studies have also identified secondary clays on the surfaces of the slag. Clays are a common secondary mineral formed after the alteration of silicate minerals. Detailed studies of chemical variation around cracks and grain boundaries have not been carried out. The clastic nature and high porosity of the Site A slags makes this a difficult task. The task is complicated further because it is likely that all of the clasts have been altered to some degree due to the manner in which the original slag was crushed, chemically processed, and then allowed to settle in evaporation ponds where natural cementation of the processed material took place. Because of this processing, it is difficult to determine what is a primary mineral assemblage of the slag as opposed to chemical alteration caused by the Site operator's processing of the slag, or by weathering processes which may have altered minerals and resulted in leaching of phases.

### 3.3.2 Natural Weathering Features at Site B

Alteration rinds on Site B slag are typically ~0.2 cm thick and they are composed of secondary iron oxides and hydroxides. Microscopy of the slag shows that the alteration is actually more pervasive than what is visible with the unaided eye and the alteration actually penetrates tens of centimeters into the slag. The alteration concentrates along grain boundaries and fractures in the slag. This is confirmed by EMPA elemental analyses which show a depletion in several elements along fractures. It is not clear, at this time, whether the depletion is due to primary crystallization or to leaching from along fractures. One could determine the cause of the depletion with additional studies of the interfaces with the TEM.

SEM images of weathered surfaces of Site B slag reveal: (1) dissolution of the glass, (2) leaching of glass and crystalline phases, (3) devitrification of the glass, (4) precipitation of secondary phases, and (5) possible microbial activity. Some examples of these processes are shown in Figures 3-3, 3-4, and 3-5. Figure 3-3 shows a weathered edge of Site B sample B-5.5. Perovskite, calzirtite and gehlenite are observed (BSE image 0004, Figure 3-3a) protruding from the glass along the weathered edge of some Site B slag, indicating that the glass has been dissolved from around the more resistant crystalline phases. Glass is also devitrified near the edge of some samples. SEM image 0006, sample B-5.5 (Figure 3-3b) of a weathered surface shows small, round precipitates that are high in Fe content, on the surface of a calc-silicate. This is possibly the result of microbial activity.

A sample of Sn slag (B-5.5) from Site B provided leaching information over a longer period than represented by the site's Nb-Ta slag (e.g. samples B-5.5, B-8, B-11). Sn slag was imported from Malaysia in the mid-1960's and it was the parent material from which Nb-Ta was extracted. However, it has not been produced in Malaysia for the last 50 – 100 years. Therefore the Sn slag found at Site B is at least 50 years older than the site's Nb-Ta slag. Devitrification of the glass in the Sn slag is evident in BSE images of B-5.5 (Figure 2-7). The feathery features radiating from gehlenite and clinopyroxene grains are wollastonite ( $\text{CaSiO}_3$ ) and Ce-silicates. Also evident is the decrease in volume of the devitrified materials relative to the original glass. Voids and fractures have been introduced into the slag from devitrification. A fracture filled with Ca-silicate and Fe-oxides is also observed in the Sn-slag, indicating the leaching of Ca and transport of Ca and Fe through the slag. The calzirtite and zirconolite in the slag appears to be altered. This could be investigated further with TEM which might bring to light variations in the Th and U content of calzirtite and structural degradation in the crystals and along grain boundaries.

The uranium and thorium are not present as uranium or thorium oxides, but as elements in (minor or trace

amounts) in silicate or oxide minerals and glass. Table 2-12 shows the relative amounts of U and Th in the minerals as well as the modal abundance of the minerals in the slag. These quantities can be used in Equations (1) and (4) to estimate boundary conditions or in Equation (13) to estimate a concentrated initial condition for solving transport equations.

Analysis of a Site B glass provides an estimate of the surface-concentration gradient that can be used to estimate the long-term leach rate in Equation (4). Figure 3-6 is a graph of microprobe data for the variation of REE with distance from a fracture in a glass. REE were used as a surrogate for U and Th because their low concentration made it difficult to detect them. In Figure 3-6, the concentration of REE increases with distance from a fracture indicating that leaching has been removing REE from the region near the fracture, which also is shown schematically in Figure 3-7. The linear-logarithmic regressions of the data points in Figure 3-8 provides a way to calculate surface concentration gradients that can be used in Equation (4) to estimate of the 25-30 year leaching rates.

It is apparent from EMPA data and BSE images that the chemical composition of the weathered glass in Site B samples B-5.5 (Sn slag) and 96TC19 (Nb-Ta slag) varies with distance from fractures and grain boundaries (Figure 3-9 and Figure 3-10). Leaching of specific elements from the glass may have occurred in these areas. Microprobe analyses along a traverse crossing the fractures indicate a change in glass chemistry. Glass near the fractures tends to be depleted in Th and U relative to glass several hundred microns from the fractures (see Figure 3-10). There is some scatter in the data and the plot is not smooth, however, there are several variables that have not been addressed by these analyses. It is not certain whether the glass initially had these chemical variations (i.e. whether the variations are due to initial crystallization). Another possible explanation for the scatter in the data is the inability to determine the distance of a point analyzed from a surface or fracture in the third dimension. These uncertainties could be addressed in the future with additional analyses.

Glass, clinopyroxene, and perovskite from four samples from Site B's Nb-Ta slag (sample B-5.5) were analyzed in detail by EMPA for chemical variation as a function of distance from the weathered surface. Samples B-5.5a, B-5.5b, B-5.5c, and B-5.5d were cut from one sample, B-5.5a taken from the top weathered surface, with B-5.5d taken from the lower, presumed unweathered surface (Figure 3-7). The data for glass are plotted in Figure 3-8. The outer 10 mm of the sample show a depletion of Si, Ca, Ce, Mn, Zr, Th and U with respect to the interior of the sample. Al, Ti, and Mg all increase in the outer 10 mm of the sample.

Glass analyses from B-5.5a and B-5.5b have been plotted as compositional variation diagrams Figure 3-

9, comparing the variation of key elements with SiO<sub>2</sub>. Data from sample B-5.5d (unweathered), all indicate a degree of correlation for Al, Ti, Zr, U with SiO<sub>2</sub>. However, the data for B-5.5a (weathered) indicate U, Zr, and Ca are not as well correlated with SiO<sub>2</sub>. This may be indicative of leaching of U and Ca from the glass in the weathered sample.

The electron microprobe was used to determine elemental variation in calzirtite as a function of distance from a weathered edge in samples from Site B and the results are shown in Figure 3-10. In the weathered slag (B5.5a) the weight percent of Ca and Si declines towards the weathered edge whereas the weight percent of Zr, Ti, Ce, Th, and U increases. In two samples of unweathered slag (B5.5c) data were collected throughout the thin sections and there is little variation in values of the aforementioned elements. It is interesting to note that the weathered samples contain higher values of both Th and U compared to the unweathered samples.

### 3.3.3 Natural Weathering Features at Site C

Alteration rinds were common in the Site C slag. This is not unexpected as the Site C samples had been collected at the ground surface where they were exposed to weathering processes.

#### (1) Glassy Slags

Slags in this group (e.g. sample C-2a) are highly vitreous and often vesicular. Weathered slags of this category are devitrified, transformed from a high temperature glass phase to a low temperature crystalline phase involves a volume decrease and the effects of this are seen by the prevalent cracks in the dendrites and the large SiO<sub>2</sub> patches (Figure 2-11). A weathered rind is often seen, consisting of iron oxides and clay-like materials.

#### (2) Dense Blocky Slags

These slags are distinctly different from those in the first group since they are more dense and blocky, and also seem to have fewer vesicles. Slags in this category are physically similar to basalts and to the black, finely crystalline slag from Site B (e.g. samples B-5 and B-5.5). The exterior surfaces of these slags are readily weathered to a greenish-gray fine-grained, clay-like material with deep fractured surface. These fractures appear to be hydration cracks. The fresh surface of hand sample (C-4) is dark reddish-brown in color. Minerals found in this group include hibonite, barium aluminate, periclase, monticellite, Cr spinel, perovskite, zirconolite, metallic iron prills, wollastonite, wustite and an alteration product, ardelite Ca<sub>2</sub>(SO<sub>4</sub>)<sub>2</sub>(HPO<sub>4</sub>)<sub>4</sub>·4H<sub>2</sub>O.

#### (3) Green-Blue Slags

Slag in this group (e.g. C-6) is distinctly greenish-blue in color and often has a 1 mm thick white crust around the outside of the sample. The exterior

surfaces of these slags are deeply indurated from hydration cracking. These surfaces contain clay-like materials. Freshly cut surfaces of this group's slag reveal a greenish-blue interior and small circular brassy looking metallic prills are often visible to the naked eye. Mineralogically, this group contains spinel, periclase, monticellite, forsterite, perovskite, zirconolite, a Ti-silicate, a Ni-oxide and metallic chromium

Samples in Site C's blue-green slag often have a fine powdery coating of secondary minerals consisting of  $\text{CaCO}_3$ , Ca alumino sulfate, and  $\text{MgCO}_3$ .

A sample of the site's dense blocky slag (C-s) was studied in detail to describe the alteration features observed. Alteration was not visible with the unaided eye, but thin sections of the sample showed a distinct zone of alteration (Figure 3-11). The zone is characterized by a ~0.4 mm thick reddish-brown alteration rind. The minerals are too fine grained to be determined with a petrographic microscope. At the SEM scale, the weathering features became quite apparent. In the unweathered interior, periclase dendrites are overgrown by spinel and these phases are usually surrounded by monticellite with the occasional forsterite. Moving towards the edge of the sample, a transition zone is encountered where intact periclase dendrites disappear, leaving an empty dendritic shape. At the very edge of the sample, periclase is completely weathered away leaving empty dendritic forms that are partially infilled by secondary iron oxides and iron hydroxides. Also, within the weathered zone, metallic iron prills are rimmed with secondary iron oxides and hydroxides. Secondary iron phases also fill cracks in the weathered rind and rim the euhedral spinel crystals.

### 3.3.4 Estimation of Weathering Rate

As mentioned in the text preceding Equation (3), the weathering rate  $v_p$  can be estimated if one has information on the history of the slag's shape. For example, a slag sample at Site C weathered to a depth of .035 cm over 50 years, so that  $v_p = 0.007$  cm/yr. Equation (12) can be used to estimate the bulk release of U and Th (combined molecular weight of 470 g/mol) from the slag. U and Th occur in this sample as  $\text{UO}_2$  and  $\text{ThO}_2$  (combined molecular weight of 534 g/mol) in perovskite (density of 4.1  $\text{g/cm}^3$ ) with no surface weight percent, a combined bulk weight percent of 0.2, and a modal abundance of 4.6%. Using Equation (12), one can estimate the bulk mass flux to be 230  $\text{ng/cm}^2\text{-yr}$ .

### 3.3.5 Distinguishing Between Primary and Secondary Phases through the Use of Artificial Melts

To distinguish between the primary phases that formed during the initial cooling of the slag and the secondary phases which formed after the slag weathered, we melted a powdered Sn slag from Site B in a Burrell electric furnace. It required a

temperature of around 1525°C to melt the powdered slag. Following cooling of the melt, microprobe analyses of the resulting material indicated the presence of perovskite, gehlenite, clinopyroxene along with glass Figure 3-12. By comparing this laboratory produced slag with Sn slag collected at Site B (sample B-5- 5.5) we concluded that the secondary phases consist of Ce silicate, Ce aluminosilicate, feldspar, wollastonite, barium aluminosilicates, clays, and gypsum.

### 3.4 Artificially Weathered (Leached) Samples

It is recognized that weathering and therefore potential leaching of U and Th from the slags may occur at different rates depending on the solution chemistry. In an attempt to quantify this effect, A. Felmy and D. Rai, PNNL, (Felmy, et al., 1999) performed a series of leaching experiments on splits from several slag samples collected at Sites A and B. The slags were leached with deionized water and with solutions at pH ranging from 0.5 - 12. Splits of the solid portion from the PNNL slag leaching studies were investigated at JHU. Samples of unleached slags, slags leached with deionized water, and slags leached under different pH conditions were characterized by SEM and quantitative electron microprobe analyses to compare the effects of leaching on the degradation of the various phases.

The samples were prepared in several ways that allowed the authors to examine the leached surfaces, and to determine changes in mineral and glass chemistry due to leaching. Pieces of the leached solids were mounted on microprobe sample holders, carbon coated and analyzed by Secondary Electrons to view the surface morphology, thereby providing a qualitative image of alteration. Other pieces were mounted in epoxy, then polished, carbon coated which allowed for detailed elemental analyses by wave-length dispersive X-ray analysis (WDS) of the crystalline and glass phases.

SEM images of a Sn slag (B-5.5) from Site B leached by deionized water are shown in Figure 3-13. The glass in these images has been partially dissolved. Perovskite and gehlenite protrude slightly from the glass surface. Fine grained needle-like precipitates litter the glass. The secondary mineralization is too fine grained for accurate analysis by electron microprobe.

SEM micrographs of slag surfaces of a Nb-Ta slag (96TC-19) from Site B leached under varying pH conditions are shown in Figure 3-14. Figure 3-14 is an image of a glass surface leached at pH 0.5 and pH 2. The glass exhibits dehydration cracks, pitting, and crystal precipitation. Calzirtite, perovskite and hibonite crystals protrude from the glass. Crystallites of secondary phases are precipitated on the glass surface. Pitting of the glass occurs at pH 0.5. The (100) surface of hibonite crystals appears to be relatively unaffected by the acidic solution, however the (010) surface shows signs of dissolution

perpendicular to the axis (Figure 3-14). It is likely that the Ca ions which occupy sites between octahedral and tetrahedral sheets in the hibonite have been leached or exchanged at this pH (Figure 3-14). This is reflected in the chemistry of the glasses and minerals. A plot of microprobe data from leached glasses of 96TC19 shows a depletion in CaO and Al<sub>2</sub>O<sub>3</sub> at pH < 4, accompanied by an increase in SiO<sub>2</sub> (Figure 3-15).

Figure 3-16 shows an analysis of the effect of leaching hibonite in Nb-Ta slag sample 96TC19 over a pH range from 0.5 to 12. The UO<sub>2</sub> content of the hibonite was low and its UO<sub>2</sub> made up < 0.02 wt % of the hibonite. Little of the UO<sub>2</sub> appears to have been leached from the hibonite between pH 0.5 to pH 12. ThO<sub>2</sub> was slightly more abundant and it made up to 0.19 wt % of the hibonite. The most significant leaching of the ThO<sub>2</sub> was between pH 0.5 and pH 2.

The data indicate that Al<sub>2</sub>O<sub>3</sub>, TiO<sub>2</sub>, and ThO<sub>2</sub> are depleted in the low-pH range, 1-4. MgO and CaO content has increased in the low pH range. SEM images of the above analyzed samples are seen in Figures 3-17, 3-18, and 3-19. A BSE image of thorianite in this sample, Figure 3-20, indicates a similar trend, i.e. depletion of certain elements in the low pH range (Figure 3-16). These data may help to explain some of the leaching and solubility data obtained by PNNL for these slags.

### 3.5 Archaeological Slags

#### 3.5.1 Introduction

Since standardized leaching tests give information only about short-term processes, archaeological slags are being studied to determine their long term leaching behavior and weathering characteristics. Comparison of the leaching behavior and weathering characteristics of slags covering a span of ages will yield information about how certain phases withstand exposure to weathering over the long term. To perform this comparison, a small suite of samples was collected from archaeological sites (Table 3.1). Such characterization of archaeological materials is necessary for understanding and defining the mechanisms of long term alteration and weathering of a slag, which, in turn is important for assessing the hazards that slag presents to its surrounding environment. Defining these mechanisms may also be pertinent to determining the safety and effectiveness of glass and ceramic waste forms. The weathering mechanisms that affect slags are closely linked to the individual phases and their composition. Before the specifics of alteration can be defined, all phases present in the system must be identified. The processes of alteration and weathering ultimately determine the relationship between slag piles and their surrounding environments. Understanding these processes may signal the need to take a closer look at the current uses of slag (e.g. as building material and as a soil additive) and current remediation techniques for large slag piles.

Most slag studies associated with archaeological sites look to the composition and morphology of slags for information about ancient smelting processes rather than their long term weathering characteristics (e.g. Franklin et al., 1976; Mascaro et al., 1995). Slags and metallic artifacts are often the only indicators for the smelting conditions and the original ingredients of the smelt which may be of interest to those reconstructing the history of an area. For example, excavations in Göltepe, Turkey, found a small piece of vitreous material (slag) melted to the wall of a crucible (Vandiver et al, 1992). Further studies and a comparison to a medieval tin slag from Cornwall, England, indicated that the Göltepe sample was formed by a tin smelting process (Adriaens, 1996).

Unfortunately, detailed, full-scale mineralogical surveys which would provide information on the long term weathering of slag are rare in investigations of ancient slags. Compositional zoning and trace element content are not usually included in petrochemical descriptions of the phases (e.g. Maskall et al., 1995; Adriaens, 1996; Gee et al., 1997). Knowledge of such small-scale information may not be obviously useful for archaeological studies, but is very important for understanding the possible contamination emanating from a smelting site. With rising concerns about the pollution associated with ancient and modern metallurgical sites, archaeologists and geologists have begun examining elemental migration (e.g. Mascall et al., 1995). In the Czech Republic, lead and other heavy metals are being leached from large slag heaps and are polluting nearby streams and soils. Lead leached from ancient metal working sites has also become a concern for drinking water sources in Greece (Voutsinou-Taliadouri et al., 1995; Sharp, 1997). More recently, slags that were crushed and added to soils to raise the pH have been pinpointed as the source of vanadium that poisoned herds of cattle (Frank et al., 1996). Again, many of these studies present bulk chemical data but do not present detailed information about the individual phases present in the slag.

#### 3.5.2 Dating of Archaeological Slags

At many archaeological sites, slags serve as the sole "witnesses of metallurgical activity" (Mascaro et al, 1995). At some locations they are surficial indicators for unexcavated metal working facilities, as was the case at Crift Farm, Cornwall, England (Figure 3-21). Dating of such material can be challenging. Obtaining an absolute age (age in years before the present) is often impossible due to the lack of organic material (such as charcoal or pieces of unburned wood) that can be dated by <sup>14</sup>C methods. When such material is absent, relative dating techniques are used. Relative ages are based on the relative position of material within a vertical column and association with other datable artifacts. In an undisturbed pile of slag the material at the base of the pile is older than the overlying material. If the

layering of a pile has been disturbed or re-worked, or if the deposition surface was not horizontal, such age correlations are more complicated, and in some cases, totally unreliable. For example, at the Crift Farm site in Cornwall, England, small pieces of glassy slag are dispersed throughout the soil. The soil has been tilled and re-worked and thus the small pieces of slag, the rare potsherd, and even larger artifacts such as a large rock that appears to be a grinding stone, elude dating.

The juxtaposition with datable material can also yield a relative age for a slag. Potsherds (with chemical dates or relative dates due to their style and decoration) incorporated into a slag pile can give a relative age for the slag. In Cyprus, the slag pile at Skouritossa mine has Roman-aged potsherds associated with the lower section of the pile which implies an age of approximately 2,000 years before present for the base of the pile.

All of the samples associated with this study of archaeological slags have relative dates except for the Cornish slags, which have a  $C^{14}$  date of 1125 A.D. (Earl, 1998). In some cases, sample ages are constrained by knowledge of how long a smelting site was in operation (as is the case with the Cu slags from Hayle, Cornwall, UK). Samples from the Czech Republic have relative ages based on their MgO content, since there is documentation about the changes in the composition of the ore and flux over time.

### 3.5.3 Archaeological Slags Investigated

Table 3.1 contains a list of archaeological slags investigated in this study. They include tin slag from Malaysia and Great Britain (Figure 3-21), Late Bronze age copper slag from Cyprus, and lead and silver slag from the Czech Republic Figure 3-22. These slags range in age from ~ 2 years old to over 2,000 years old. Transmission electron microscopy, electron microprobe analyses, X-ray spectroscopy, and traditional optical microscopy were used to identify and describe slags' components. In particular, the distribution of rare earth, radioactive, and/or toxic elements among primary and secondary minerals was determined by Farthing (2002).

#### 3.5.3.1 Tin Slag from England and Malaysia

Tin slags from England and Malaysia were collected for comparison to the slag from Sites A, B, and C. The tin slag from Malaysia is quite complex mineralogically, with some samples featuring more than 20 individual phases. Still it is hoped that the mineral assemblages of the Malaysian and English slag will be comparable, and that textures and phases associated with alteration will be more prevalent in the older samples from England and Malaysia than in the samples from Sites A, B, and C. To assist in determining the effects of weathering, cassiterite ( $SnO_2$ ) ore from one of the Cornish tin mines could be smelted to create an 'age-zero' unweathered slag.

The phases in this 'age-zero' slag can be compared with the older Cornwall Slag to determine the changes due to weathering of an ancient slag and to project what might have been lost with time. The fact that we were unsuccessful in finding archaeological Sn slags from the UK much older than 1000 years may be the result of devitrification and other processes that have consumed the very old slags.

#### 3.5.3.2 Copper Slag from Cyprus

A sample of a Late Bronze Age copper slag from Skouritossa, Cyprus, was incorporated into the study of the long-term weathering and leaching of slag. Although the composition of the Cyprus slag is not analogous to that of the tin slags, it may offer an insight to the behavior of glass. A thin-section of the sample features long crystals of olivine (Figure 3-23). Glass is usually the host material for slag crystals, but in the Cyprus sample, the area between the olivine laths is no longer glass. Complete devitrification of the interstitial glass is observable, and is also supported by a flat background in powdered XRD spectra of the bulk sample which is seen in Figure 3-24. The composition and identity of the alteration product are unknown at this time. The lack of glass observed in the Cyprus slag raises the question of whether the absence of glass is consistent throughout the slag pile. Examination of other samples from this site would indicate if this was indeed the case. Also, the material around the olivine laths should be identified to help define the mechanisms and reactions that might have caused the breakdown of interstitial glass.

#### 3.5.3.3 Lead and Silver Slag from the Czech Republic

Our investigation of lead and silver slag from Pribram, in the Czech Republic, was only preliminary. The bulk chemistry of the Pribram slag differs from the Site A, B, and C slags (Figure 2-10). Careful investigation of the phases present in the Pribram slag would need to be done for comparison with the slags from Sites A, B, and C. Because pitchblende (uraninite- $UO_2$ ) was inadvertently incorporated into the Pribram smelting process there may be mineralogical similarities of Pribram with Sites A, B, and C. With regard to weathering, the samples from Pribram range in age from 2 to >100 years old. The ore and the processing techniques have been relatively constant over this span of time, making the Pribram slag an ideal candidate for investigating weathering through time.

### 3.6 Summary of Weathering Mechanisms of Slag

The following weathering mechanisms are evident in the slag from sites A, B, and C: (1) formation of weathering rinds through oxidation, (2) devitrification of the glass accompanied by formation of voids, (3) leaching of glass and crystalline phases along fractures and grain boundaries, (4) precipitation of secondary phases, and (5) possible microbial activity.

All of the above lead to the formation of secondary minerals. As noted previously, the slags were formed under strongly reducing conditions. When exposed to oxidizing conditions, such as found at or near the ground surface, weathering is rapid and many if not most of the samples collected had weathering rinds up to several cm thick. Weathering is also visible on a microscopic scale and glass corrosion could be seen along fractured surfaces as seen in the upper photograph in Figure 3-2. This is an image of an archaeological slag, several hundred years old and the glass alteration along the fractures is quite evident. Devitification also occurs and this is accompanied by a negative change in volume that results in voids within the slag (Figure 2-7). In the case of natural glasses, weathered basaltic glasses form palagonite, a vitreous, red, yellow or brown, fine-grained mixture of clays and silicates (Jervinovic and Ewing, 1992). Likewise, we see evidence of palagonite formation in the Site B and Site C slags. The outer tens of microns of material in the Site C slag show a preferential dissolution of periclase, a Mg-Fe-oxide (Figure 3-25). Dissolution extends into the slag along and within the spinel grains. This indicates grain boundary diffusion of corroding fluids into the interior of the slag. Glass in the Site C slag (Figure 3-26) has oxidized and partially recrystallized to Fe-oxyhydroxides. Weathering along grain boundaries is fairly common in humid regions. With the passage of enough time, granitic and basaltic rocks often form saprolites in humid, near-surface

environments. Saprolite is a material that has all the textural features of the original rock, but, the minerals have been altered to clays, and oxides. This material is friable and does not have the structural integrity of the original rock. This is a likely scenario for the long-term degradation of the slag in an Eastern humid environment. The fact that we have been unsuccessful in finding archaeological Sn slags from the UK much older than 1000 years may support this conclusion.

The weathered slag provides information that can be used for estimation of a leach rate. For example, naturally weathered glass from Site B (Figure 3-8) shows a loss of 0.2 weight percent Th and 0.05 weight percent U from the outer 10 millimeters of the slag over a 30 year period. This information can be used in Equation (4) to estimate a 30-year leach rate.

Leach rates calculated using Equation (4) or (12) require determining the weathering rate for each phase. Although the weathering process appears to follow a steady-state law (cf. Equation (4)), the law is at best a quasi-steady state law. As Figure 3-27 shows schematically, the surface-concentration gradient will vary with time and from Equation (4), the degradation rate,  $v_p$ , also will vary with time. An estimation of this temporal variability requires an examination of young (e.g. SDMP) and archaeological slags.

**Table 3-1 Table for Estimating Leach Rate at Site B Based on Mineral Abundance in the Slag Samples.**

Phase	Modal Abundance	Wt% (U + Th) in phase	Wt% in Slag
Gehlenite	38.8	--	--
Glass	36.3	~ 0.25	~0.09
Clinopyroxene	10.1	-0.02	-0.002
Perovskite	9.5	~0.53	~0.05
Calzirtite	4.4	~0.46	~0.02
Rutile	1.98	--	--
Pyrochlore	0.05	~1.66	~0.001
Alteration	0.4	--	
Cracks and holes	2.1	--	--

**Table 3-2 Archaeological Slags investigated in this study.**

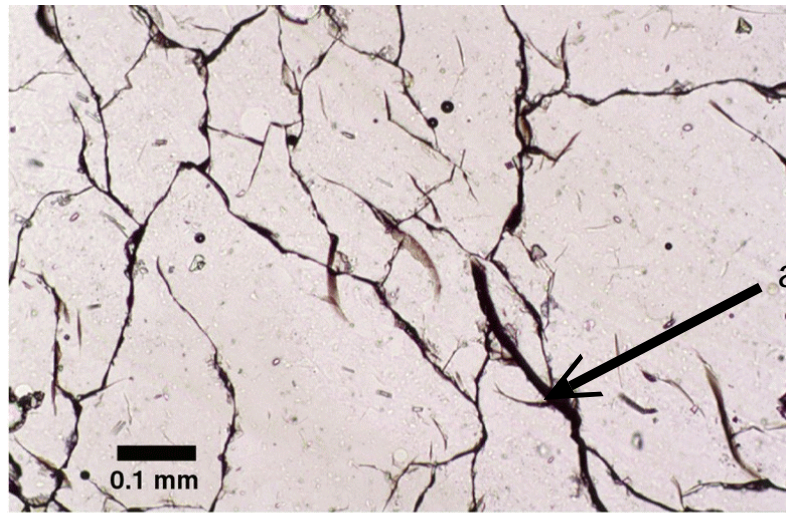
Location	Metal Extracted	Age
SW Great Britain (Cornwall and Devon) Crift farm Treireife*	Sn Sn	1100 - 1600 a.d. 1710 - 1896 a.d.
Lamb and Flag Seleggan*	Sn Sn	1715 - 1883 a.d. 1887 - 1931 a.d.
Chy-an-Dour*	Sn	1660 - 1910 a.d.
Charlestown	Sn	1834 - 1884 a.d.
Week Ford	Sn	640 - 17 <sup>th</sup> century
Eylesbarrow	Sn	1822 - 1831 a.d.
Hayle	Cu	~300 years old
Czech Republic Pibram	Pb and Ag	~2 to 100 years old
Cyprus Skouritossa	Cu	Late Bronze Age (>1,000 years old)
Malaysia*	Sn	50-100 years old

\* indicates radioactive slag



Figure 3-1. Weathered Slags from Sites A and B. Top photograph is of a Site A sample after it was split into two pieces. The contrast between a weathered and unweathered surface can be seen in the block in the foreground. The outer weathered surface is visible on the right edge of the block and it is a reddish brown material several mm thick. The unweathered interior is visible on the left and the alternating light and dark layers show up well. The lower photograph is of Site B sample B-5.5 after being split in the field. The outer weathered surface is visible on the top of the block on the left. It is a light tan color and is several mm thick. The unweathered interior is very dark gray in color.

200 year old slag  
from England



alteration



alteration

35 year old slag  
(Site B)

Figure 3-2. Photomicrographs of weathered slag under plane polarized light. The upper image is archeological slag from Lamb and Flag, UK (200 years old). The lower image is Site B slag ~35 years old. Alteration is seen along fractures in even this young slag. The small star shaped crystallites have a calzirtite composition.

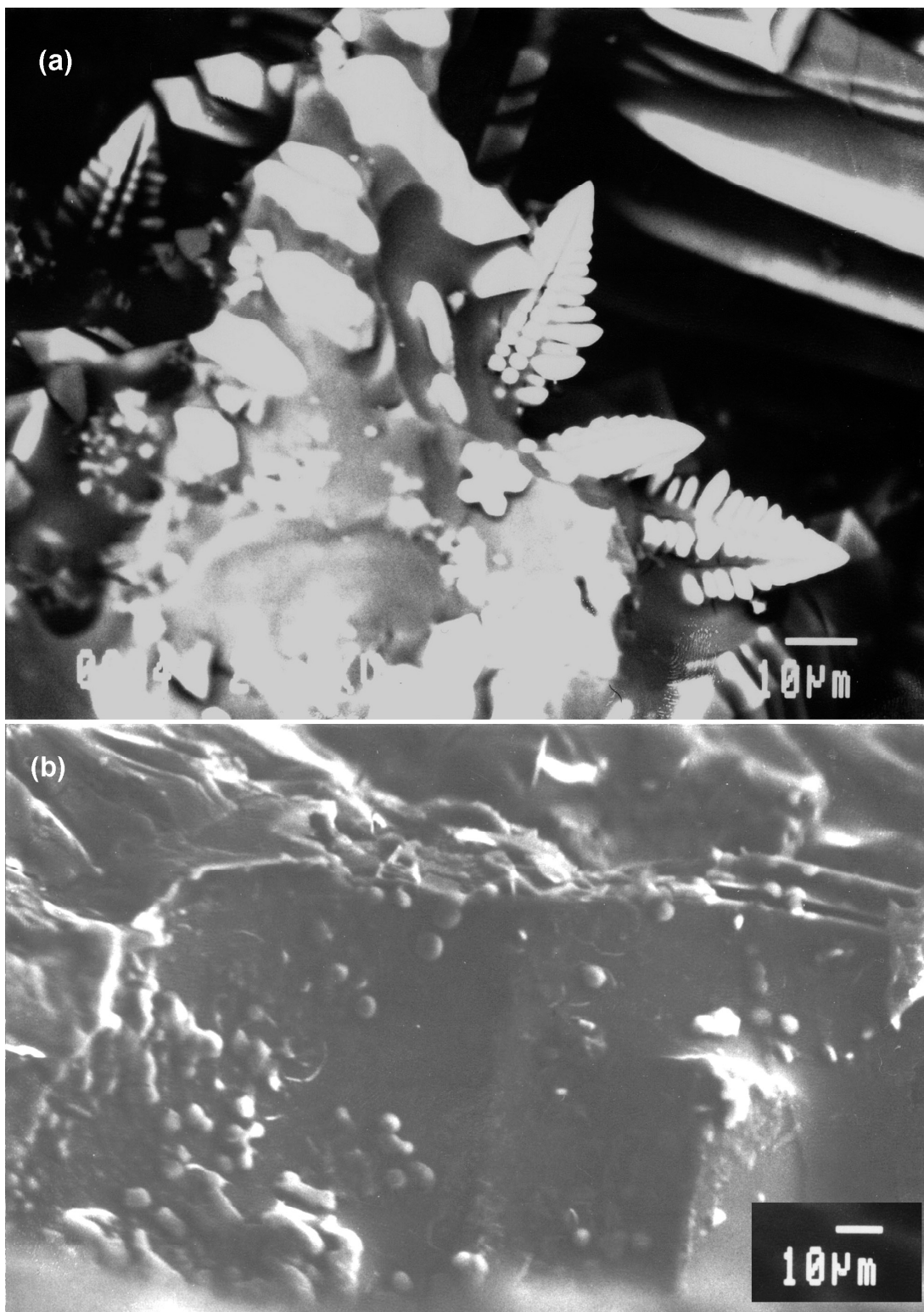


Figure 3-3. SEM images showing weathering features in Site B sample B-5.5. Sample is from PNNL and it was leached with deionized water. In the upper image perovskite and calzirtite protrude from weathered glass. In the lower image, round precipitates are visible on the glass surface. The precipitates have a high Fe content and might be the result of microbial activity.

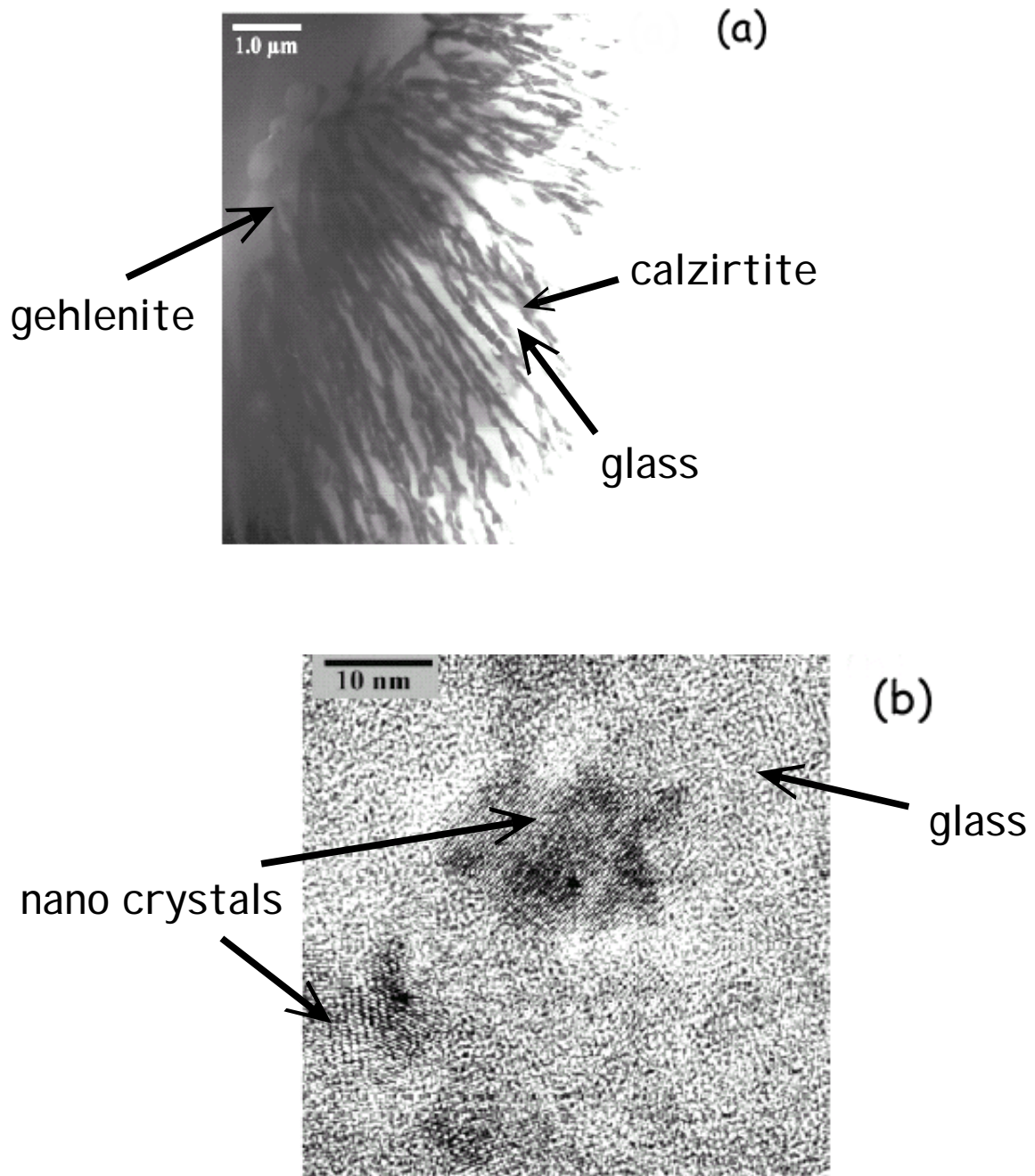


Figure 3-4. TEM images of Site B tin slag B8 showing weathering on a sub-microscopic scale. (a) HRTEM image of devitrification in glass. Small clusters of lattice fringes are visible and represent nano-crystals of gehlenite and calzirtite formed as the glass devitrified. (b) TEM image showing crystals of calzirtite nucleated on a gehlenite crystal.

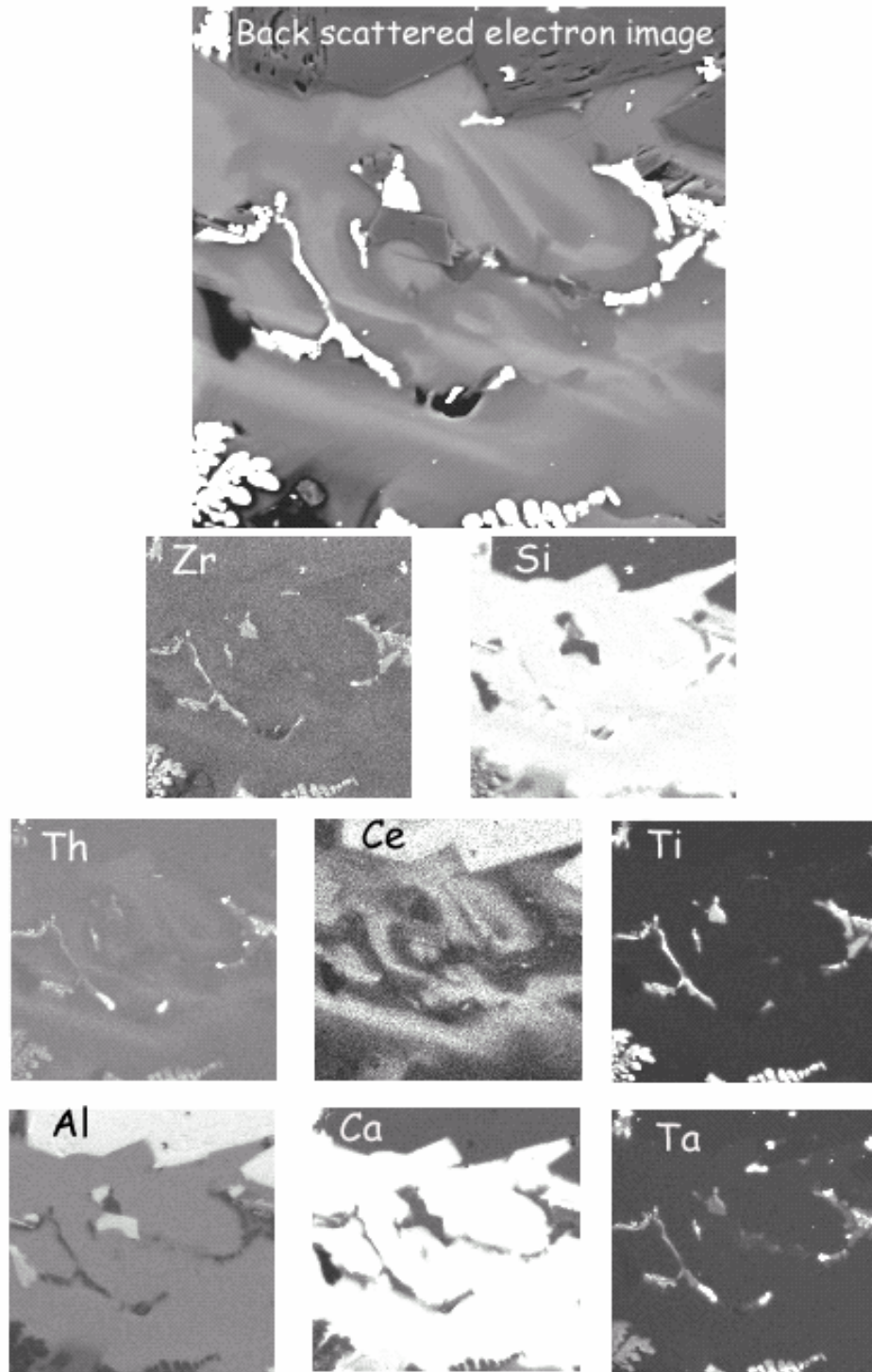


Figure 3-5. Back scattered electron (BSE) image of weathered Site B slag sample 96TC-19. The BSE image is at the top and the x-ray maps showing elemental variation are at the bottom. In the x-ray maps, the higher the relative concentration of a given element, the lighter the color. Thorium is associated with tantalite, pyrochlore, or zirconolite.

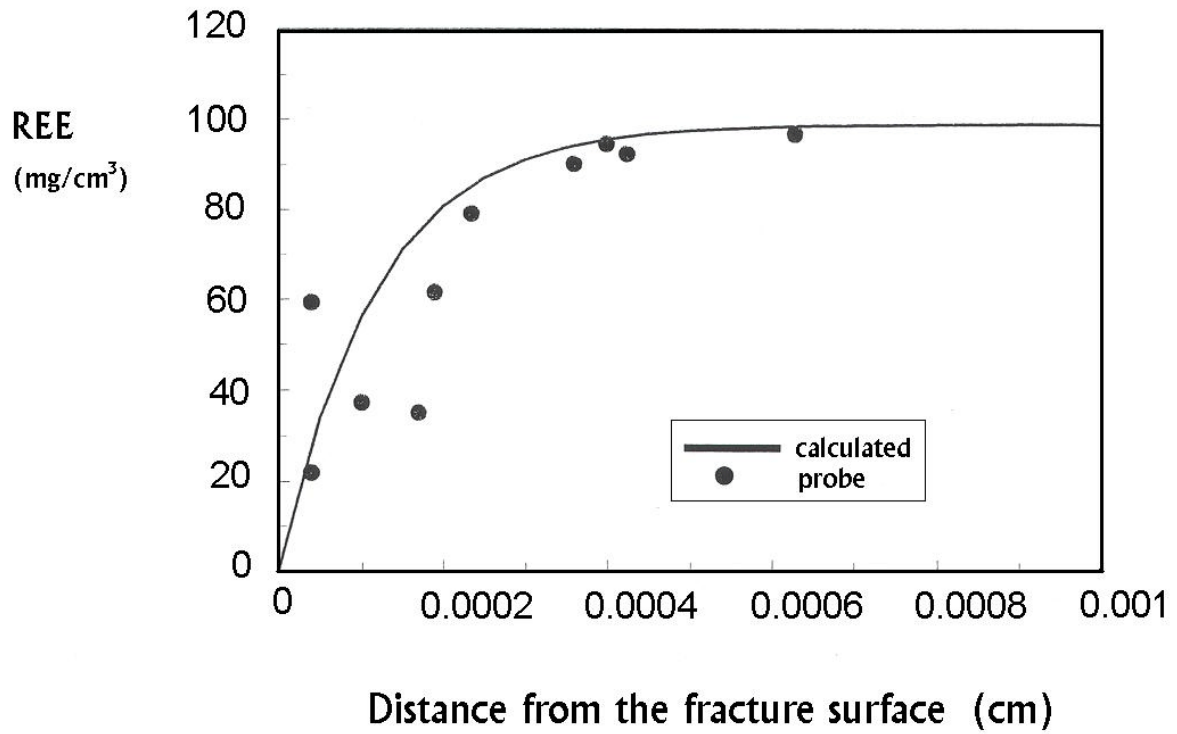


Figure 3-6. Microprobe analyses of Site B sample 96TC-19 showing variation in rare earth elements (REE) as a function of distance from a fracture. As can be seen in this graph, there is a depletion in the rare earth elements closer to the fracture.

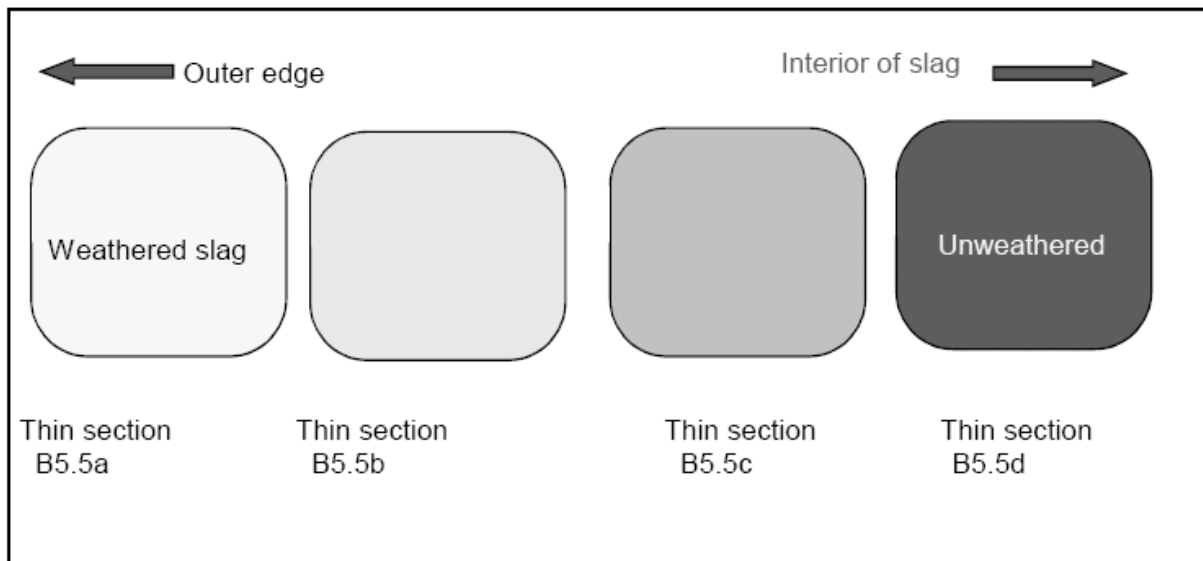


Figure 3-7. Schematic diagram illustrating location of elemental variation measurements from Site B sample B-5.5 as a function of proximity to a weathered edge. See Figure 1-1 for a photograph of B-5.5 being collected. Samples B-5.5a, B-5.5b, B-5.5c, and B-5.5d were cut from one sample with B-5.5a taken from the top weathered surface and B-5.5d from the bottom presumably unweathered surface. B-5.5b and B-5.5c are intermediate between the weathered edge and the interior.

### Site B Glass - 9 Traverses Across Thin Section

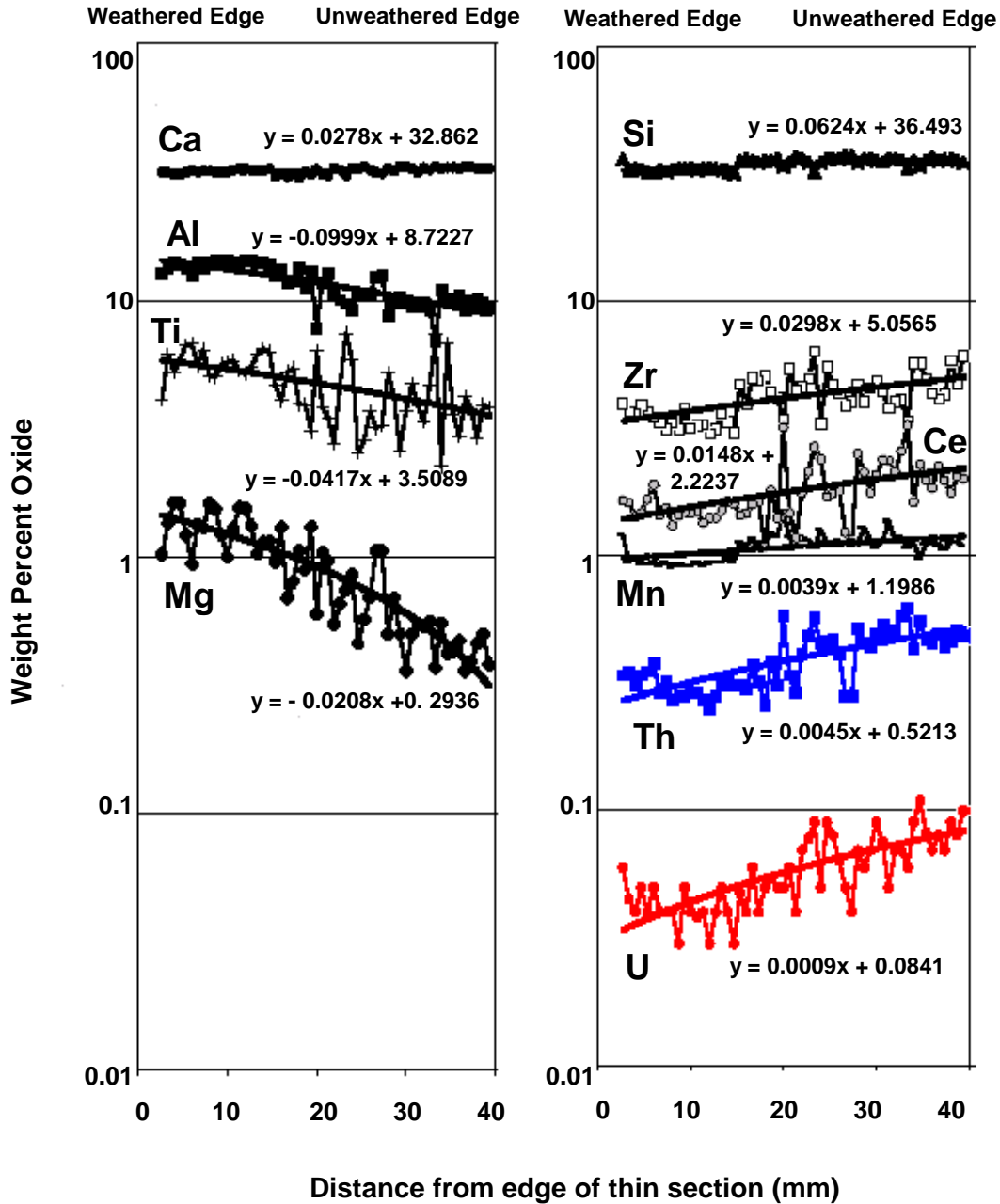


Figure 3-8. Chemical changes associated with weathering. These graphs of microprobe analyses show elemental variation associated with weathering. The sample is a Site B glass in which B-5.5a represents the outside of the sample and B-5.5d the unweathered interior. Note the elemental changes in the weathered sample. In approaching the weathered edge, there is an increase in the relative amount of Al, Ti, and Mg accompanied by a decrease in Zr, Ce, Mn, Th, and U. Ca and Si exhibit little change in amount. In contrast, elemental variation is negligible in the thin section of the unweathered sample and there is no depletion of Th and U.

### Site B Glass - Unweathered Thin Section

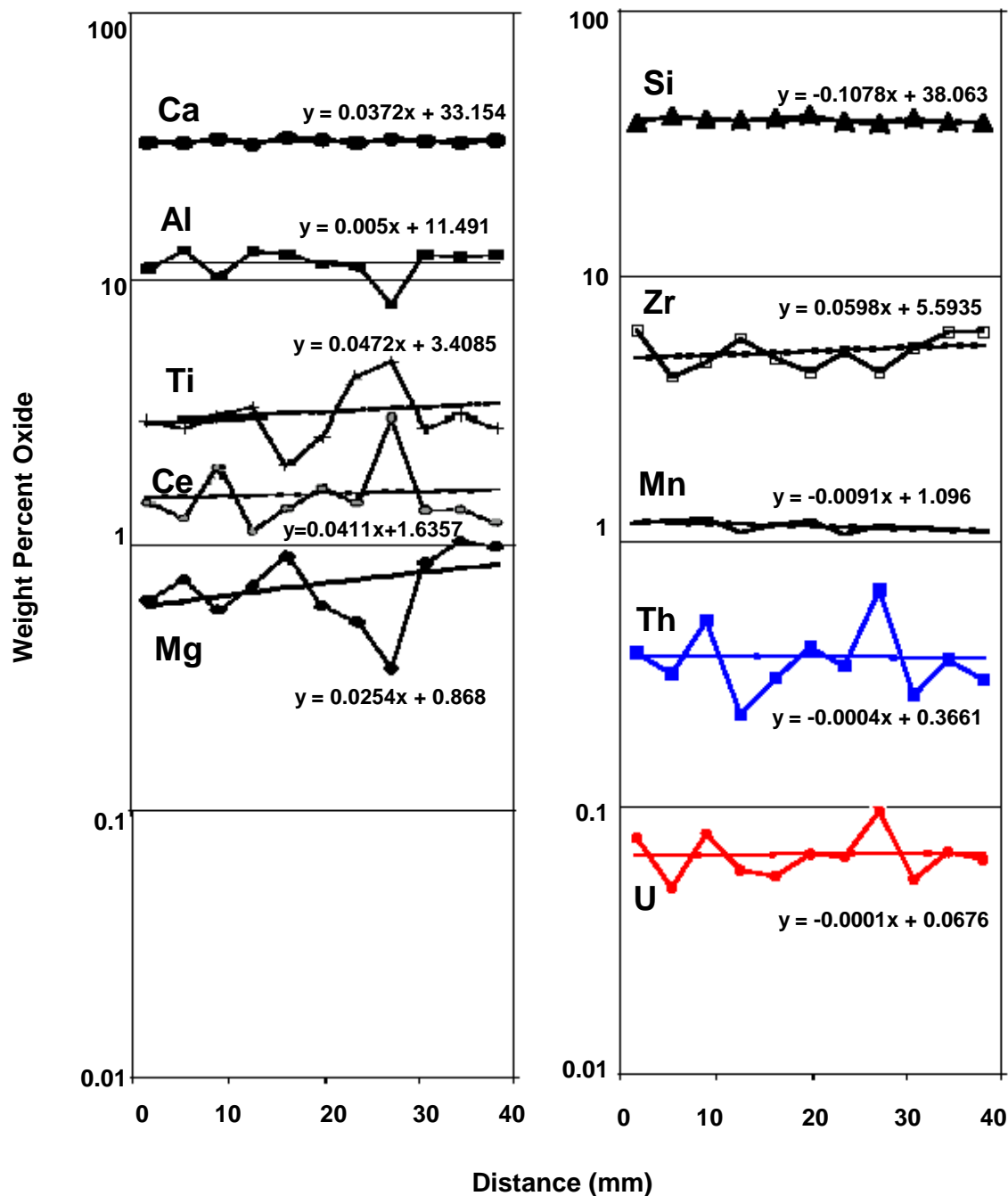


Figure 3-8 (cont'd). Chemical changes associated with weathering. These graphs of microprobe analyses show elemental variation associated with weathering. This sample is a Site B glass in which B-5.5d represents the unweathered interior of a slag block. Note that in this sample, B-5.5d, elemental variation is negligible in the thin section and there is no depletion of Th and U. In contrast, the elemental changes in the weathered sample (B-5.5a, pg 66), in approaching the weathered edge, there is an increase in the relative amount of Al, Ti, and Mg accompanied by a decrease in Zr, Ce, Mn, Th, and U. Ca and Si exhibit little change in amount.

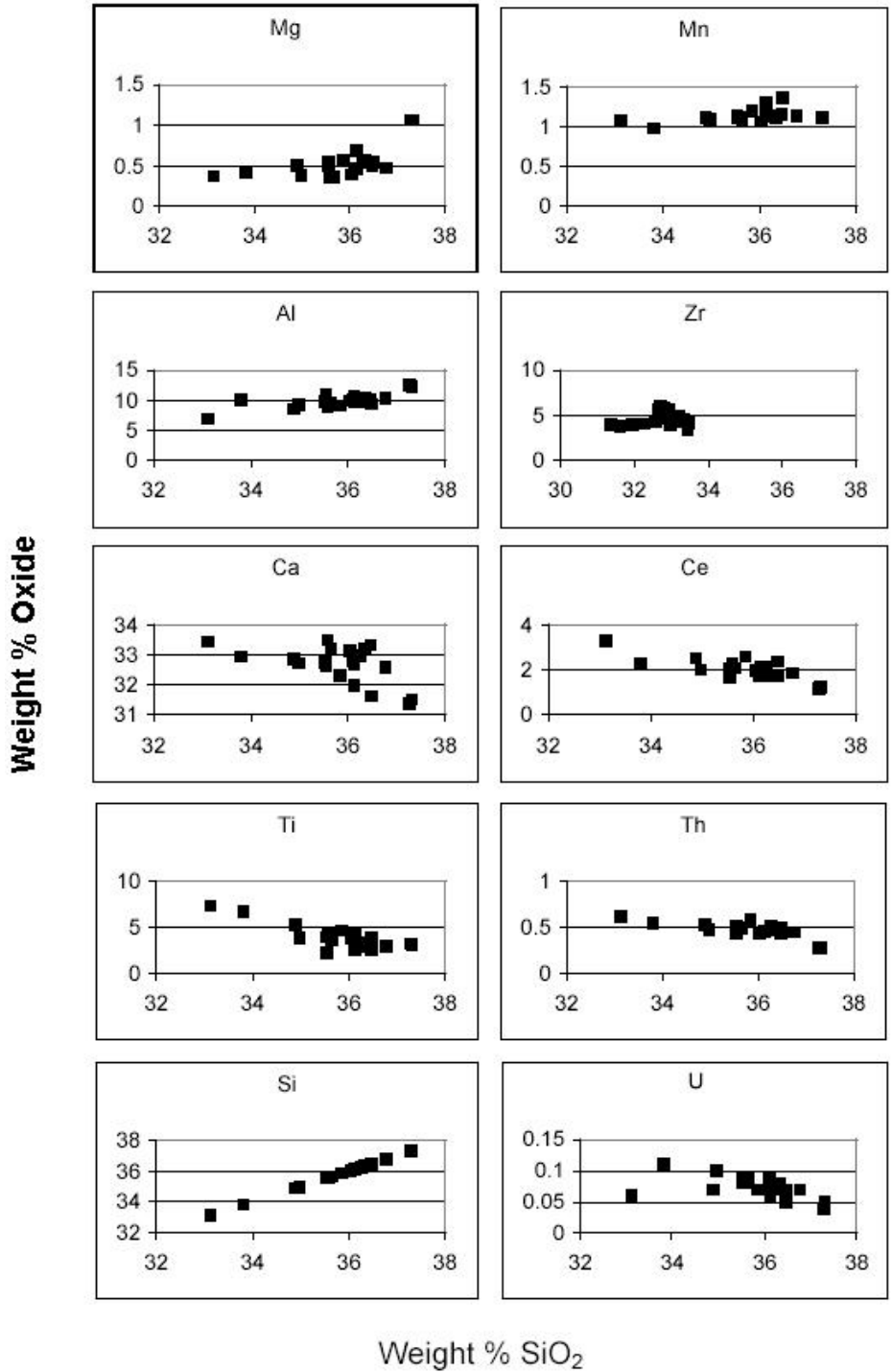


Figure 3-9. Compositional variation diagrams for Site B weathered glass. Note the degree of correlation of Al, Ti, Zr, and U with SiO<sub>2</sub>.

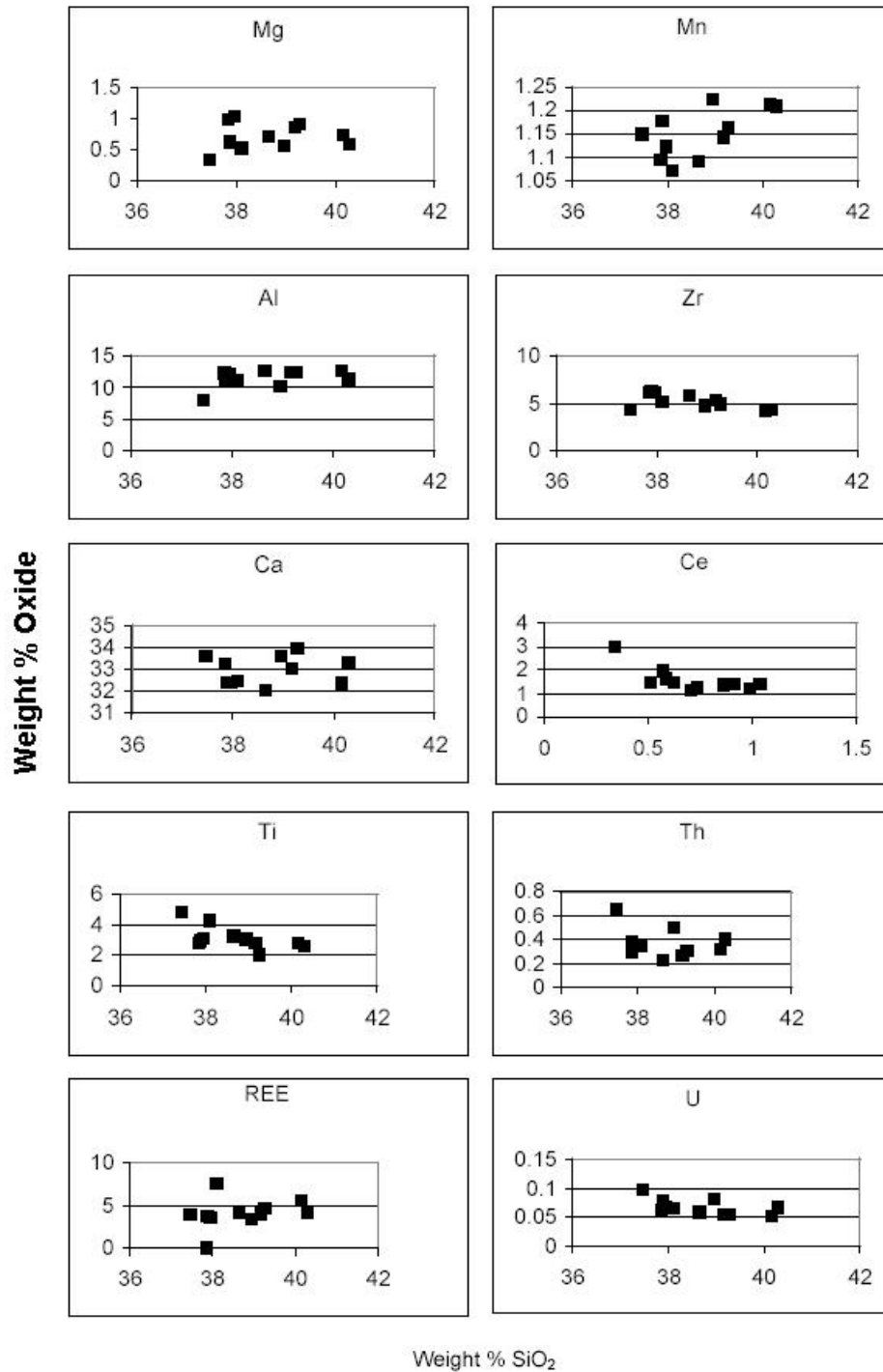


Figure 3-9 (continued). Compositional variation diagrams for Site B weathered glass. Note the degree of correlation of Al, Ti, Zr, and U with SiO<sub>2</sub>.

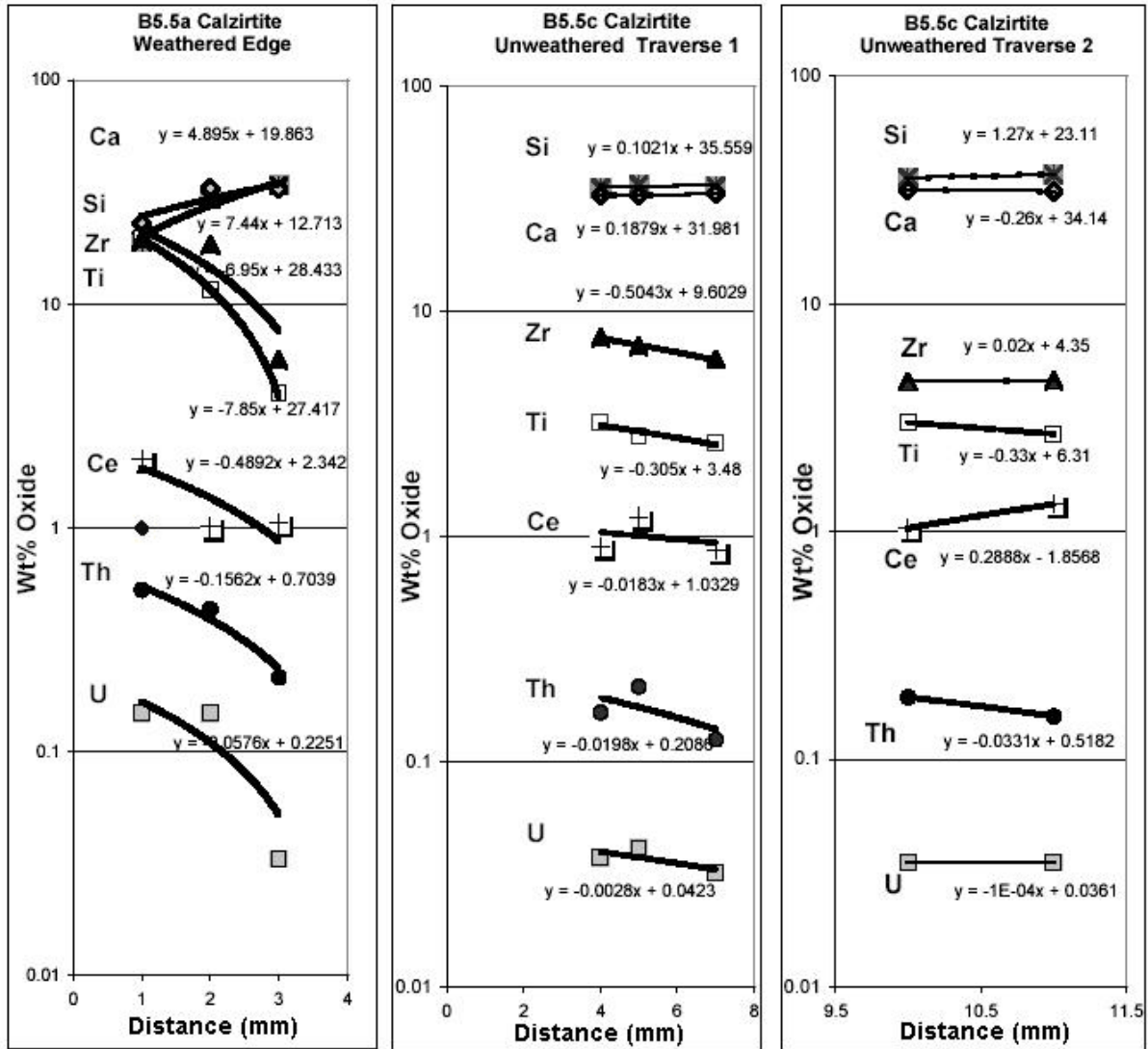
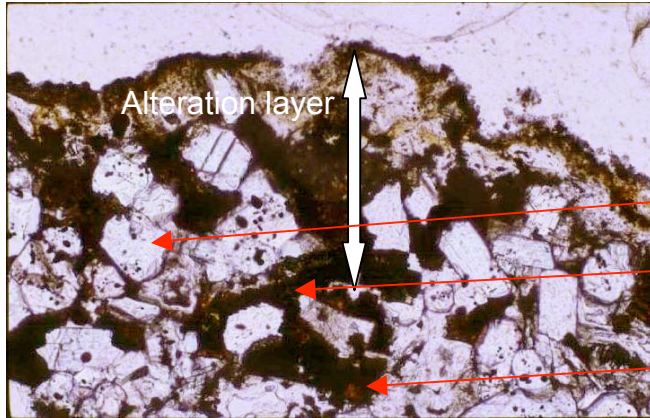


Figure 3-10. Electron microprobe analyses of Site B samples showing the elemental variation in calzirtite as a function of distance from a weathered edge. In the weathered slag (B5.5a) the weight percent of Ca and Si declines towards the weathered edge whereas the weight percent of Zr, Ti, Ce, Th, and U increases. In the two samples of unweathered slag (B5.5c) data were collected throughout the thin sections and there is little variation in values of the aforementioned elements. It is interesting to note that the weathered samples contain higher values of both Th and U compared to the unweathered samples.



Plane-polarized light

Ba aluminates

zirconolite

Cr spinel



Cross-polarized light



Reflected light

Figure 3-11. Photomicrograph of a weathered edge of a dense blocky slag (sample C-2a) from Site C. Alteration was not visible to the naked eye, but thin sections of the sample showed a distinct zone of alteration. The alteration zone is characterized by a ~0.4 mm thick reddish-brown alteration rind. The minerals of this zone are too fine grained to be determined with a petrographic microscope. At the SEM scale, the weathering products of this zone were identified as ardelite ( $\text{Ca}_2(\text{SO}_4)_2(\text{HPO}_4) \cdot \text{H}_2\text{O}$ ) and periclase ( $\text{MgO}$ ). The dark black material in the middle of the slide is perovskite. Other phases present in the sample are Ba aluminates, periclase, monticellite, Cr spinel, zirconolite, and metallic prills.

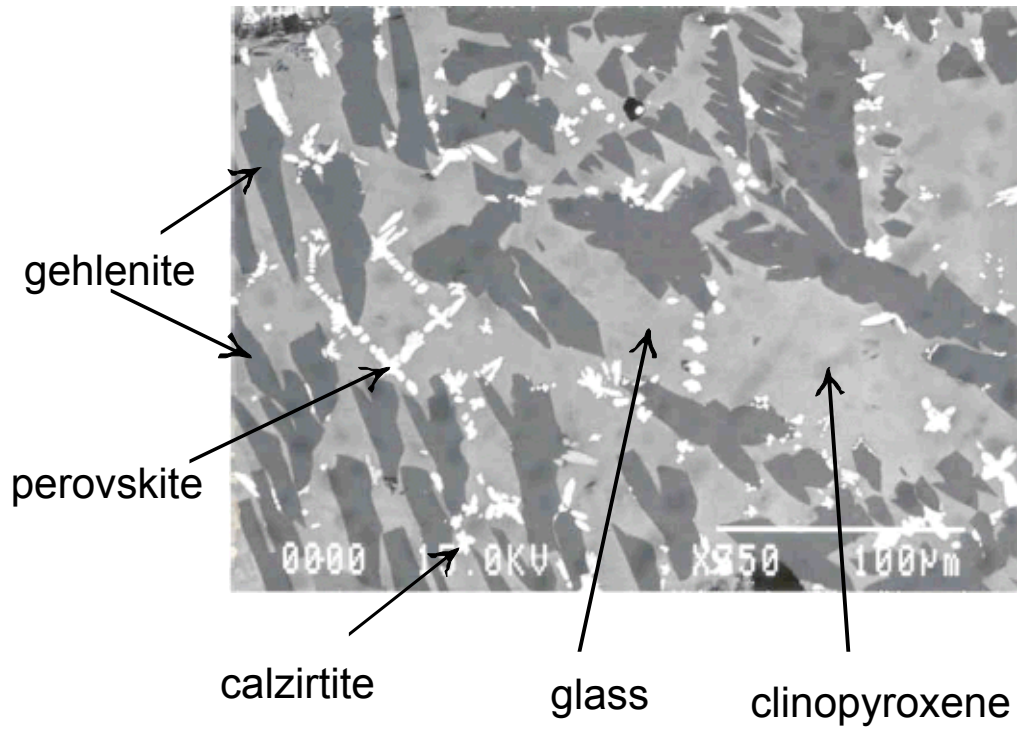


Figure 3-12. BSE image of remelted Site B slag. Note that there is no evidence of devitrification. The large dark gray crystals are gehlenite, the medium gray groundmass is glass, and the dark areas within the glass are clinopyroxene. The very light phases are perovskite which appear as dendrites, and calzirtite which form small star shaped clusters.

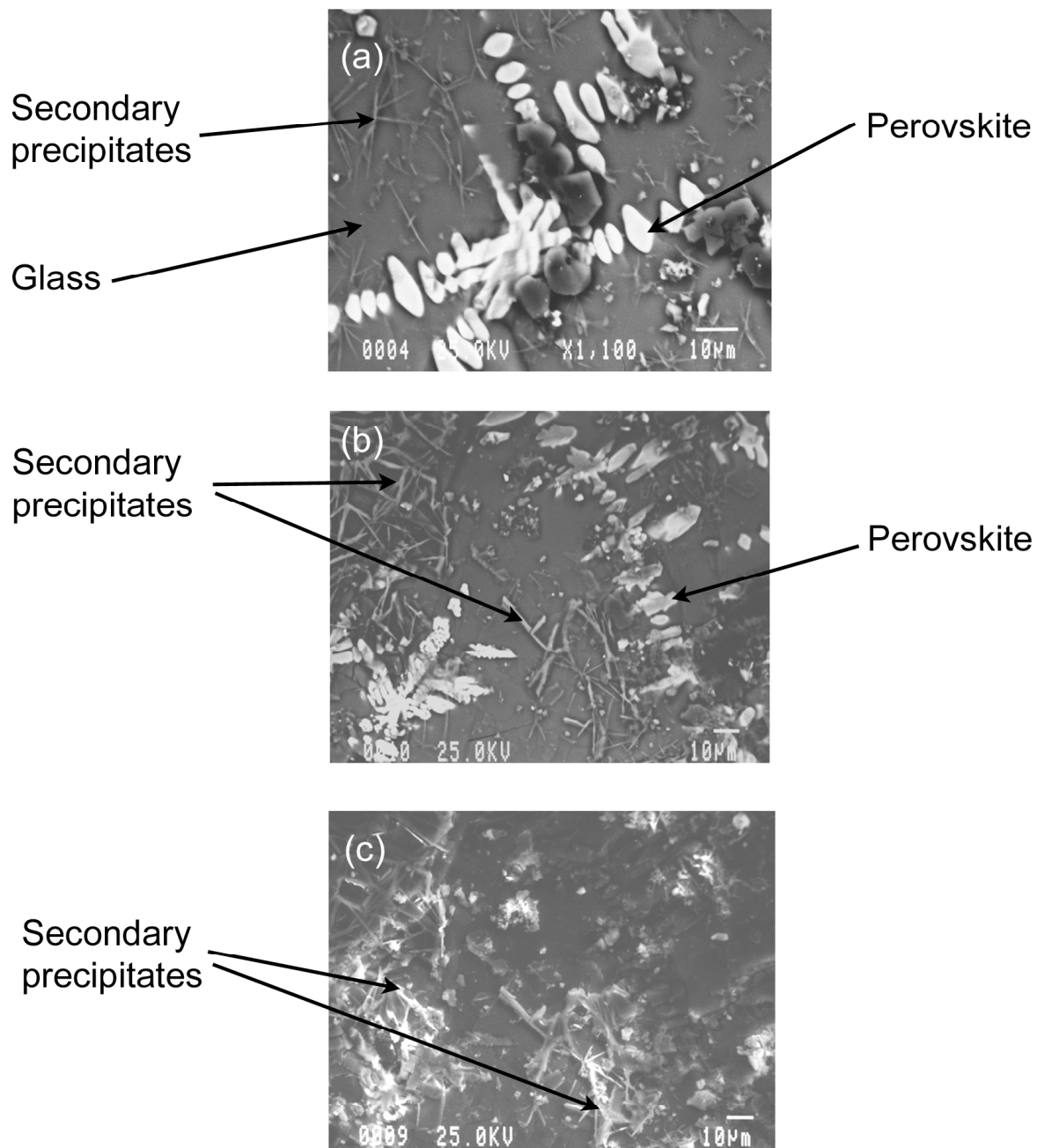


Figure 3-13. SEM secondary electron images of Site B Sn slag sample B-5.5 showing surface of the slag leached by PNNL with deionized water. Image (a) shows perovskite dendrites (white) protruding from the glass (dark gray). Smaller needle-like precipitates of clay (?) are visible on the glass surface. Images (b) and (c) have abundant needle-like precipitates on the glass surface.

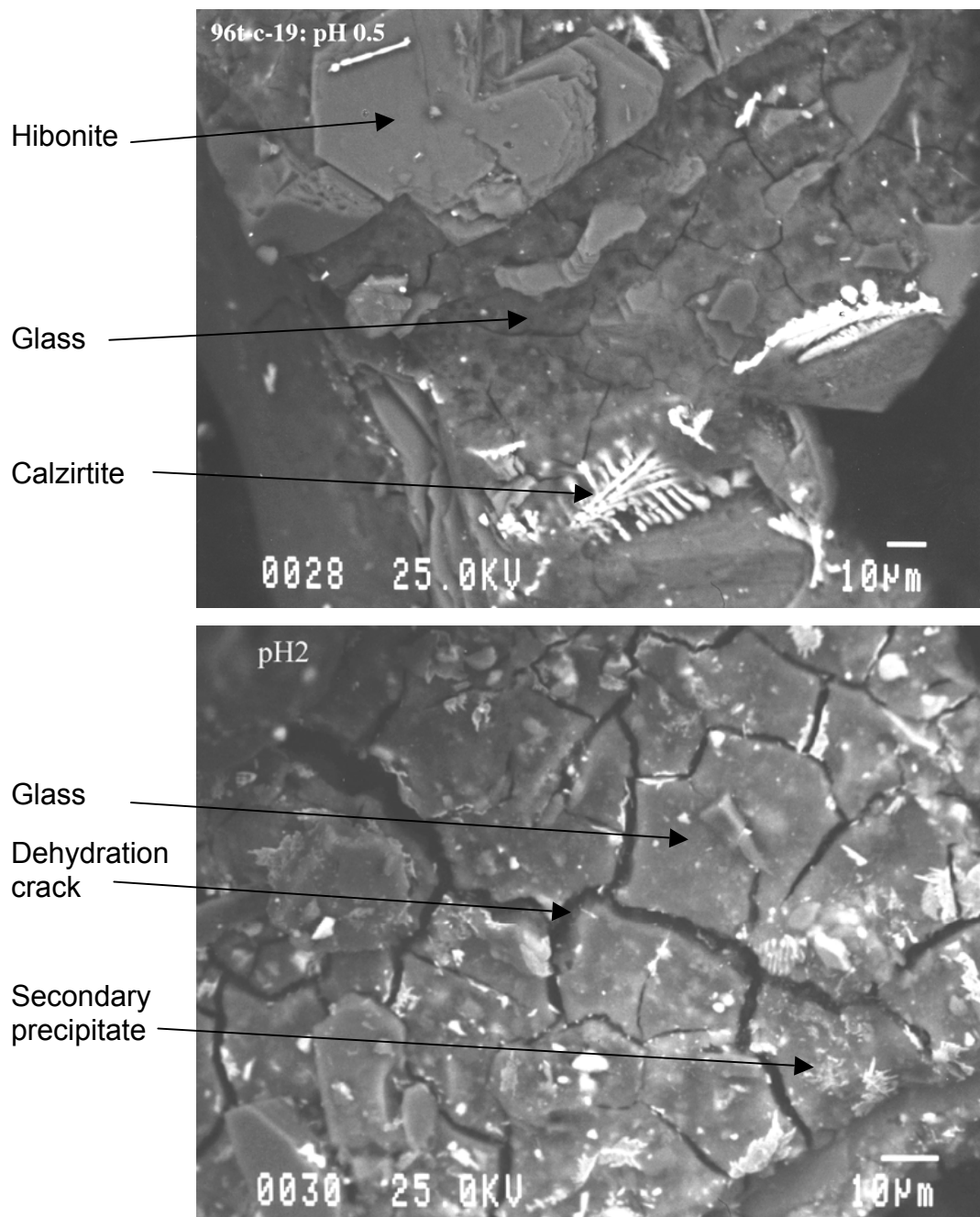


Figure 3-14. SEM secondary electron images of Site B Nb-Ta slag sample 96TC-19 after leaching by PNNL at pH 0.5 and pH 2. The upper image (a) shows the surface after leaching at pH 0.5. There is evidence of glass corrosion, dehydration cracking and attack on hibonite. The lower image shows the slag after leaching at pH 2. The glass exhibits dehydration cracks, pitting and crystallites of secondary phases are visible on the surface of the glass.

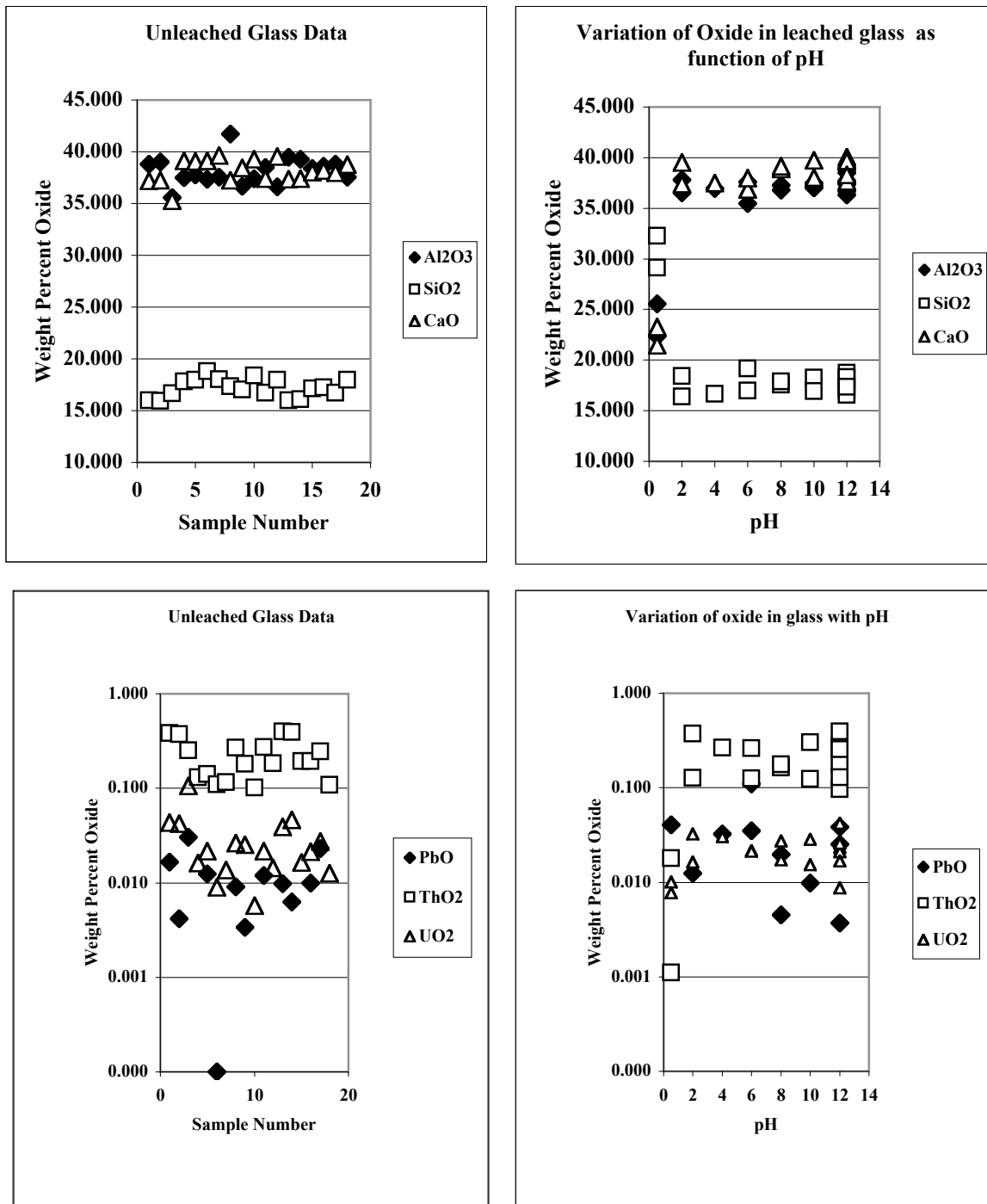


Figure 3-15. Elemental variation of glass in unleached and leached Site B sample 96TC-19. Leaching was done by PNNL from pH 0.5 through pH 12. The greatest effect on CaO, Al<sub>2</sub>O<sub>3</sub>, and possible Ce<sub>2</sub>O<sub>3</sub> are from pH 2 and below. There appears to be leaching in that range. However the pattern with Th, U, and Zr is not as simple.

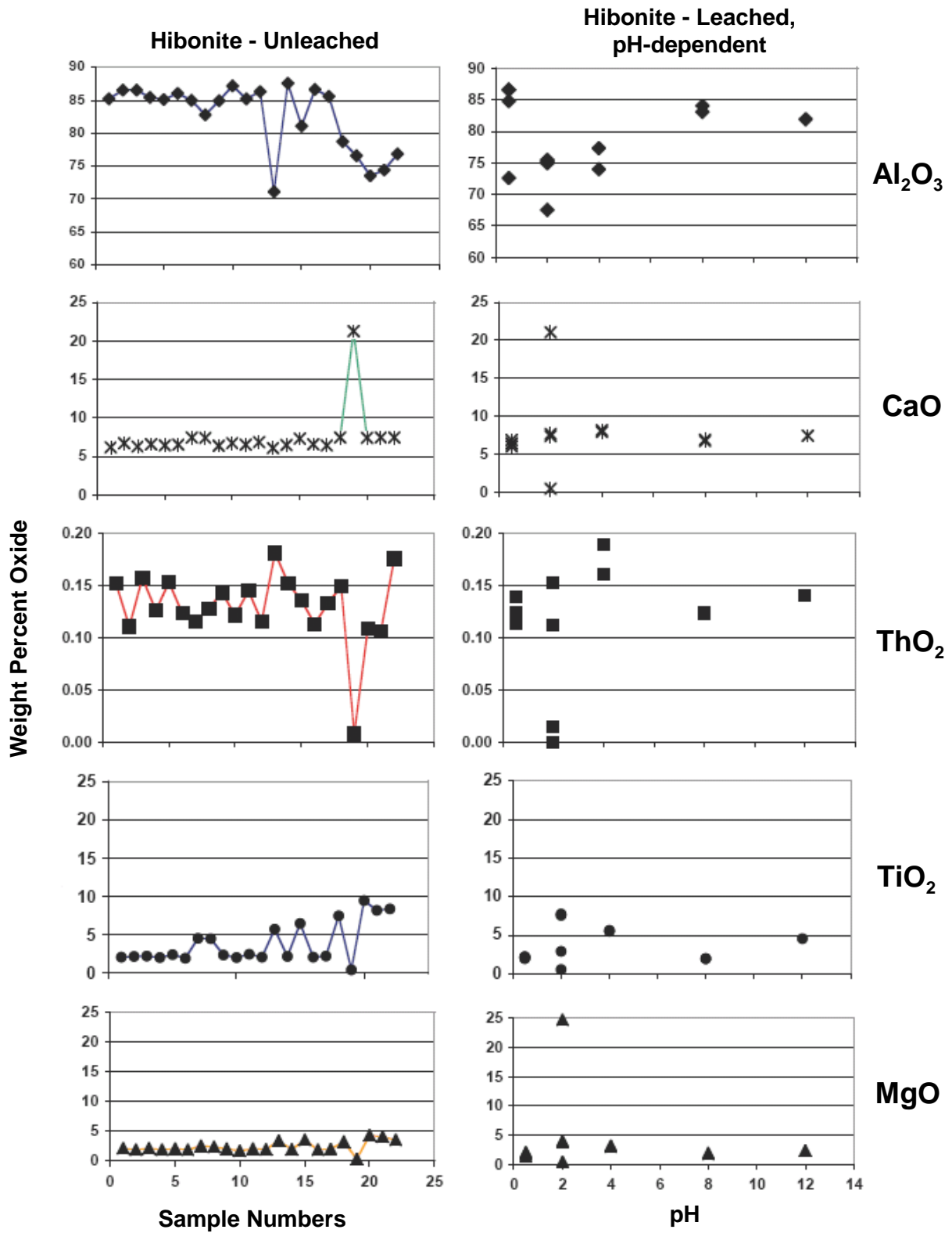


Figure 3-16. Elemental variation of hibanite in unleached and leached Site B sample 96TC-19. Leaching was done by PNNL from pH 0.5 through pH 12. The greatest effects are from pH 2 and below, and there appears to be leaching in that range.

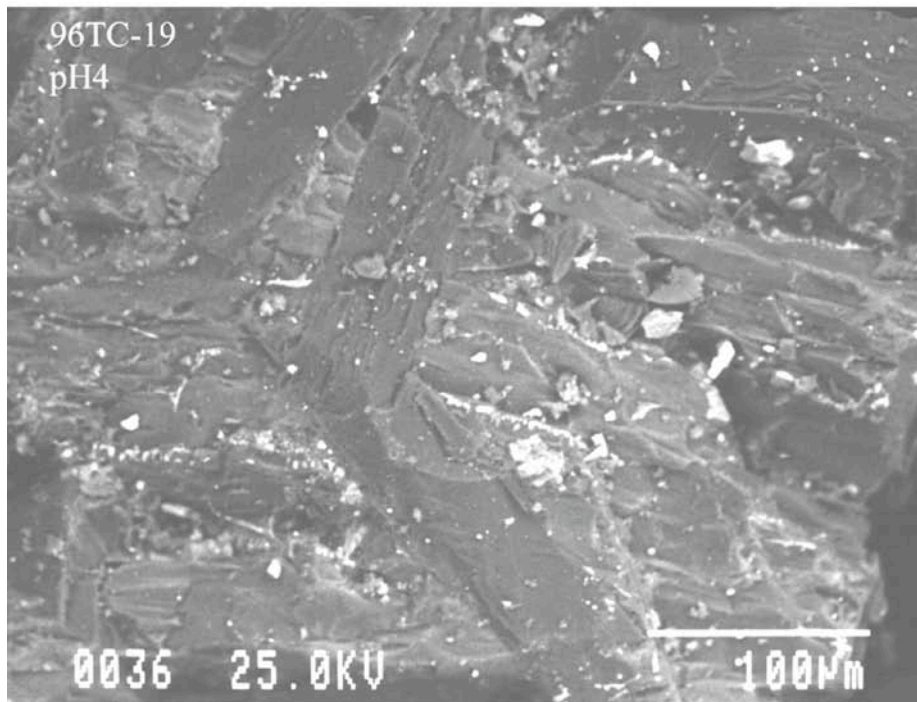
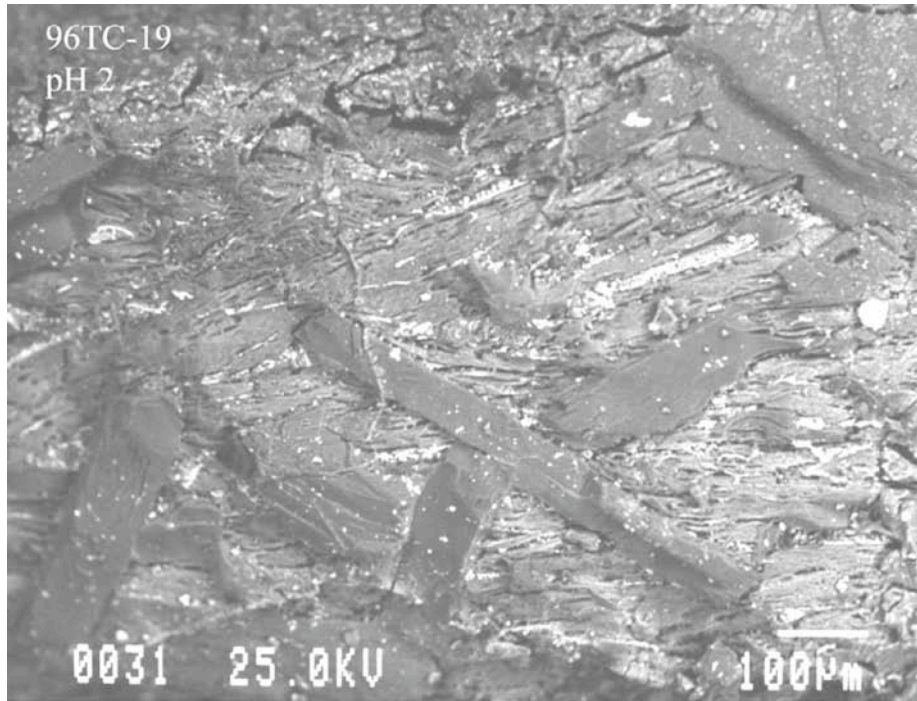


Figure 3-17. SEM secondary electron images of Site B slag sample 96TC-19 following leaching by PNNL at pH 2 and 4. The upper image shows the slag after leaching at pH 2. Dehydration cracking of the glass indicates that glass corrosion has taken place (medium gray, layered appearance). Calzirtite, perovskite (both small white needles) and hibonite crystals (dark gray prismatic crystals) protrude from the glass. Crystallites of secondary phases are precipitated on the glass surface. The lower image shows the slag after leaching at pH 4. The glass (medium gray) is not nearly as corroded. However the calzirtite and perovskite still protrude from the glass.

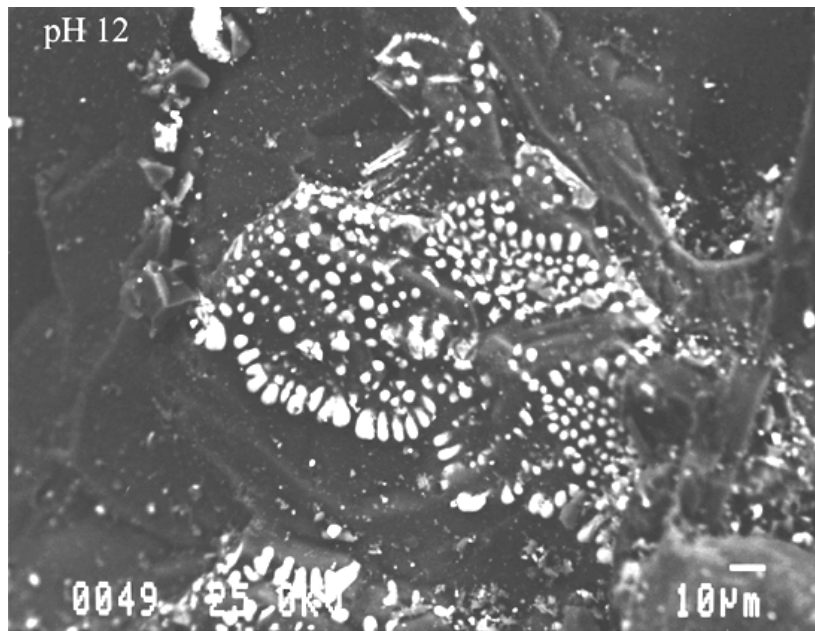
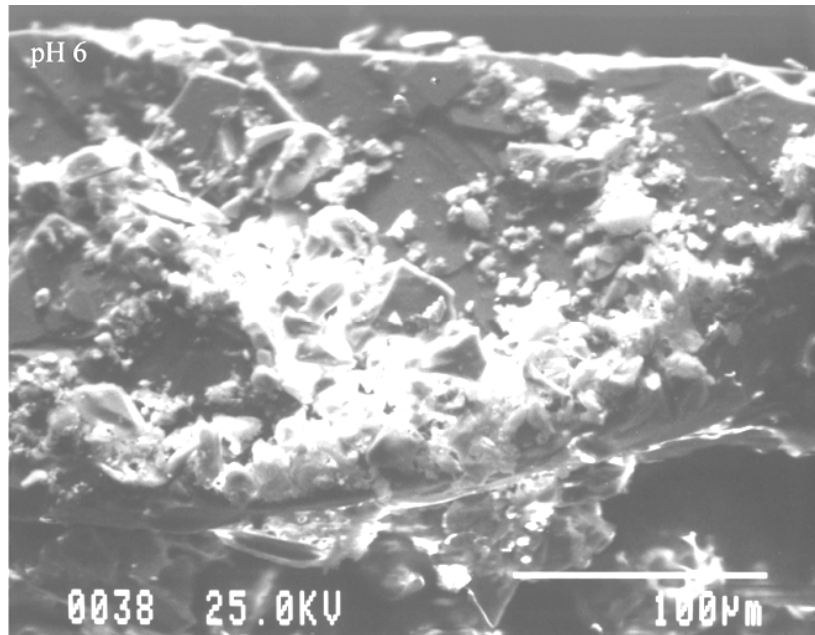


Figure 3-18. SEM secondary electron images of Site B slag sample 96TC-19 after leaching by PNNL at pH 6, and 12. The upper image shows the glass surface after leaching at pH 6. Crystallites of secondary phases are visible on the surface of the glass. The lower image shows the glass surface after leaching at pH 12. Calzirtite is seen protruding from the glass and it does not appear to be as affected by the leaching as was the glass.

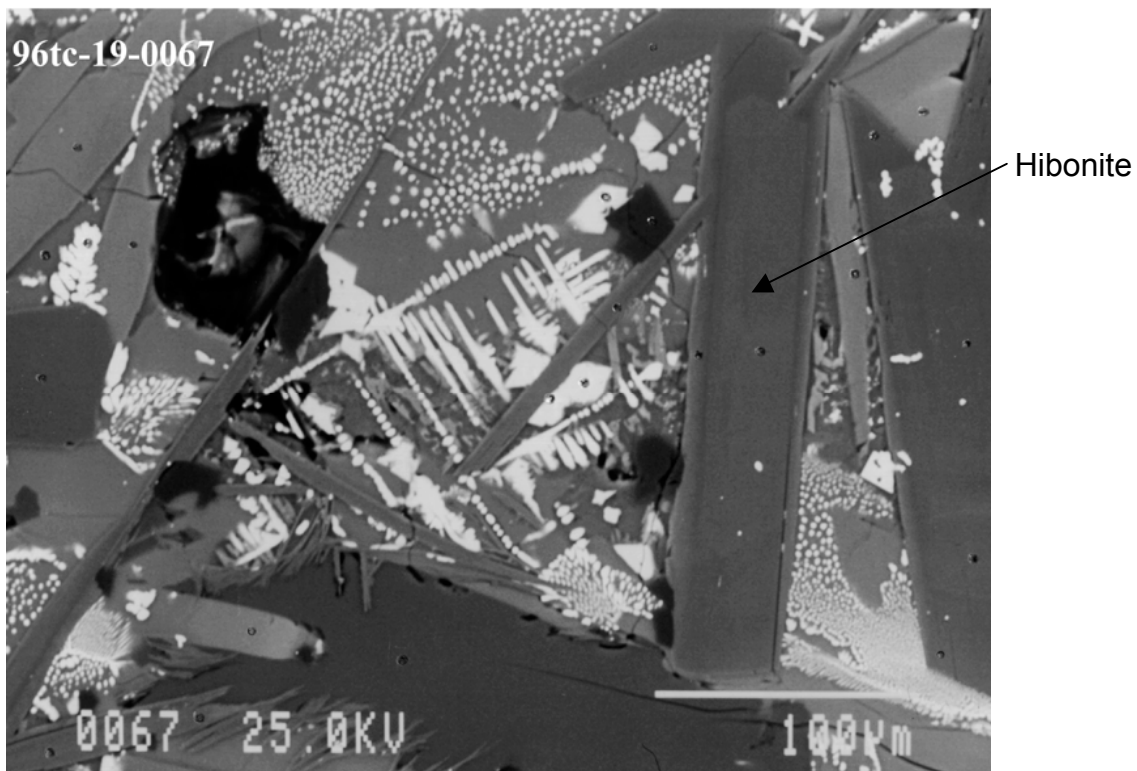
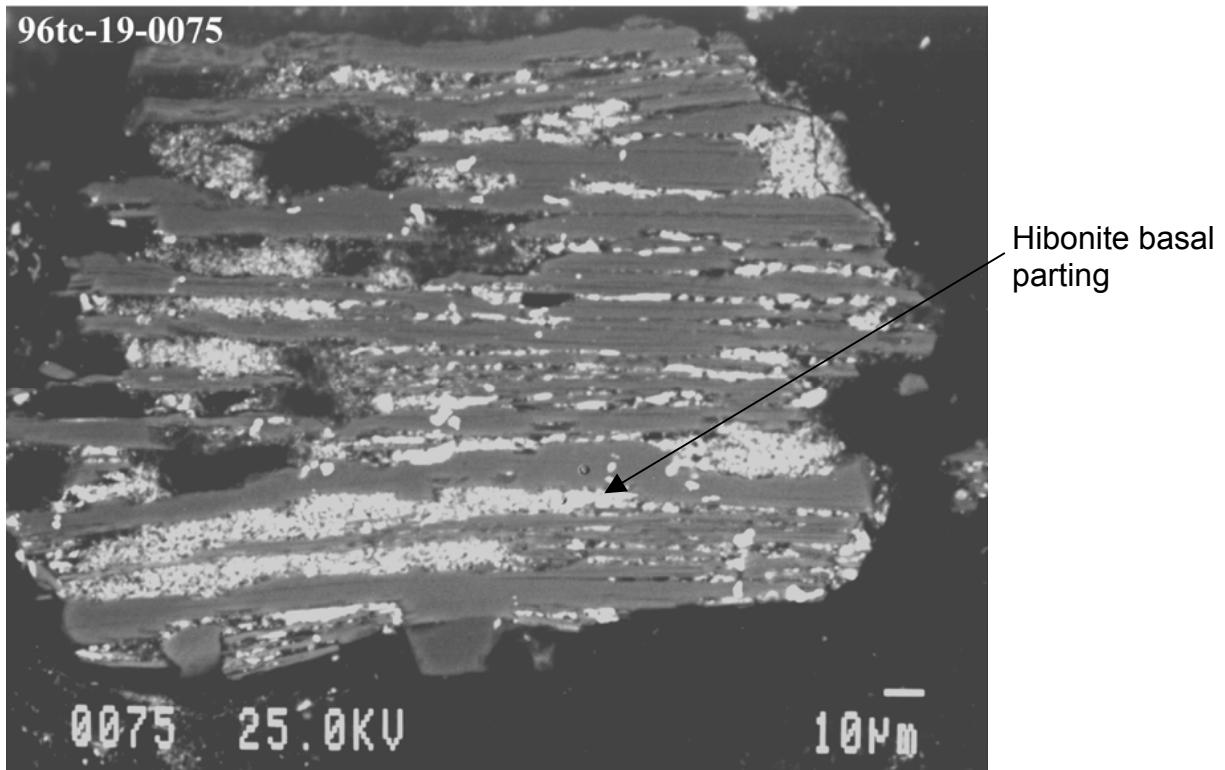


Figure 3-19. SEM secondary electron images of Site B Nb-Ta slag sample 96TC-19 contrasting a leached sample with an unleached one. The upper image was made after leaching by PNNL at pH 2. There is evidence of corrosion along basal partings in hibanite. It is likely that the Ca ions which occupy sites between the octahedral and tetrahedral sheets in the hibanite have been leached or exchanged at this pH. The lower image shows an unleached sample and there is little evidence of corrosion.

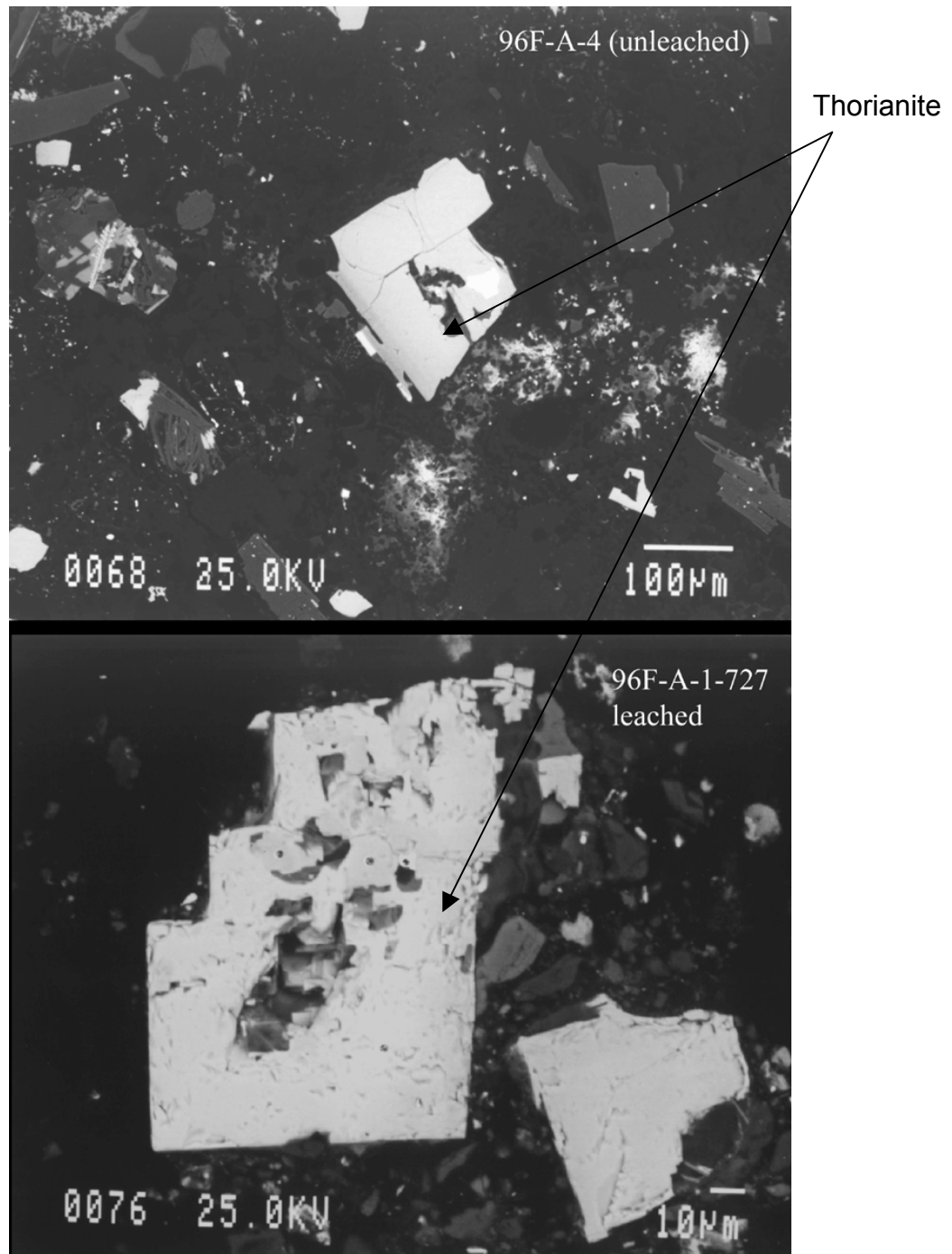


Figure 3-20. BSE image of thorianite grains from Site A slag. The top image shows an unleached grain of thorianite. This polished surface appears to have no defects. The lower image is a thorianite grain leached with deionized water. Note the pitting that has occurred in the interior of the grain.



Figure 3-21. Crift Farm tin slags, Cornwall, England. According to radiocarbon dating, these slags date to 1200 A.D. The slags are very glassy. Because of deep chemical weathering of the slag, it is very difficult to locate sites such as this one.



Figure 3-22. Pribram slag pile, Czech Republic. Pribram mine was the site of Pb, Ag, mining and smelting. This is a 10 - 30 year old slag pile. The surface weathers within several years to a buff or white color.

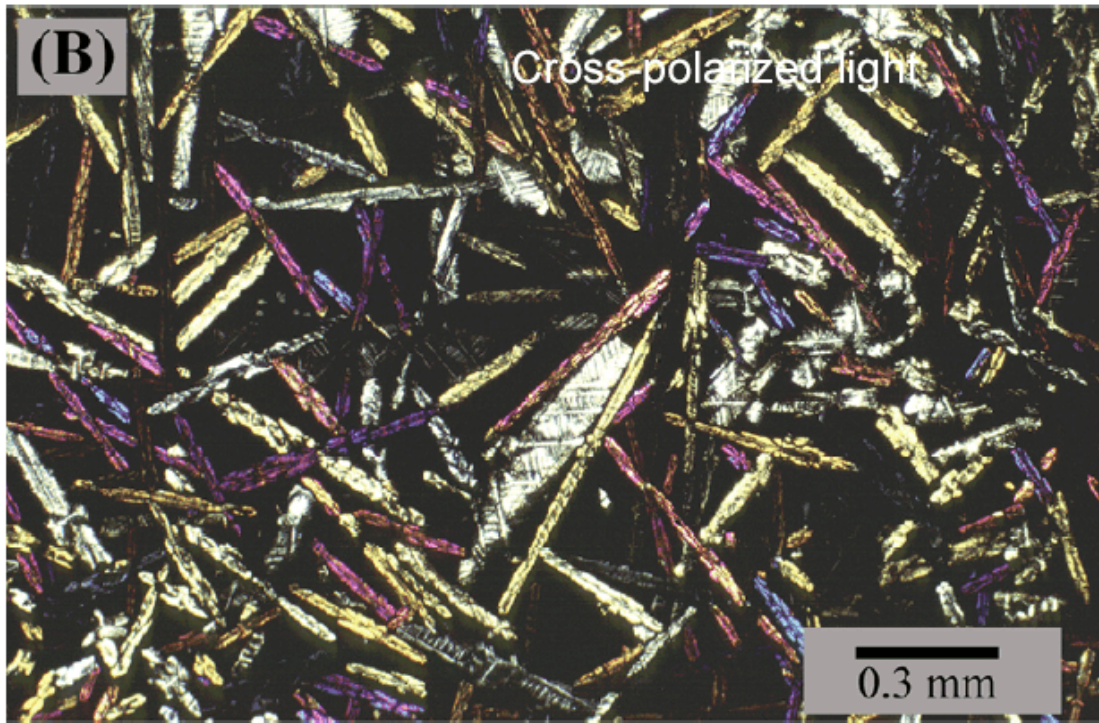
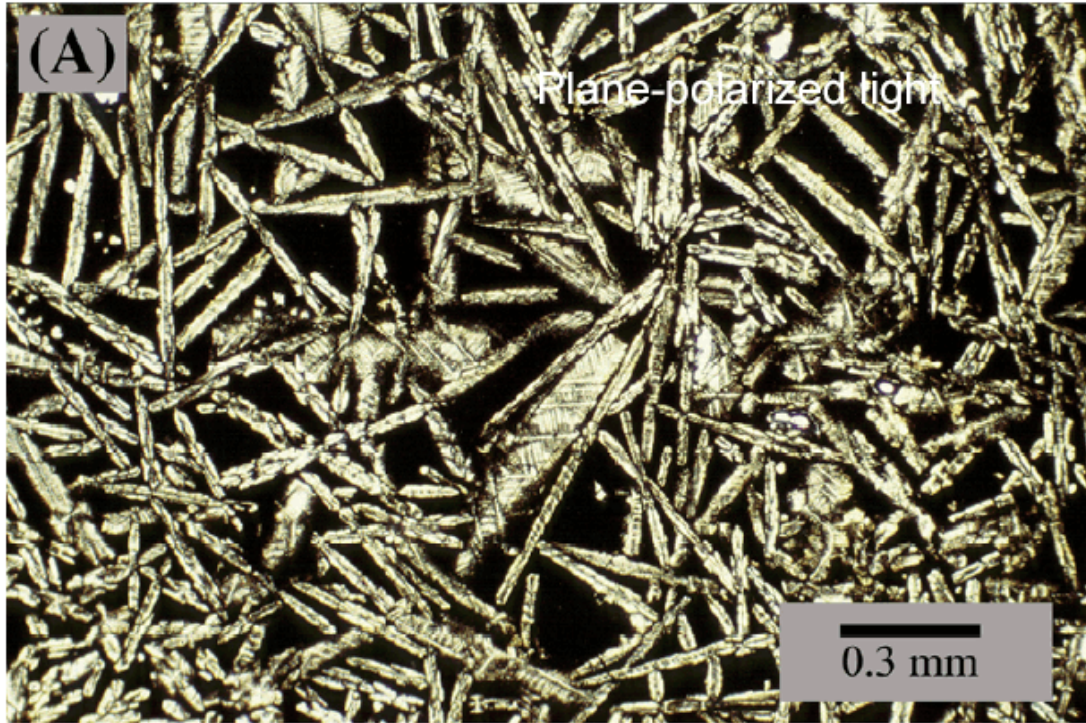


Figure 3-23. Photomicrographs of 1,000 year old Cyprus slag. Complete devitrification of the interstitial glass, as a result of weathering, is observable with a light microscope and is also supported by a flat background in powdered xray diffraction spectra of the bulk sample (see Figure 3-24). The composition and identity of the alteration product are unknown at this time.

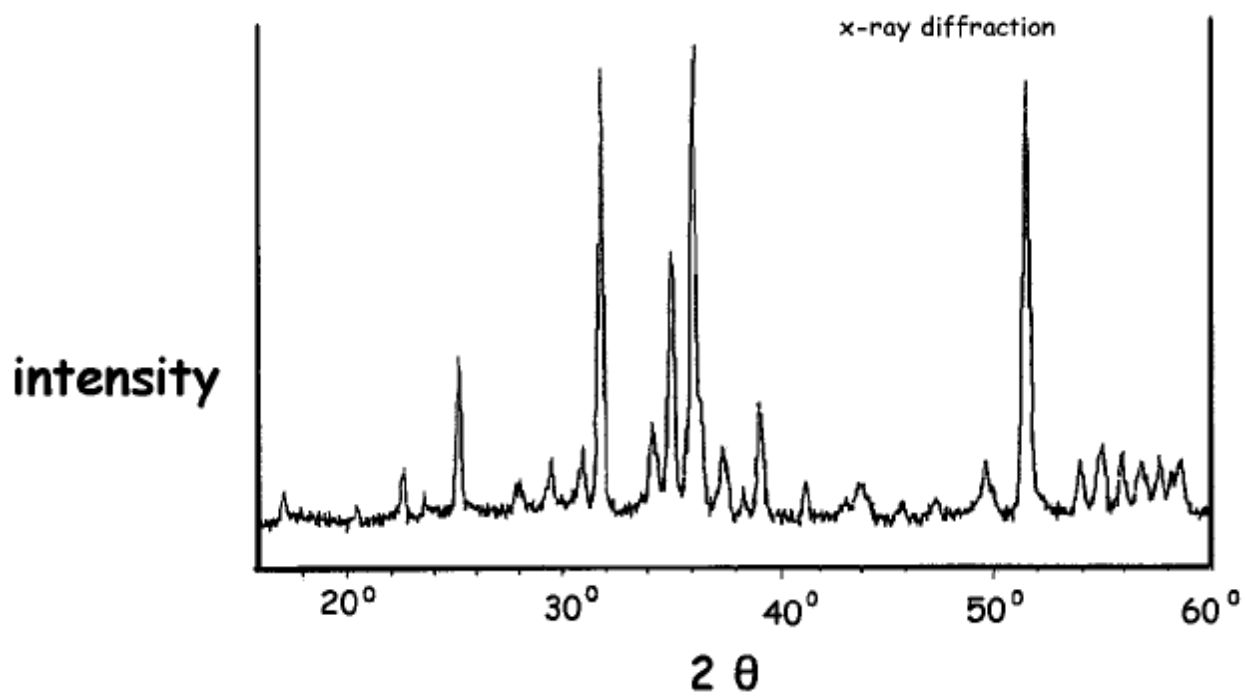


Figure 3-24. X-ray diffraction spectrum of Cu slag from Cyprus (using  $\text{CuK}\alpha$  radiation). This scan has not been background subtracted. The peaks observed in the spectrum correspond with olivine ( $(\text{Fe},\text{Mg}_2)\text{SiO}_4$ ). The absence of a broad hump signifies the absence of glass. During weathering, the glass was altered to form crystalline phases.

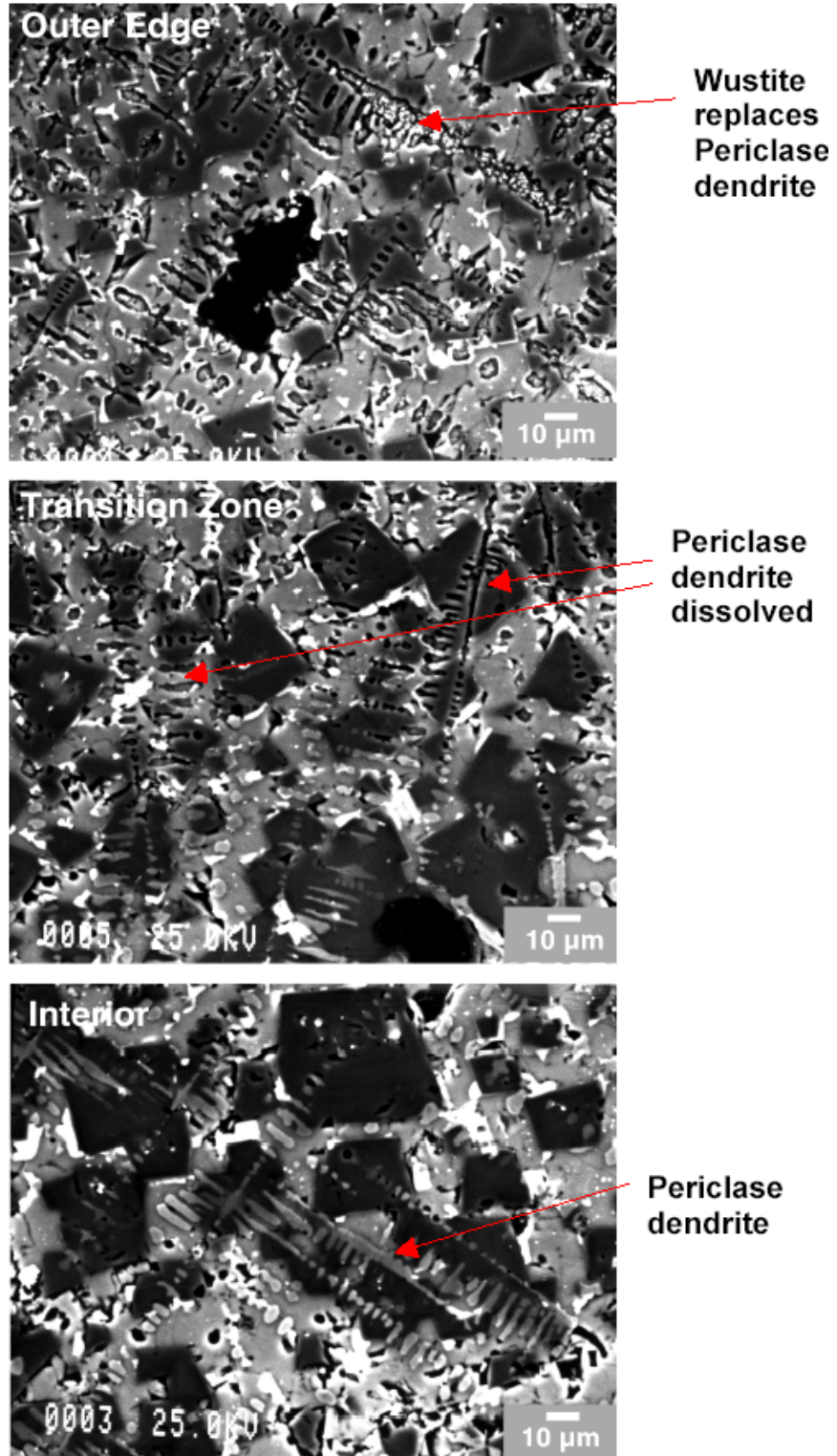


Figure 3-25. BSE images of weathered edge of Site C sample C-1a. MgO, periclase dendrites are dissolved at the outer, weathered edge of the sample (upper image). Toward the interior of the sample (bottom image), the periclase is not dissolved. In the upper image, wustite (FeO) has replaced some of the periclase dendrites.

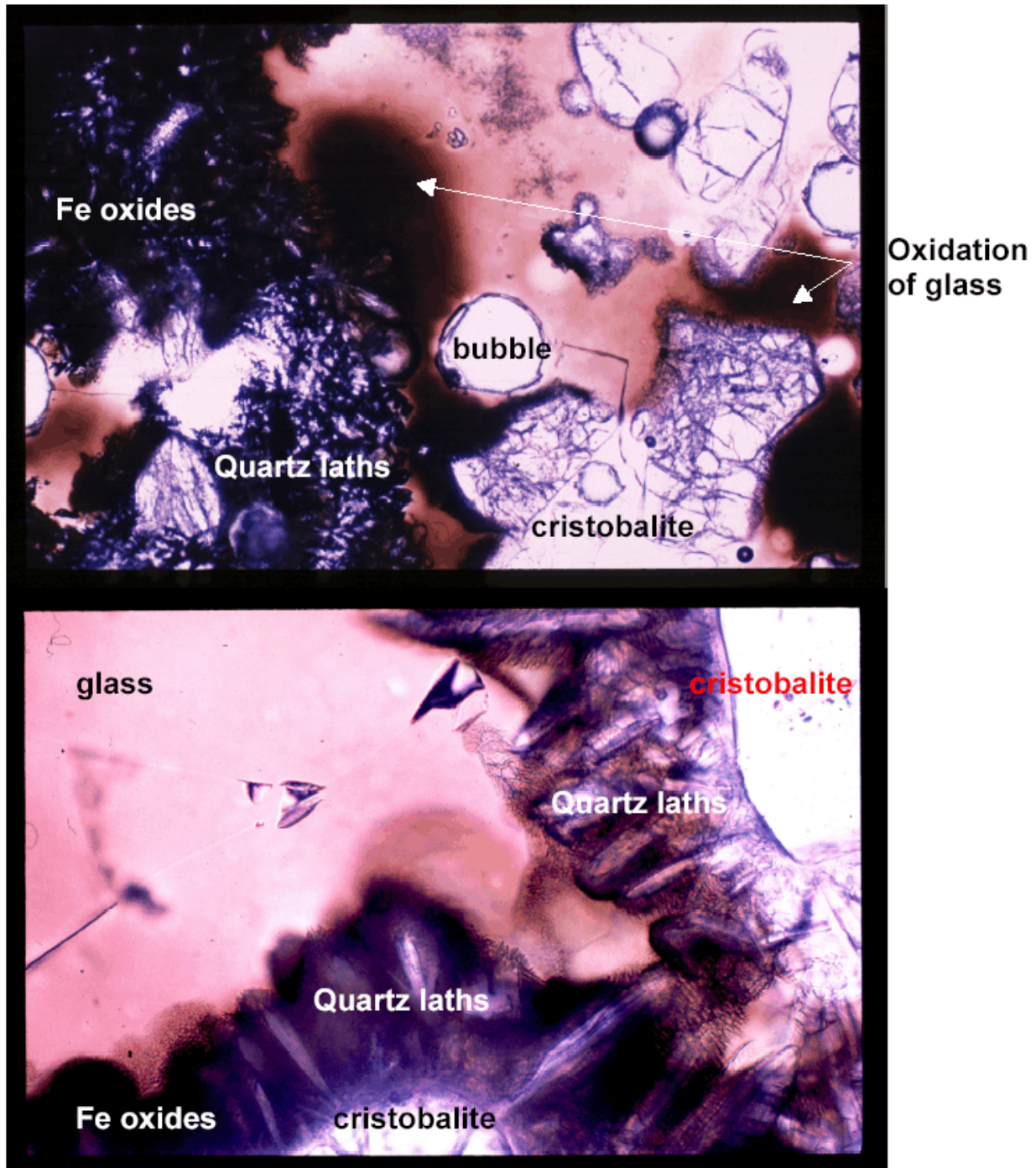


Figure 3-26. Photomicrographs of Site C slag sample C-1a in plane polarized light. Large cristobalite - quartz grains are surrounded by laths of quartz. The glass which appears brown under the polarizing microscope has oxidized in some areas to form Fe oxides.

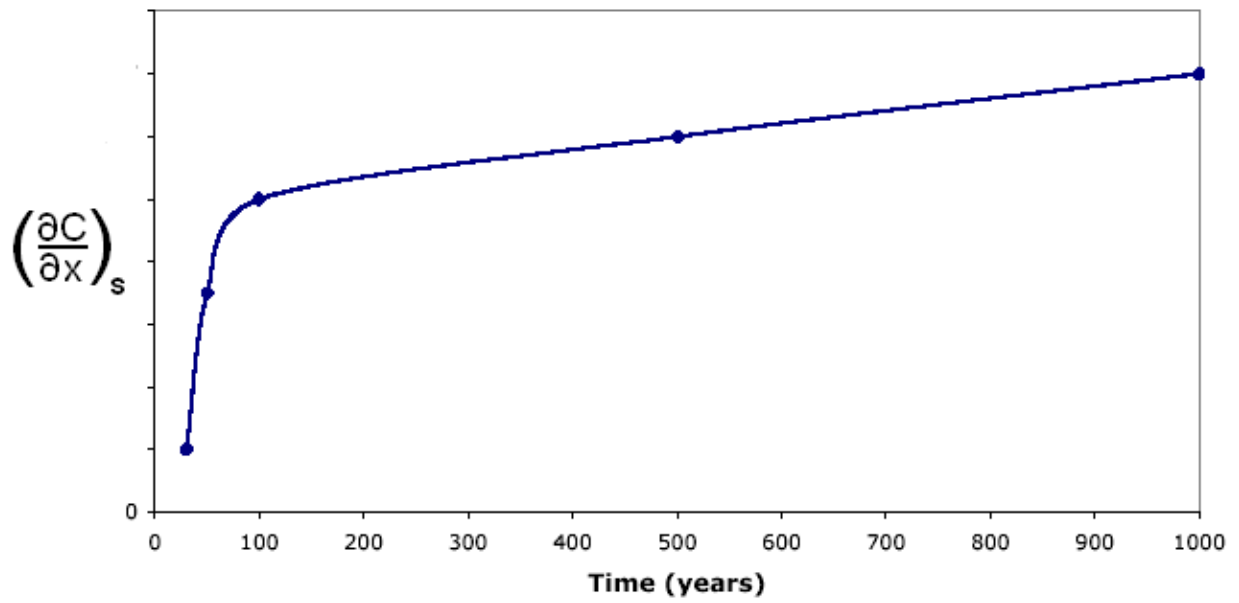


Figure 3-27. Hypothetical plot of a slag's surface-concentration gradient. The figure shows the trend of how the surface-concentration gradient might vary with time, suggesting that the weathering rate and leach rate may vary with time (cf. Equations (4) and (5)).

## 4.0 Conclusions and Recommendations

Slag is a multi-phase material containing glass and crystalline phases: oxides, silicates, carbides, and metals. The release of uranium and thorium from slags depends on the phases of the slags and their durability when subject to weathering. Prior to this study, very little was known about the mineralogy, petrology, and the results of weathering of SDMP Nb-Ta slag. As a result of the study we have identified the dominant phases in slag from three SDMP sites and we have been able to determine the phases in which uranium and thorium reside. These phases weather at different rates, and therefore the uranium and thorium will be released at different rates over time. Identification of the uranium- and thorium-bearing phases will enable the calculation of their release from the slag. In addition to identification of the phases, the weathering characteristics of the slag were identified and the elemental variation which resulted from weathering was determined. The conclusions and recommendations based on this study, have been divided into Site Specific Conclusions, Generic Conclusions, and Future work.

### 4.1 Site Specific Conclusions

#### 4.1.1 Phases Present in Slag

##### 4.1.1.1 Site A

Slag from Site A differs from the two other sites in that it is the product of the reprocessing of a Nb-Ta slag. Following cooling of the Nb-Ta slag, it was ground and subjected to chemical reprocessing and then disposed in evaporation ponds. Natural cementation took place and the slag presently resembles a sandstone. The reprocessed slag is more permeable than slag from sites B and C, so fluid access to the radionuclide-bearing phases is potentially greater.

The dominant phases present at Site A are: hibonite, barium aluminate, spinel, pyrochlore, and perovskite, and are similar to those found at Site C. Glass is present to a lesser extent than at Site B or C. In contrast, Ba aluminate, thorianite, and spinel are absent from Site B.

The radioactivity in the Site A slag is in discrete phases. The uranium- and thorium-bearing phases in the waste material are: perovskite, thorianite ( $\text{ThO}_2$ ), thorite ( $\text{ThSiO}_4$ ), perhaps thorogummite ( $\text{Th,U,CeSiO}_4$ ), and uranophane ( $\text{Ca(UO}_2)_2(\text{SiO}_3\text{OH})_2 \cdot 5\text{H}_2\text{O}$ ). Uranium-bearing phases are a minor constituent of the Site A waste.

##### 4.1.1.2 Site B

The dominant phases are gehlenite, Zr-clinopyroxene, glass, hibonite, and perovskite. Uranium and thorium are contained within discrete phases. The uranium- and thorium-bearing phases in the waste material are perovskite, pyrochlore,

glass, calzirtite, hibonite, cerium silicate ( $\text{CeSiO}_4$ ), and barium aluminate.

##### 4.1.1.3 Site C

The dominant phases present at Site C are hibonite, barium aluminate, spinel, olivine, perovskite, wustite and periclase. At this site, two dominant slag types were present. One is similar to Site A and B because it had high aluminum phases (e.g. Ba aluminate, hibonite, or Ca Al phases). In this slag both uranium and thorium are in perovskite, pyrochlore, and Ti oxides such as thorianite. The second Site C slag is rich in two spinels and olivine. The dominant uranium- and thorium-bearing phases are glass, calzirtite, and perovskite.

#### 4.1.2 Weathering in Slag

Glass and perovskite appear to be the most unstable phases in oxidizing, near-surface conditions. Perovskite may weather to anatase ( $\text{TiO}_2$ ) and thorianite ( $\text{ThO}_2$ ) a stable form of Th, in which case the release of Th may be limited by the relatively low solubility of  $\text{ThO}_2$ . Thorium release will likely be controlled by the solubility of perovskite, thorianite and thorite.

Glass weathers by several means: dissolution, ion exchange, and devitrification. These studies have shown examples of all three mechanisms. Evidence of glass dissolution is visible in several of the SEM-BSE images presented in this report. Quantitative EMPA data provides evidence of preferential leaching or ion exchange in the form of chemical gradients in the near surface glass environment. Devitrification is evident in SEM-BSE and TEM images. These weathering mechanisms are important to understanding the degradation of the slag. The glass is the last phase to form and it fills interstices among all the other phases. Its destabilization will in turn effect all the other phases. Thus, water and other corrosive elements will be more accessible to the radioactive phases.

From examination of the weathering of Site C sample C-s we calculated a bulk release rate of 230  $\text{ng/yr/cm}^2$  of uranium and thorium as was explained in Section 3.3.4. This is similar to the experimentally determined leach rates of Site A (Felmy et al., 1999).

The slags at all three sites have weathered over the 30 years since disposal. It appears from the EMPA analyses that some uranium (and perhaps thorium) has been released from the glass within the slag at Site B. Quantitative analyses of elemental variation within the weathered slags have been completed, and provide estimates of leach rates to be compared with PNNL (Felmy et al., 1999) and CNWRA (Pickett et al., 1998) leach and solubility tests. The leach rate from 96TC-19 for uranium is 3.8  $\mu\text{g/yr/cm}^2$ , and thorium is 32.1  $\mu\text{g/yr/cm}^2$ .

Examination of samples by TEM of experimentally

leached slags from Sites A and B show evidence of degradation. The EMPA data on elemental variation in the slag as a function of pH provides information for interpretation of the leaching data from the PNNL and CNWRA studies. The greatest changes in elemental composition occurred between pH 0.5 to 4. In this range, Ca, Al, U, and Th were depleted, while Si, Mg, and Ti increased.

#### 4.2 Generic Conclusions

As a result of this study's characterization of the chemical composition and phases in slags from three SDMP sites in the humid Eastern United States, One can make the following conclusions.

Although the three sites produced slag from different processes for different metals they all produced Nb-Ta slag from a Sn slag parent material. Any NRC-licensed site that processed Nb-Ta slag may have similar materials to Site B. Therefore the degradation of the slag at this site could be used as a model for other Nb-Ta slag sites.

Uranium and thorium are not uniformly distributed within the slags, rather they are present in discrete phases such as glass, perovskite, calzirtite, and pyrochlore. Microanalytical (petrographic and electron microprobe) information provided in this report will help guide decision makers in identification of slag phases at additional sites.

A bulk dissolution or leach rate does not provide an accurate representation of slag leaching over long times (1000 years). It overestimates the release of radionuclides to the environment. Slag phases weather at different rates, and congruent dissolution of the slag does not occur.

Demonstrable slag weathering occurs on the time scale of 25 - 30 years. Preferential dissolution of certain phases allows fluid access to the interior of the slag. Uranium and thorium are contained within glass and perovskite, which are both unstable at near-surface, humid conditions. However, thorium from perovskite appears to form secondary thorianite which is stable. The alteration products of the glass may sequester the thorium and to a lesser extent the uranium in Ce- and Th-silicates.

The slags studied have been characterized into two similar groups based on bulk chemical composition and the crystalline phases as is shown in the ternary phase diagram of slag compositions in Figure 2-10. The end points of the ternary diagram represent octahedral and tetrahedral sites and coordinating cations. Such characterization provides a means for classification of additional sites, that fall within the bounds of this study. Site B and C slags fall within a tight range on the compositional diagram, indicating a similarity in composition. This means that similar phases will exist in these slags, and therefore will most likely weather at the same rate. Site A slag has a different composition because of the additional

processing. For archeological slags with the passage of time there is a depletion in calcium and sodium. This is evidenced by samples of Sn glass (40-50 years old), Crift Farm Sn slag (500 - 1000 years old), and Treriefe Sn slag (100 - 500 years old) which all fall along a trend line of  $\text{CaO} + \text{Na}_2\text{O} < 10\%$ . The Pribram samples older than 100 years also fall along the  $<10\%$  CaO and  $\text{Na}_2\text{O}$ . Site B and Site C slag fall along same trendline in Figure 2-10 as the Pribram 150 year old slag.

#### 4.3 Recommendations and Future Work

To better understand the release of uranium and thorium from all the phases present in the slags studied requires a more sophisticated approach than assuming a bulk dissolution rate. The phases are similar to SYNROC, vitrified wastes, natural glasses, and naturally occurring perovskite, calzirtite, and pyrochlore. Data gleaned from the literature relating to degradation of these phases can be used to enhance our understanding of slag leach rates.

Analogous archaeological slags have been identified and sampled based on similarity of bulk chemistry, crystalline phases, and glass chemistry. Primary slag phases and alteration products have been identified. Quantification of the modal abundance of primary and alteration phases has been completed and presented in Farthing, 2002.

This study has provided the phase characterization data necessary for calculation of solubility-limited dissolution of slag phases, and calculation of a realistic leach rate (Equation (4)). The data necessary for a solubility limited release rate model are:

- (a) radionuclide bearing phase (for solubility calculation) and its density
- (b) amount of phase present (modal abundance)
- (c) amount of U or Th in phase (mass fraction from EMPA chemical analysis)
- (d) estimate of the weathering rate of a particular phase (m/y)

Given this information, a realistic leach rate could be calculated from Equation (4).

A cost-effective means of site characterization might be as follows:

- a) Review information on the smelting operation, the processing of the slag and final waste products to refine calculations based on the amount of material present at the site.
- (b) Collect representative radioactive material present on the site and obtain bulk chemical analysis, and obtain modal abundance of radioactive phases. (This could be done with X-

ray diffraction, petrographic microscope and point counts.) It should not be necessary for a licensee to provide the level of micro analytical detail provided in this report. With this information: a radionuclide release model could

be developed based on the phase solubility and weathering rates obtained in this study.

## 5.0 References

- Adriaens, A. 1996. "Elemental composition and microstructure of early Bronze Age and Medieval tin slags," *Mikrochim. Acta* 124: 89-98.
- ANSI/ANS-16.1-1986. Measurements of the Leachability of Solidified Low-Level Radioactive Waste by a Short-term Test Procedure. American National Standard American Nuclear Society, Pub. by American Nuclear Society, 555 North Kensington Avenue, La Grange Park, IL 60525, 1986, pp 35.
- Armstrong, 1989. Quantitative analysis of silicate and oxide minerals: Comparison of Monte Carlo, ZAF and Phi-rho-z procedures. In: Newbury, D.E. (Ed.) *Microbeam Analysis - 1988*. San Francisco, CA: San Francisco Press, pp. 239-246.
- Banfield, J.F. and D.R. Veblen, 1992, "Conversion of perovskite to anatase and  $\text{TiO}_2$ : A TEM study and the use of fundamental building blocks for understanding relationships among the  $\text{TiO}_2$  minerals," *American Mineralogist*, 77:545-557.
- Bates, J.K., L.J. Jardine, and M.J. Steindler. 1982. Hydration aging of nuclear waste glass. *Science* 218: 51-54.
- Byers, C.D., M.J. Jercinovic, R.C. Ewing, and K Keil. 1985. Basalt glass: an analogue for the evaluation of the long-term stability of nuclear waste form borosilicate glasses. *Materials Research Society Symposium Proceedings* 44: 583-590.
- Dowty, E. and J.R. Clark, 1973. Crystal Structure Refinement and Optical Properties of a  $\text{Ti}^{3+}$  Fassaite from the Allende Meteorite, *Am. Min.*, 58:230-242.
- EPA 1311, July 1995, Toxicity Characteristic Leaching Procedure, Method 1311., EPA Manual SW-846 Washington DC: US Environmental Protection Agency.
- EPA 1312, July, 1995, Synthetic Precipitation Leaching Procedure, Method 1312, EPA Manual SW-846 Washington DC: US Environmental Protection Agency.
- Felmy, A.R., V.L. LeGore, S.A. Hartley, "Solubility and Leaching of Radionuclides in Site Decommissioning Management Plan (SDMP) Soil and Pooled Wastes," NUREG/CR-6821, United States Nuclear Regulatory Commission, Washington, DC, May 2003.
- Farthing, D.J., 2002, "*The Mineralogy of Tin Slags*", dissertation submitted to Johns Hopkins University, Baltimore, Maryland in conformity with the requirements for degree of Doctor of Philosophy.
- Fauver, D. N., M. F. Weber, T. C. Johnson, and J. D. Kinneman, 1995, "Site Decommissioning Management Plan," NUREG-1444, Supplement 1, U.S. Nuclear Regulatory Commission, Washington, DC 20555, 95 pp.
- Frank, A., A. Madej, V. Galgan, and L.R. Petersson. 1996. Vanadium poisoning of cattle with basic slag. Concentrations in tissues from poisoned animals and from a reference, slaughterhouse material. *The Science of the Total Environment* 181: 73-92.
- Franklin, U.M., J.C. Grosjean, and M.J. Tinkler. 1976. A study of ancient slags from Oman. *Canadian Metallurgical Quarterly* 15 (1): 29-35.
- Gee, C., M.H. Ramsey, J. Maskall, and I. Thornton. 1997. Mineralogy and weathering processes in historical smelting slags and their affect on the mobilization of lead. *Journal of Geochemical Exploration* 58: 249-257.
- Grambow, B., 1992. Geochemical Approach to Glass Dissolution. In Corrosion of Glass, Ceramics and ceramic Superconductors, edited by D.E. Clark and B.K. Zaitos, (Noyes Publications, Park Ridge, New Jersey) pp. 124-152.
- Gustison, R.A. and J.A. Cenerazzo, 1971, Exothermic Fusion of eastern tin slag carbides to a tantalum-columbium concentrate. *Journal of Metals*, pp 45-48.
- Ihinger and Stolper, 1986. The color of meteoritic hibonite: an indicator of oxygen fugacity, *Earth Planet. Sci. Lett.*, 78:67-79.
- Jantzen, C.M., 1992, "Thermodynamic Approach to Glass Corrosion", in Corrosion of Glass, Ceramics and Ceramic Superconductors, Principles, Testing, characterization and Applications", edited by Clark, D.E and B.K. Zaitos (Noyes Publications, Park Ridge, New Jersey) pp 153-215.
- Keil, K. and L.H. Fuchs, 1971. Hibonite  $\text{Ca}_2(\text{Al,Ti})_{24}\text{O}_{38}$  from the Leoville and Allende chondritic meteorites. *Earth Planet. Sci. Lett.* 12:184-90.
- Mascaro, I., M. Benvenuti, and G. Tanelli. 1995. Mineralogy applied to archaeometallurgy: an

- investigation of medieval slags from Rocca San Silvestro (Campiglia M.ma, Tuscany). *Science and Technology for Cultural Heritage* 4 (1): 87-98.
- Maskall, J., K. Whitehead, I. Thornton. 1995. Heavy metal migration in soils and rocks at historical smelting sites. *Environmental Geochemistry and Health* 17: 127-138.
- Smith, J.V., 1979. Mineralogy of the planets: a voyage in space and time. *Mineral. Mag.* 43:1-89.
- Vandiver, P. 1992. Corrosion and conservation of ancient glass and ceramics. In In Corrosion of Glass, Ceramics and ceramic Superconductors, edited by D.E. Clark and B.K. Zaitos, (Noyes Publications, Park Ridge, New Jersey) pp. 393-427.
- Vandiver, P., K.A. Yenner, and L. May. 1992. Third millennium B.C. tin processing debris from Göltepe (Anatolia), p. 545-570. In: Vandiver, P.B. et al. (eds.), *Materials Issues in Art and Archaeology III*. Materials Research Society, Pittsburgh, PA.
- Voutsinou-Taliadouri, F., R. Psyllidou-Giouranovits, and E. Georgakopoulou-Gregoriadou. 1995. Active growth of a submarine slag disposal ore deposit in the northern Euboean Gulf, Greece. *Fresenius Environmental Bulletin* 4: 195-200.
- Xu, H. and Y. Wang, 2000. Crystallization sequence and microstructure evolution of Synroc samples crystallized from CaZrTi<sub>2</sub>O<sub>7</sub> melts. *Journal of Nuclear Materials* 279: 100-106.

## Appendix: Surface Mass-Transfer Coefficients

There is an extensive chemical engineering literature on mass-transfer coefficients. Some examples of these coefficients are given in Sherwood, Pigford, and Wilke (1975). The surface mass-transfer coefficient depends on the fluid flow regime around the slag and on the geometry of the slag.

### A.1 Fluid Flow Regimes

The flow regimes that may occur around slags include stagnation, very slow flow such as groundwater flow, laminar flow, and turbulent flow. The flow regime that has to be considered depends on how the surround fluid's inertial forces compare with its viscous forces, as expressed by the fluid's Reynolds number,

$$\text{Re} = \frac{UL}{\nu} \quad (\text{A1})$$

where  $U$  is a characteristic fluid velocity,  $L$  is a characteristic length of the piece of slag under consideration, and  $\nu$  is the fluid's kinematic viscosity or momentum diffusivity. Mass-diffusion and momentum-diffusion near the slag is compared using the Schmidt number,

$$\text{Sc}_{k_r} = \frac{\nu}{D_{k_r}^F} \quad (\text{A2})$$

where  $D_{k_r}^F$  is the fluid diffusion coefficient for species  $k$  containing radionuclide  $r$ . Mass transfer theory has shown that the Sherwood number for species  $k$  containing radionuclide  $r$ ,

$$\text{Sh}_{k_r} = \frac{H_{k_r} L}{D_{k_r}^F}, \quad (\text{A3})$$

depends on the Reynolds and Schmidt numbers. This functional relationship, which depends on the fluid flow regime and the slag geometry, allows one to estimate the surface mass-transfer coefficient  $H_{k_r}$ .

### A.2 Idealizing Slag Shapes

It may be convenient to view large slabs of slag as flat plates and smaller chunks of slag as spheres or disks. In this study, long cylindrical slags were not observed. Cylindrical shapes may not be suitable idealizations of pieces of slag.

### A.3 Stagnant Fluid

In this case, the Reynolds number is zero, momentum diffusion plays no role, and mass transfer

in the fluid surrounding the slag is diffusional. Sherwood, Pigford, and Wilke (1975) show that for a spherical slag of diameter  $d$  in a stagnant fluid,

$$\frac{H_{k_r} d}{D_{k_r}^F} = 2. \quad (\text{A4})$$

Stagnant-fluid Sherwood numbers, such as that in Equation (A4), are the minimum values for the geometries considered.

### A.4 Very Slow Flow

In very slow flows such as groundwater flows, the Reynolds number is finite but very small. Momentum diffusion is negligible in such flows and

$$H_{k_r} = U \quad (\text{A5})$$

### A.5 Laminar Flow

In laminar flows, inertial fluid accelerations are large, but not enough to destabilize the flows. In the boundary layers near slag surfaces, momentum- and mass-diffusion effects are important. For flow over flat plates (Sherwood, Pigford, and Wilke (1975)),

$$\frac{H_{k_r} L}{D_{k_r}^F} = 0.664 \left( \frac{UL}{\nu} \right)^{1/2} \left( \frac{\nu}{D_{k_r}^F} \right)^{1/3} \quad (\text{A6})$$

where  $U$  is the flow velocity parallel to the flat plate. Equation (A6) is valid for values of Reynolds number up to about 300,000 to 500,000, after which the flow over the plate becomes turbulent.

For laminar flow over a sphere of diameter  $d$ ,

$$\frac{H_{k_r} d}{D_{k_r}^F} = \left( 4 + 1.21 \left( \frac{Ud}{D_{k_r}^F} \right)^{2/3} \right)^{1/2} \quad (\text{A7})$$

which is valid for  $Ud / D_{k_r}^F < 10,000$ .

### A.6 Turbulent Flow

Turbulent flows are chaotic and characterized by high Reynolds numbers. For turbulent flows over flat plates,

$$\frac{H_{k_r} L}{D_{k_r}^F} = 0.036 \left( \frac{UL}{\nu} \right)^{0.8} \left( \frac{\nu}{D_{k_r}^F} \right)^{1/3} \quad (\text{A8})$$

**BIBLIOGRAPHIC DATA SHEET**

(See instructions on the reverse)

1. REPORT NUMBER  
(Assigned by NRC, Add Vol., Supp., Rev.,  
and Addendum Numbers, if any.)

NUREG-1703

2. TITLE AND SUBTITLE

Characterization of Radioactive Slags

3. DATE REPORT PUBLISHED

MONTH | YEAR

October | 2004

4. FIN OR GRANT NUMBER

5. AUTHOR(S)

Linda A. Veblen(1), Dori Farthing(2), Edward O'Donnell(1), John D. Randall(1)  
(1) U.S. Nuclear Regulatory Commission (See Block 8)  
(2) Department of Earth and Planetary Sciences; Johns Hopkins University; Baltimore, MD  
21218

6. TYPE OF REPORT

Staff report

7. PERIOD COVERED (Inclusive Dates)

1997-2002

8. PERFORMING ORGANIZATION - NAME AND ADDRESS (If NRC, provide Division, Office or Region, U.S. Nuclear Regulatory Commission, and mailing address; if contractor, provide name and mailing address.)

Division of Systems Analysis and Regulatory Applications  
Office of Nuclear Regulatory Research  
U.S. Nuclear Regulatory Commission  
Washington, DC 20555-0001

9. SPONSORING ORGANIZATION - NAME AND ADDRESS (If NRC, type "Same as above"; if contractor, provide NRC Division, Office or Region, U.S. Nuclear Regulatory Commission, and mailing address.)

Same as above

10. SUPPLEMENTARY NOTES

11. ABSTRACT (200 words or less)

Slag samples from three humid region sites located in the Eastern United States were studied in detail. Since this investigation is generic in nature, the precise locations of the sites are not identified and are referred to as Sites A, B, and C. Site A's slag was formed from a reprocessed Nb-Ta slag that was ground, leached and deposited in settling ponds which were allowed to evaporate. The resulting material was a "rock like," porous, altered material that resembled a sandstone. Site B was the most intensively studied site and it provided valuable information on the physical and chemical form of the original Nb and Ta slag, as well as the Sn slag that was used as the "ore" material. Site C's slag, although not studied in as much detail as the Site B slag, is physically similar to the Site B slag and both sites had (i) glassy slag and (ii) dense dark slags that ranged from fine grained to very coarsely crystalline. Detailed microanalytical data from Sites B and C provide information regarding the degradation of the radionuclide-bearing phases. Uranium and thorium are present in glass, perovskite, calzirtite, zirconolite, and pyrochlore. Cerium and thorium are present in hibonite. These phases are similar to phases in the proposed high-level radioactive waste form SYNROC. Numerous studies provide experimentally determined solubility and leach rates for these phases. These data provide insight into and bounding values for estimates of slag leach rates. Data reduction and a detailed petrological study provide the necessary information for guidance to the NRC's Office of Nuclear Material Safety and Safeguards for license termination at future decommissioning sites.

12. KEY WORDS/DESCRIPTORS (List words or phrases that will assist researchers in locating the report.)

Slags, uranium, thorium

13. AVAILABILITY STATEMENT

unlimited

14. SECURITY CLASSIFICATION

(This Page)

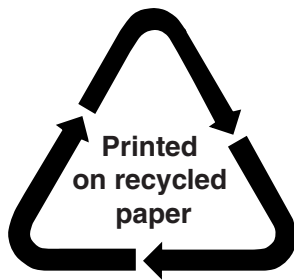
unclassified

(This Report)

unclassified

15. NUMBER OF PAGES

16. PRICE



**Federal Recycling Program**